広島大学学位請求論文

Exploring Emission Region of Gamma-ray Pulsars

ガンマ線パルサーの放射領域に関する研究

2012年

広島大学大学院理学研究科物理科学専攻

木坂 将大

目次

1. 主論文

Exploring Emission Region of Gamma-ray Pulsars
ガンマ線パルサーの放射領域に関する研究
木坂 将大

2. 公表論文

(1) Multi-Wavelength Emission Region of γ-ray Emitting Pulsars
S. Kisaka and Y. Kojima
Astrophysical Journal, 739 (2011) 14

3. 参考論文

(1) TeV cosmic ray electrons from millisecond pulsars
S. Kisaka and N. Kawanaka
Monthly Notices of the Royal Astronomical Society, in press

(2) Magnetic field decay with Hall drift in neutron star crusts
Y. Kojima and S. Kisaka
Monthly Notices of the Royal Astronomical Society, in press

(3) Mass-Dependent Evolution of the Relation Between Supermassive Black Hole Mass and Host Spheroid Mass Since z ~ 1
S. Kisaka and Y. Kojima
Monthly Notices of the Royal Astronomical Society, 405 (2010) 1285-1292

(4) The Correlation of Black Hole Mass with Metallicity Index of Host Spheroid
S. Kisaka, Y. Kojima and Y. Otani
Monthly Notices of the Royal Astronomical Society, 390 (2008) 814-818

主論文

Exploring Emission Region of Gamma-ray Pulsars

Shota Kisaka

Graduate School of Science
Hiroshima University

January, 2012

Abstract

There is not yet common understanding of the pulsar magnetosphere. Recently, number of sources detected in γ-ray is significantly increasing thanks to *Fermi Gamma-ray Space Telescope*. The pulsed emission in the GeV energy band is an important tool for probing the particle acceleration and dissipation processes in the magnetosphere, since the characteristic energy of curvature radiation from charged particles with the maximum determined by the acceleration-radiation-reaction corresponds to the GeV band. *Fermi* results support that the γ-ray emission region is relatively far from the star, since the observed γ-ray spectrum of most pulsars can be fitted by the power-law with normal exponential cutoff. There is no evidence of the magnetic pair-creation attenuation occurred near the stellar surface. The emission in the slot gap or outer gap models is located at rather outer region of the magnetosphere. These models are preferable, but the fitting to the γ-ray light curve cannot distinguish them. The pulsed emission is also detected in other energy bands (in X-ray, ultraviolet, optical and radio bands) for some sources. The combination of multi-wavelength light curves can provide valuable information of the emission regions, which are imprinted in radiation with different energy through the electromagnetic cascade process.

In this thesis, we adopt the outer gap model and investigate the emission region by comparing it with the multi-wavelength light curves from energetic pulsars. We assume that γ-ray and non-thermal X-ray photons are emitted from a particle acceleration region in the outer magnetosphere, and UV/optical photons originate above that region. We also assume that γ-rays are radiated only by outwardly moving particles, whereas the other photons are produced by particles moving outward and inward. The light curves are modeled by the altitude of the emission region, magnetic dipole inclination angle and viewing angle of the pulsars. For the pulsars observationally constrained these angles, the altitude of the emission region is determined, and it is found that the outer gap model can explain the multi-wavelength pulse behavior by a simple distribution of emissivity. From observational fitting, we also find a general tendency for the altitude of the γ-ray emission region to depend on the inclination angle. This empirical relation suggests a modification of statistics about observed γ-ray pulsars. Number of the sources with low inclination and viewing angles increases compared with previous estimate.

Acknowedgements

First of all, I wish to thank my supervisor, Prof. Yasufumi Kojima, for much valuable discussions, useful suggestions and patience throughout my post-graduate study. I am also grateful to Associate Prof. Kazuhiro Yamamoto, Assistant Prof. Tsunehiko N. Kato and Associate Prof. Ryo Yamazaki whose insightful comments and suggestions were valuable for my study. I would like to thank Kunihito Ioka, Kazumi Kashiyama, Norita Kawanaka, Yutaka Ohira, Shinpei Shibata, Jumpei Takata, Shuta J. Tanaka, Tomohide Wada, Masaki S. Yamaguchi and Shinya Yuki for contributing to my study and for fruitful discussions. I would also like to thank all my colleagues in our group, especially Tatsuya Narikawa, Gen Nakamura and Yugo E. Kato for useful comments and discussions. I would like to thank my parents and my grandparents for their continuous support and encouragements. This work was supported in part by a Grant-in-Aid for Scientific Research from the Japan Society for the Promotion of Science (JSPS).

List of Useful Astronomical and Physical Constants

c	speed of light	2.998×10^{10} cm/s
G	gravitational constant	6.673×10^{-8} dyn cm^2 g^{-2}
h	Planck constant	6.626×10^{-27} erg s
k_B	Boltzmann constant	1.381×10^{-16} erg K^{-1}
m_e	mass of an electron	9.109×10^{-28} g, 511.00 keV/c^2
m_n	mass of a neutron	1.674×10^{-28} g, 939.56 MeV/c^2
m_p	mass of a proton	1.673×10^{-24} g, 938.27 MeV/c^2
e	electric charge	4.803×10^{-10} esu
α_{f}	$= e^2/hc$, fine structure constant	7.297×10^{-3}
r_e	$= e^2/m_e c^2$, classical electron radius	2.818×10^{-13} cm
λ_C	$= h/m_e c$, electron Compton wavelength	2.426×10^{-10} cm
σ_T	$= 8\pi r_e^2/3$, Thomson cross section	6.652×10^{-25} cm^2
B_c	$= m_e^2 c^3/he$, critical magnetic field strength	4.414×10^{13} G
$M_\odot$	solar mass	1.989×10^{33} g

List of Symbols

$a(\eta)$	function
a_0	coefficient
a_1	coefficient
$a_1(\eta)$	function
A_1	coefficient
A_2	coefficient
$A_{\rm abs}$	cross-sectional area at absorption radius
$A_{\rm sur}$	surface area of slot gap
$A(r)$	cross-sectional area of radio cone beam
b_1	coefficient
B	magnetic field
B'	magnetic field normalized by critical magnetic field
B_1	coefficient
$B_{\rm in}$	internal magnetic field of neutron star
$B_{\rm NS}$	surface magnetic field of neutron star
$B_{\rm s}$	surface magnetic field of normal star
$C(\Psi)$	constant along magnetic field line
C_1	coefficient
$C_{\rm g}$	function
d	distance
D	coefficient
$D_{\rm g}$	function
E	electric field
E_F	Fermi energy
$E_{\rm cur}$	characteristic energy of curvature radiation
$E_{\rm syn}$	characteristic energy of synchrotron radiation
$E_{\rm th}$	threshold energy of photo-photon pair creation
$E_{\rm X}$	energy of X-ray photon
E_γ	energy of γ-ray photon
f	gap fraction
$f(1)$	general relativiatic parameter
$f_{\rm rad,cur}$	radiation drag force for curvature radiation
$f_{\rm rad,sc}$	radiation drag force for synchrotron and curvature radiations
$f_{\rm rad,syn}$	radiation drag force for synchrotron radiation
f_Ω	beaming factor
F	function
$F_{\rm cur}$	total power of curvature radiation
$F_{{\rm cur},\omega}$	energy spectrum of curvature radiation
$F_{\rm pc}$	poloidal flux over a cap
$F_{\rm radio}$	radio flux

$F_{\mathrm{sc},\omega}$	power of synchro-curvature radiation
F_{SG}	radiated flux of slot gap
F_{syn}	total power of syncrotron radiation
$F_{\mathrm{syn},\omega}$	energy spectrum of syncrotron radiation
F_{γ}	photon energy flux
$F_{\gamma,100}$	energy flux between 100 MeV and 300 GeV
g	difference between charge density and GJ-one in the units of GJ-one
g_1	g at main accelerating region
g_2	g at screening region
g_{NS}	surface gravity of neutron star
h	coordinate along magnetic field line
h_0	parameter for polar cap model
$h_{\mathrm{fl},1}$	height of boundary between accelerating and screening regions
$h_{\mathrm{fl},2}$	height of upper boundary of outer gap
H	gap height
$H(1)$	general relativistic parameter
H_{atm}	scale height of atmosphere of neutron star
I	moment of inertia
$I(\theta)$	net total current between pole and angle θ
I_0	observed radio intensity
I_{m}	maxmun of $I(\theta)$
j_1	current in units of GJ value carried by particle into gap through inner boundary
j_2	current in units of GJ value carried by particle into gap through outer boundary
j_g	current in units of GJ value carried by pairs produced in gap
J	current density
J_{back}	current density of back flow
J_{GJ}	Goldreich-Julian current density
J_{in}	current density interior of pulsar
J_l	Bessel function
J_l'	derivative of J_l
J_{out}	current density exterior of pulsar
J_{sur}	current density at surface
K	constant
$K_{5/3}(\xi)$	modifoed Bessel function of second kind of order 5/3
l_{B}	photon mean free path for magnetic pair creation
l_{p}	photon mean free path for photon-photon pair creation
L_{1400}	luminosity at 1400 MHz
L_{r}	radio luminosity
L_{sd}	spin-down luminosity
L_{SG}	luminosity of slot gap
L_{tor}	total torque exerted from star
L_{x}	X-ray luminosity
M_{NS}	mass of neutron star
$\mathcal{M}_{\mathrm{pair}}$	pair multiplicity

$\dot{n}$	particle flux
$\dot{n}_{\rm SG}$	particle flux of slot gap
n_e	electron number density
$n_{\rm GJ}$	Goldreich-Julian number density
$n_{\rm ph}$	photon number density
$n_{\rm r}$	local radio photon number density
N_+	number density of positron
N_-	number density of electron
$N_{\rm CR}(\epsilon)$	curvature radiation energy spectrum
$N_{\rm ICS}$	inverse Compton scattered photon number
$N_{\rm p}$	particle number density
$N_{\rm X}$	number density of X-ray photon
$\dot{N}_{\rm SC}$	γ-ray absorption rate
$\dot{N}_{\rm SR}$	synchrotron photon number flux
$\mathcal{N}_{\rm pairs}$	energy spectrum of pairs
p	momentum
p_F	Fermi momentum
P	period
$\dot{P}$	time derivative of period
$P_{\rm B}$	probability (per unit length) of magnetic pair-creation
P_l	Legendre polynominal
$P_{\rm p}$	photon conversion probability
Q_2	function
$r_{\rm abs}$	absorption radius
$r_{\rm B}$	radius of gyroration
$r_{\rm c}$	synchro-curvature radius
$r_{\rm em}$	radial distance at emission point
$r_{\rm g}$	gravitational radius
$r_{\rm n}$	radial distance to null surface
$r_{\rm n,lim}$	limiting distance to null surface
$r_{\rm ov}$	magnetic colatitude normarized by polar cap angle $\equiv \theta_{\rm m}/\theta_{\rm m}^{\rm pc}$
$\Delta r_{\rm ov,SG}$	magnetic colatitude for width of slot gap
$R_{\rm cur}$	curvature radius of magnetic field line
$R_{\rm eff}$	effective radius of emitting region
$R_{\rm LC}$	radius of light cylinder
$R_{\rm max}$	radius for maximum mass of neutron star
$R_{\rm NS}$	radius of neutron star
$R_{\rm pc}$	polar cap radius
$R_{\rm s}$	radius of normal star
R_∞	radiation radius
s	photon propagating distance
$s_{\rm col}$	invariant energy for two-body collision
$s_{\rm col,tot}$	invariant total energy for two-body collision
δs	width of outer gap

$S(r)$	source term
$S_{\rm peak}$	peak flux density
t	time
Δt	pulse duration
$t_{\rm r}$	retarded time
$T_{\rm e}$	escaping temperature for electron
$T_{\rm i}$	escaping temperature for ion
$T_{\rm s}$	surface temperature
$T^{\alpha\beta}$	energy-momentum tensor
$T^{\alpha\beta}_{\rm em}$	electromagnetic energy-momentum tensor
w	thickness of outer gap
w_e	width of radio cone beam
W	pulse width
W_{50}	half-power pulse-width
$x_{\rm fl}$	coordinate along field line
$z_{\rm fl}$	coordinate along field line
$z'_{\rm fl}$	$z_{\rm fl}$ normalized by $h_{\rm fl,2}$
Z	atomic number
α	inclination angle
α_0	lapse function on neutron star surface
$\alpha_{\rm p}$	pitch angle
$\beta_{\rm cm}$	velocity normalized by c in center-of-momentum frame
$\beta_{\rm i}$	impact parameter
$\gamma_{\rm p}^{\rm br}$	Lorentz factor at break point for pairs
$\gamma_{\rm cm}$	Lorentz factor in center-of-momentum frame
$\gamma_{\rm p}^{\rm max}$	maximun Lorentz factor for pairs
$\gamma_{\rm p}^{\rm min}$	minimum Lorentz factor for pairs
$\gamma_{\rm p}$	Lorentz factor of pairs
$\gamma_{\rm r}$	Lorentz factor for relative velocity
$\gamma_{\rm res}$	Lorentz factor for resonance
$\gamma_{\rm sat}$	Lorentz factor for satulated particle
$\gamma_{\rm tot}$	Lorentz factor for $s_{\rm tot}$
$\delta(\eta)$	function
δ_1	spectral index for pairs at low energy
δ_2	spectral index for pairs at high energy
ε	photon energy in units of electron rest mass energy
ε_0	energy of radio photon in units of electron rest mass energy
$\varepsilon_{\rm cur}$	$= E_{\rm cur}/(m_{\rm e}c^2)$
ε_s	scattered photon energy in units of electron rest mass energy
$\varepsilon_{\rm SR}$	$= E_{\rm syn}/(m_{\rm e}c^2)$
$\epsilon_{\rm A}$	small geometrical parameter
$\epsilon_{\rm ph}$	energy of a photon
ϵ_γ	radiative efficiency
ζ	viewing angle

$\zeta_{\rm in}$	inner boundary of outer gap
$\zeta_{\rm out}$	outer boundary of puter gap
η	radial distance normarized by neutron star radius ($\equiv r/R_{\rm NS}$)
$\eta_{\rm acc}$	efficiency of accelerating electric field ($= E_{\parallel}/B$)
$\eta_{\rm c}$	free parameter for slot gap
$\eta_{\rm p}$	pair creation rate
$\eta_{\rm r}$	radio emission altitude normalized by stellar radius
θ_0	polar cap half-angle including general relativistic correction
$\theta_{\rm b}$	half-angle of γ-ray beam from polar cap
$\theta_{\rm em}$	angle between emission direction and radiak direction at emission point
$\theta_{\rm m}$	magnetic polar angle
$\theta_{\rm pc}$	magnetic colatitude of polar cap
$\theta_{\rm m}^{\rm pc,0}$	magnetic colatitude of polar cap in vacuum dipole
$\theta_{\rm X\gamma}$	collision angle between X-ray and γ-ray photons
$\Theta(x)$	step function
$\Theta(\mu)$	angular distribution function
κ	general relativistic parameter from frame dragging effect
$\kappa(x)$	function
λ	mean free path for surface X-ray photon
Λ	logarithmic factor
$\Lambda_{\rm SG}$	function of slot gap
μ	$= \cos\theta$
$\mu_{\rm dip}$	magnetic dipole moment
μ_s	scattered photon angle
ν	radio spectral index
$\nu_{\rm SG}$	parameter related to width of slot gap
ρ	charge density
ρ_0	charge density at neutron star surface
ρ_1	charge density at main accelerating region
ρ_2	charge density at screening region
$\rho_{\rm cone}$	opening semi-angle of radio emission cone
$\rho_{\rm GJ}$	Goldreich-Julian charge density
$\rho_{\rm in}$	charge density inside of pulsar
$\rho_{\rm out}$	charge density outside of pulsar
$\rho_{\rm sur}$	charge density at surface
σ	scattering cross section
$\sigma_{\gamma\gamma}$	cross section of photon-photon pair creation
$\tau_{\rm c}$	spin-down age
$\tau_{\rm syn}$	synchrotron lifetime
$\tau_{\gamma\gamma}$	optical depth for photon-hpoton pair-creation
ϕ'	electric potential of accelerating field
ϕ_0	constant
$\Delta\phi$	phase separation
$\phi_{\rm em}$	azimuthal angle at emission point

ϕ_{fl}	coordinate along field line
ϕ_{in}	electric potential inside of pulsar
ϕ_{nco}	non-corotation potential
ϕ_{out}	electric potential outside of pulsar
ϕ_{m}	magnetic azimuthal angle
ϕ_{NS}	$\equiv B_{\mathrm{NS}}R_{\mathrm{NS}}^2/R_{\mathrm{LC}}$
ϕ_{sur}	electric potential at the surface
$\phi_{\mathrm{tot}}^{\mathrm{SG}}$	full potential drop of slot gap model
$\phi_{\mathrm{low}}^{\mathrm{SG}}$	low-altitude potential of slot gap
$\phi_{\mathrm{high}}^{\mathrm{SG}}$	high-altitude potential of slot gap
χ_1	lower boundary of outer gap
χ_{up}	upper boundary of outer gap
ψ	position angle
ψ_0	porjected direction of rotation axis
Ψ	stream function
Ψ_{b}	angle between photon and local enectron beam directions
ω	frequency
ω_{B}	frequency of gyration
ω_{c}	characteristic frequency of synchro-curvature radiation
ω_{cur}	characteristic frequency of curvature radiation
ω_{syn}	characteristic frequency of synchrotron radiation
Ω	angular velocity of pulsar
Ω_{p}	solid angle
$\Omega_{\mathrm{p,SG}}$	solid angle of slot gap model
$\Omega_{\mathrm{p,r}}$	radio emission solid angle

Contents

1 INTRODUCTION **15**

2 BASIC PHYSICAL PROCESSES **17**
- 2.1 Emission Mechanisms 17
  - 2.1.1 Synchrotron radiation 17
  - 2.1.2 Curvature radiation 18
- 2.2 Pair Creation Processes 18
  - 2.2.1 Magnetic pair-creation 18
  - 2.2.2 Photon-photon pair-creation 19

3 PULSARS **21**
- 3.1 Observational Properties of Pulsars 21
  - 3.1.1 Rotating magnetized neutron stars 21
  - 3.1.2 Pulsed emission properties in each energy band 24
- 3.2 Pulsar Magnetosphere 34
  - 3.2.1 Goldreich-Julian Critique 34
  - 3.2.2 Force-free approximation 41
- 3.3 Particle Acceleration and Emission Models 43
  - 3.3.1 Polar cap model 43
  - 3.3.2 Slot gap model 47
  - 3.3.3 Outer gap model 61
  - 3.3.4 Inner acceleration region vs outer acceleration region 70
  - 3.3.5 Slot gap vs outer gap 72
- 3.4 Remarks to Further Model 74

4 MODEL **76**

5 RESULTS **79**
- 5.1 Vela pulsar (PSR J0835-4510) 79
- 5.2 PSR J0659+1414 80
- 5.3 PSR J0205+6449 84
- 5.4 PSR J2229+6114 84
- 5.5 PSR J1420-6048 84
- 5.6 PSR J2021+3651 85
- 5.7 PSR J1057-5226 85

6 DISCUSSIONS **87**
- 6.1 Statistical Properties of the Emission Region 87
- 6.2 The Phenomenological Limitation for Emissivity 88
- 6.3 The Location of the UV/Optical Emission Region 91

7 CONCLUSIONS **93**

A The effect to the cut-off energy **94**

1 INTRODUCTION

The pulsars emit stable and periodic pulsed radiation over a wide range of energies from radio to γ-ray. They are identified to isolated, rapidly rotating, highly magnetized neutron stars since the proposals by Gold (1968) [49] and Pacini (1967) [115]. Pulsars are divided into the rotation-powered and accretion-powered ones depending on their the energy sources. In this thesis, we only consider the rotation-powered pulsars.

The structure of the rotation-powered pulsars remains one of profound problems. In the earliest, the models of the magnetic dipole rotator were considered (e.g., [115]). If rotation and magnetic axes are misaligned, the rotating magnetic dipole in vacuum emits the pulsed radiation essentially at the rotational frequency with a characteristic dipole pattern. If this radiation can propagate away from the pulsar, it will be detected as a periodic signal. However there are other effects that could prevent it from the propagation. In the above model, the region outside the pulsar is assumed to be a vacuum. A rotating magnetic field will create a strong electric field that may be capable of pulling out charged particles from the stellar surface. If this happens, the pulsars are surrounded by a plasma that will have a very high conductivity. We are thus faced with a problem of a rotating compact object surrounded by a corotating plasma, and the net radiation emitted from the system should be taken into account all the processes operating in the magnetosphere filled with the plasma. There is so far no consistent quantitative pulsar model. The proposed models are for example a neutron star with the charge-starved electrosphere [83], or with the force-free magnetosphere, where the acceleration of particles and the emitting zones are localized in the very small spatial regions [50]. It is very difficult to judge correct one among many models only by theoretical approach.

Recent observations of about 100 pulsars by the *Fermi Gamma-ray Space Telescope* [1] have revealed details of the structure of the emission region. The pulsed emission in the GeV energy band is an important tool for probing the particle acceleration and dissipation processes in the pulsar magnetosphere, since the maximum energy is determined by the acceleration-radiation-reaction limit for typical energetic pulsars. The γ-ray emission region has therefore been explored by comparing theoretical models with the observed light curve (e.g., [169, 162, 127]).

The pulsed emission is also detected in other energy bands (X-ray, ultraviolet, optical and radio) for some sources (e.g., [158]). The spectral features are non-thermal expect for the soft X-ray range, and the light curves from a single object are, in general, different from one energy band to another. For example, profiles of the light curve in one spin period are different in the γ-ray and X-ray ranges in the Vela pulsar [5]. The peak phase of different energy range is expected to coincide, since the emitting particles are related to a pair cascade process. However, the observation shows that the phase depends on the energy bands. This means that their emission regions are not the same. Complete understanding of light curve behavior in multi-wavelength bands can provide valuable information about the particle acceleration region. Note that we do not discuss soft X-rays, which are believed to be thermal radiation from the neutron star surface (e.g., [69]).

Possible origins of non-thermal pulsed emissions have been considered in the polar cap [39], slot gap [111], outer gap [30] and so on [18, 118, 43, 36, 34]. Recent *Fermi* observations with high γ-ray photon number statistics have showed that the phase-averaged spectrum above 200 MeV is well fitted by a power law plus exponential cut off, and that a cutoff shape sharper than a simple exponential is rejected with high significance (e.g., [5]). Furthermore, MAGIC and VERITAS detect γ-ray photons up to 400GeV from Crab pulsar [13, 11]. These observations rule out the near-surface emission proposed in polar cap cascade models [39], which would exhibit a much sharp spectral cutoff due to magnetic pair-production attenuation. Thus, pulsed γ-ray emission originates in the outer magnetosphere, as considered in the outer gap model.

Takata et al. (2008 [152], hereafter TCS08) considered a three-dimensional geometrical emission model to fit the observed light curves at different energy bands. The model is extended with some model parameters from the gap structure calculated in a two-dimensional meridian plane. By comparing the light curves of the Vela pulsar, they found that the X-ray emission is produced by both inward and outward emissions from the gap region, and that UV/optical emission originates from secondary pairs at a higher altitude. The number of light curves of pulsars observed at γ-ray and other energy bands is increasing thanks to *Fermi*, so that it is worthwhile to investigate whether outer gap model is applicable to other sources.

In this thesis, we investigate the structure of pulsar magnetosphere, especially the emission regions of several pulsars. We use the simplified model of TCS08 to fit to the observed multi-wavelength light curves. In this model, we have to specify the locations of the upper and lower boundaries of the gap region where the non-corotation potential is zero. Therefore, we explicitly introduce the altitude of the gap region as a parameter, in order to fit the observational data easily. The light curves also depend on the dipole inclination and viewing angles. In our method, such parameters are eliminated by other observational data, and only the altitude is changed for the fitting. In most studies, the lower boundary of the emission region is chosen as the surface of the last-open field lines of the rotating dipole (e.g., [152, 127]). In this thesis, however, the altitude is allowed to be in a wide range in order to explore the possible deviation of magnetic field line structure from that of a rotating dipole in vacuum.

The thesis is structured as follows. The mechanisms of high-energy radiation and the pair-creation processes will be reviewed in section 2. A brief review of pulsars is given in section 3. In section 4, we describe the model assumptions and parameters. In section 5, we compare the peaks of light curves with those observed at multiple wavelengths and determine the altitude of the emission region. Discussion is presented in section 6. Conclusions are given in section 7.

2 BASIC PHYSICAL PROCESSES

2.1 Emission Mechanisms

We briefly describe some emission mechanisms, which are responsible for the observation of the pulsar magnetosphere.

2.1.1 Synchrotron radiation

Considering that a charged particle moves in magnetic field, the trajectory is circular on projected plane, which is perpendicular to magnetic field. The radiation is emitted by the particle with relativistic energy and the direction is beamed along the velocity. This is called synchrotron radiation. The characteristic frequency $\omega_{\rm syn}$ and the energy spectrum $F_{{\rm syn},\omega}$ from a single electron with mass $m_{\rm e}$, charge $-e$ and energy $\gamma m_{\rm e}c^2$ can be written as (see e.g., [130])

$$\omega_{\rm syn} = \frac{3}{2}\gamma^3\omega_{\rm B}\sin\alpha_{\rm p}, \tag{1}$$

$$F_{{\rm syn},\omega} = \frac{\sqrt{3}}{2\pi}\frac{e^3 B\sin\alpha_{\rm p}}{m_{\rm e}c^2}F\left(\frac{\omega}{\omega_{\rm syn}}\right), \tag{2}$$

$$\tag{3}$$

where

$$\omega_{\rm B} = \frac{eB}{\gamma m_{\rm e}c}, \tag{4}$$

is the gyration frequency, $\alpha_{\rm p}$ is the pitch angle of the electron with respect to the magnetic field B and function $F(x)$ is

$$F(x) = x\int_x^\infty K_{5/3}(\xi)d\xi. \tag{5}$$

In eq.(5), $K_{5/3}(\xi)$ is the modified Bessel function of the second kind with an order of 5/3.

The total radiative power $F_{\rm syn}$ is

$$F_{\rm syn} = \int_0^\infty F_{{\rm syn},\omega}d\omega = \frac{2e^2}{3c^3}\gamma^4\omega_{\rm B}^2 v_\perp^2, \tag{6}$$

where $v_\perp$ is electron velocity perpendicular to the magnetic field. If γ is so large, radiative drag force cannot be negligible. The drag force $f_{\rm rad,syn}$ for the synchrotron radiation is

$$\mathbf{f}_{\rm rad,syn} = -\frac{F_{\rm syn}}{c}\hat{\mathbf{v}}_\perp = -\frac{2e^2}{3}\gamma^4\left(\frac{\omega_{\rm B}}{c}\right)^2\left(\frac{v_\perp}{c}\right)^2\hat{\mathbf{v}}_\perp, \tag{7}$$

where $\hat{\mathbf{v}}_\perp$ is unit vector along the direction of $v_\perp$.

As described in section, magnetic field in the pulsar magnetosphere is so large that the synchrotron lifetime $\tau_{\rm syn}$ is very small. Using typical values for Lorentz factor and field strength B, the lifetime is

$$\tau_{\rm syn} = \frac{\gamma m_{\rm e}c^2}{F_{\rm syn}} \sim 5.2\times10^{-23}\left(\frac{\gamma}{10^7}\right)^{-1}\left(\frac{B}{10^{12}{\rm G}}\right)^{-2}{\rm s}. \tag{8}$$

2.1.2 Curvature radiation

In section 2.1.1, we implicitly assume that particle gyroradius $r_{\mathrm{B}} = c/\omega_{\mathrm{B}}$ is much smaller than curvature radius R_{cur} of magnetic field line. In pulsar magnetosphere, synchrotron lifetime eq.(8) is so small that the particle motion is limited to along the magnetic field lines and electric drift in a transverse direction. Therefore, gyroradius r_{B} is much larger than curvature radius R_{cur} of the magnetic field line for most particles in pulsar magnetosphere. In this case, the relativistic particle motion along a curved trajectory gives rise to the emission due to so-called curvature radiation. This process is quite analogous to the ordinary synchrotron radiation, irrespective of the origin of the acceleration. Therefore, all formula for the synchrotron radiation can be used to describe the curvature radiation only by changing the gyroradius r_{B} to the curvature radius R_{cur}. The characteristic frequency ω_{cur} and the energy spectrum $F_{\mathrm{cur},\omega}$ of the curvature radiation from a single electron can be written as

$$\begin{aligned} \omega_{\mathrm{cur}} &= \frac{3c}{2R_{\mathrm{cur}}}\gamma^3, && (9) \\ F_{\mathrm{cur},\omega} &= \frac{\sqrt{3}}{2\pi}\frac{e^2 c\gamma}{R_{\mathrm{cur}}} F\left(\frac{\omega}{\omega_{\mathrm{cur}}}\right). && (10) \\ & && (11) \end{aligned}$$

The radiation drag force for curvature radiation $f_{\mathrm{rad,cur}}$ is

$$\mathbf{f}_{\mathrm{rad,cur}} = -\frac{F_{\mathrm{cur}}}{c}\hat{\mathbf{v}} = -\frac{2e^2}{3R_{\mathrm{cur}}}\gamma^4\hat{\mathbf{v}}. \tag{12}$$

2.2 Pair Creation Processes

In this subsection, we briefly describe two kinds of pair-creation process, by strong magnetic field and by photons.

2.2.1 Magnetic pair-creation

When a photon moves across the strong magnetic field, electron-positron pair is generated by one-photon,

$$\gamma + B \to e^+ + e^- + B. \tag{13}$$

The conversion probability (per unit length) of a photon with energy ϵ_{ph} (i.e., for $\epsilon >> 2m_{\mathrm{e}}c^2$) propagating at an angle θ to the magnetic field $\mathbf{B}$ is [23]

$$P_{\mathrm{B}} = \frac{3\sqrt{3}}{16\sqrt{2}}\frac{e^3 B\sin\theta}{\hbar m_{\mathrm{e}}c^2}\exp\left(-\frac{8}{3}\frac{B_{\mathrm{c}}}{B\sin\theta}\frac{m_{\mathrm{e}}c^2}{\epsilon_{\mathrm{ph}}}\right), \tag{14}$$

where

$$B_{\mathrm{c}} = \frac{m_{\mathrm{e}}^2 c^3}{e\hbar} \sim 4.4\times 10^{13}\mathrm{G} \tag{15}$$

corresponds to the critical magnetic field for which the energy gap between two Landau levels reaches the rest mass energy of an electron, $\hbar\gamma\omega_{\mathrm{B}} = m_{\mathrm{e}}c^2$. It is generally considered that pair-creating photons are generated by curvature radiation. Note that though the curvature photon is emitted locally parallel to the magnetic field lines, the angle θ to the magnetic field increase due to the curved field lines. On the other hand, for the photon mean-free-path $l_{\rm B}$ smaller than the curvature radius, we can take $\sin\theta \sim l_{\rm B}/R_{\rm cur}$. Therefore, $l_{\rm B}$ for the magnetic pair-creation can be estimated as [146]

$$l_{\rm B} = \frac{8}{3\Lambda} R_{\rm cur} \frac{B_{\rm c}}{B} \frac{m_{\rm e}c^2}{\epsilon_{\rm ph}}, \tag{16}$$

where $\Lambda \sim 20$ is a logarithmic factor. Using typical values, the mean free path is

$$\frac{l_{\rm B}}{R_{\rm NS}} \sim 0.1 \left(\frac{R_{\rm cur}}{10^8 {\rm cm}}\right) \left(\frac{B}{10^{12.5}{\rm G}}\right)^{-1} \left(\frac{R_{\rm NS}}{10^6 {\rm cm}}\right)^{-1}, \tag{17}$$

where $R_{\rm NS}$ is the radius of neutron star.

2.2.2 Photon-photon pair-creation

At relatively outer region in the pulsar magnetosphere, magnetic pair-creation process is not active. Instead, photon-photon pair creation occurs there by collision between high-energy γ-ray and X-ray photons.

Quantum electrodynamics [55, 70] gives the cross section as

$$\sigma_{\gamma\gamma}(s_{\rm col}) = \frac{1}{2}\pi r_{\rm e}^2 (1-\beta_{\rm cm}^2) \left[(3-\beta_{\rm cm}^4) \ln\left(\frac{1+\beta_{\rm cm}}{1-\beta_{\rm cm}}\right) - 2\beta_{\rm cm}(2-\beta_{\rm cm}^2) \right], \tag{18}$$

where $r_{\rm e}$ is classical electron radius, $\beta_{\rm cm} = (1-\gamma_{\rm cm}^{-2})^{1/2}$, $\gamma_{\rm cm}$ is the Lorentz factor in center of momentum frame of the produced electron and positron and $s_{\rm col} = \gamma_{\rm cm}^2$ is the characteristic non-dimensional value of interaction energy. The strength of a collision is characterized by the invariant energy $\sqrt{s_{\rm col,tot}}$, defined in terms of four-vectors $p_1^\mu = (\epsilon_1, \epsilon_1, 0, 0)$ and $p_2^\mu = (\epsilon, \epsilon\mu, \epsilon(1-\mu^2)^{1/2}, 0)$ in the units of $m_{\rm e}c^2$ by

$$s_{\rm col,tot} = (p_1^\mu + p_2^\mu)^2 = (\epsilon_1+\epsilon)^2 - (\epsilon_1+\epsilon\mu)^2 - \epsilon_1^2(1-\mu^2) = 2\epsilon\epsilon_1(1-\mu), \tag{19}$$

where $\theta = \arccos\mu$ is the interaction angle between the directions of ϵ_1 and ϵ. At threshold, two leptons are formed at rest with total energy $2m_{\rm e}c^2$, so that $s_{\rm col,tot} = 4$. Above threshold, $s_{\rm col,tot} = 4\gamma_{\rm cm}^2$. Hence

$$s_{\rm col} = \gamma_{\rm cm}^2 = \frac{1}{2}[\epsilon\epsilon_1(1-\mu)] = \frac{s_{\rm col,tot}}{4}. \tag{20}$$

The asymptotic cross section is

$$\sigma_{\gamma\gamma} = \pi r_{\rm e}^2 \begin{cases} \beta_{\rm cm}, & \beta_{\rm cm} \ll 1 \\ \frac{\ln 2s_{\rm col} - 1}{s_{\rm col}}, & s_{\rm col} \gg 1. \end{cases} \tag{21}$$

The cross section (eqs. 18 and 21) is plotted in figure 1, as a function of $s_{\rm col}$. For a γ-ray photon with energy ϵ_1 passing through a background of photons with energy ϵ and angle θ, the cross section is invariant with respect to fixed values of the interaction energy $s_{\rm col} = \epsilon\epsilon_1(1-\mu)/2$. Note the strong peaking of the cross section when $s_{\rm col} \sim 2$, consequently favors collisions near threshold. The assumption $s_{\rm col} \sim 2$ gives a good approximation to

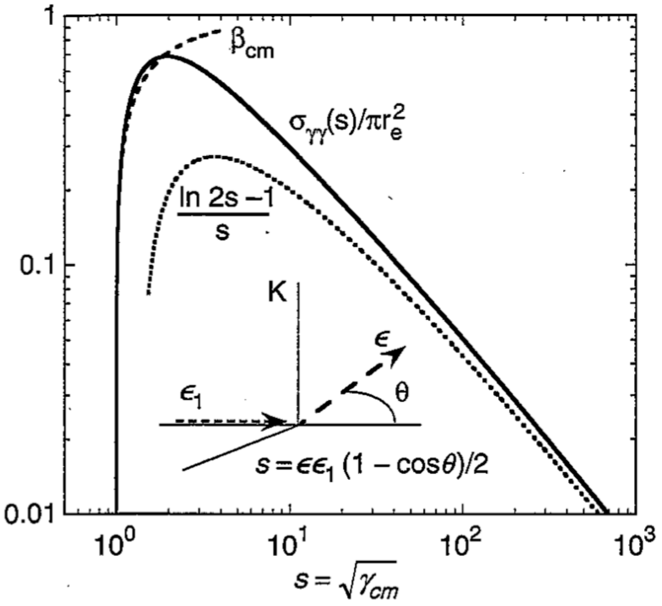

Figure 1: Cross section for photon-photon pair-production, $\sigma_{\gamma\gamma}$, as a function of invariant $s_{\rm col}$ (denoted s in this figure), along with asymptotes at $s_{\rm col} - 1 \ll 1$ and $s_{\rm col} \gg 1$.Figure adopted from Dermer & Menon (2009) [42].

this process except for hard spectrum of the target photons, for which the interactions of $s_{\rm col} \gg 1$ become important.

For γ-ray passing through isotropic photon fields, $s_{\rm col} \to \epsilon\epsilon_1$ for head-on collisions. An approximation, $s_{\rm col} \to \epsilon\epsilon_1/2$ (assuming typical collision angle $\theta \sim \pi/2$) gives an estimate for isotropic target photons. The threshold for pair creation in photon-photon processes is $\beta_{\rm cm} > 0$, $\gamma_{\rm cm} > 1$, implying $s_{\rm col} > 1$.

The absorption probability per unit path length is

$$\frac{d\tau_{\gamma\gamma}(\epsilon_1)}{dx} = \frac{\dot{N}_{\rm SC}}{c} = \oint d\Omega(1-\mu) \int_0^\infty d\epsilon n_{\rm ph}(\epsilon, \Omega)\sigma_{\gamma\gamma}(s_{\rm col}), \tag{22}$$

where $\dot{N}_{\rm SC}$ is the γ-ray absorption rate, $n_{\rm ph}(\epsilon, \Omega)$ is the number density of photons and the dependence on ϵ_1 is contained in the definition of $s_{\rm col}$, eq.(20). For an isotropic photon field, we have

$$\frac{d\tau_{\gamma\gamma}}{dx} = \frac{1}{2}\int_{-1}^{1} d\mu(1-\mu) \int_0^\infty d\epsilon n_{\rm ph}(\epsilon, \Omega)\sigma_{\gamma\gamma}(s_{\rm col}). \tag{23}$$

3 PULSARS

In this section, the current understanding of pulsars will be briefly described. We discuss three main areas: (a) In section 3.1, general pulsar properties derived by observational facts will be briefly summarized. (b) In section 3.2, the structure of pulsar magnetosphere from theoretical studies will be described. (c) In section 3.3, recent studies of emission region using gap models will be described. Some remarks in this section are added in section 3.4.

3.1 Observational Properties of Pulsars

3.1.1 Rotating magnetized neutron stars

Pulsars emit periodic radiation with very high accuracy. It is naturally considered that the well-regulated phenomenon is related to rotation of the objects. We can constrain the averaged density $\bar{\rho}$ of an object with mass M and radius R using the condition that gravity is larger than centrifugal force,

$$\bar{\rho} = \frac{3M}{4\pi R^3} > \frac{3\Omega^3}{4\pi G}, \tag{24}$$

where G is gravitational constant and Ω is angular velocity. The shortest period currently known is $P(= 2\pi/\Omega) = 1.39$ms (PSR J1748-2446ad [63]). This gives lower limit for the averaged density

$$\bar{\rho} > 7.3 \times 10^{13} \left(\frac{P}{1.39\text{ms}}\right)^{-2} \text{ g cm}^{-3}. \tag{25}$$

This value is comparable to the nucleus density.

In order to investigate the materials in such a high density object, we consider the composition with same number densities of proton, neutron and electron. For the simplification, we assume that temperature is zero. The relation of electron number density n_e and Fermi momentum p_F is

$$2 \times \frac{4\pi}{h^3} \int_0^{p_F} p^2 dp = n_e, \tag{26}$$

where h is Planck constant. Using eq.(26), Fermi momentum is

$$p_F = h \left(\frac{3}{8\pi} \frac{\rho}{(m_p + m_n)}\right)^{1/3}, \tag{27}$$

where m_p and m_n are proton and neutron mass, and density of objects ρ is

$$\rho = (m_p + m_n) n_e. \tag{28}$$

Using above equations, Fermi energy E_F is

$$\begin{aligned} E_F &= \sqrt{m_e^2 c^4 + p_F^2 c^2} \\ &\sim 200 \left(\frac{\rho}{10^{14}\text{g cm}^{-3}}\right)^{1/3} \text{MeV}, \end{aligned} \tag{29}$$

where m_e is electron mass. This E_F value is much larger than the difference between proton mass and neutron mass 1.29MeV. Under this situation, a proton captures a electron and

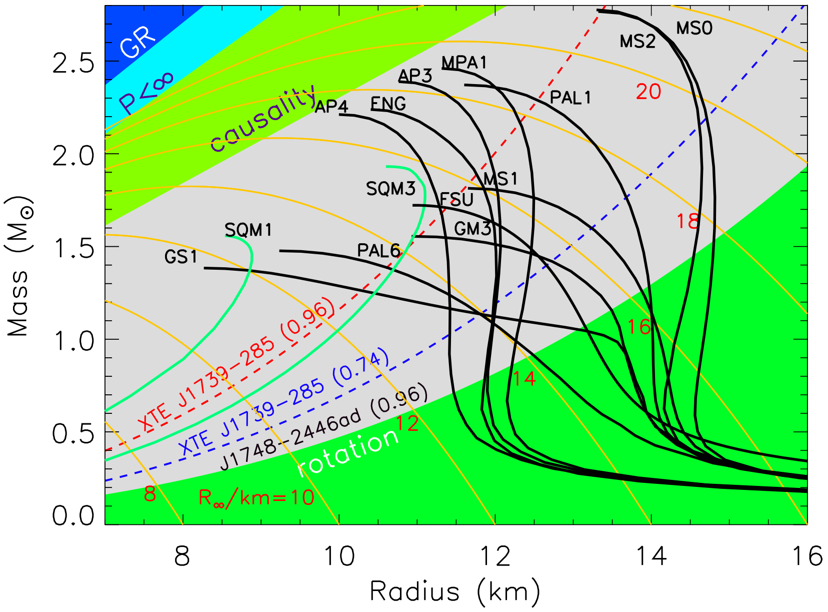

Figure 2: Mass-radius trajectories for typical equation of states (see Lattimer & Prakash (2001) [86] for notation) are shown as black curves. Green curves (SQM1, SQM3) are self-bound quark stars. Orange lines are contours of radiation radius, $R_\infty = R_{\rm NS}/\sqrt{1 - 2GM_{\rm NS}/R_{\rm NS}c^2}$. The dark region is excluded by the general relativity constraint $R_{\rm NS} > 2GM_{\rm NS}/c^2$, the light blue region is excluded by the finite pressure constraint $R_{\rm NS} > (9/4)GM_{\rm NS}/c^2$, and the green region is excluded by causality, $R_{\rm NS} > 2.9GM_{\rm NS}/c^2$. The light green region shows the region $R_{\rm NS} > R_{\rm max}$ excluded by the 716 Hz pulsar J1748-2446ad [63] using eq.(12) of Lattimer & Prakash (2007)[87]. The upper red dashed curve is the corresponding rotational limit for the 1122 Hz X-ray source XTE J1739-285 [73]; the lower blue dashed curve is the rigorous causal limit using the coefficient 0.74 ms in eq.(12) of Lattimer & Prakash (2007)[87]. Figure adopted from Lattimer & Prakash (2007)[87].

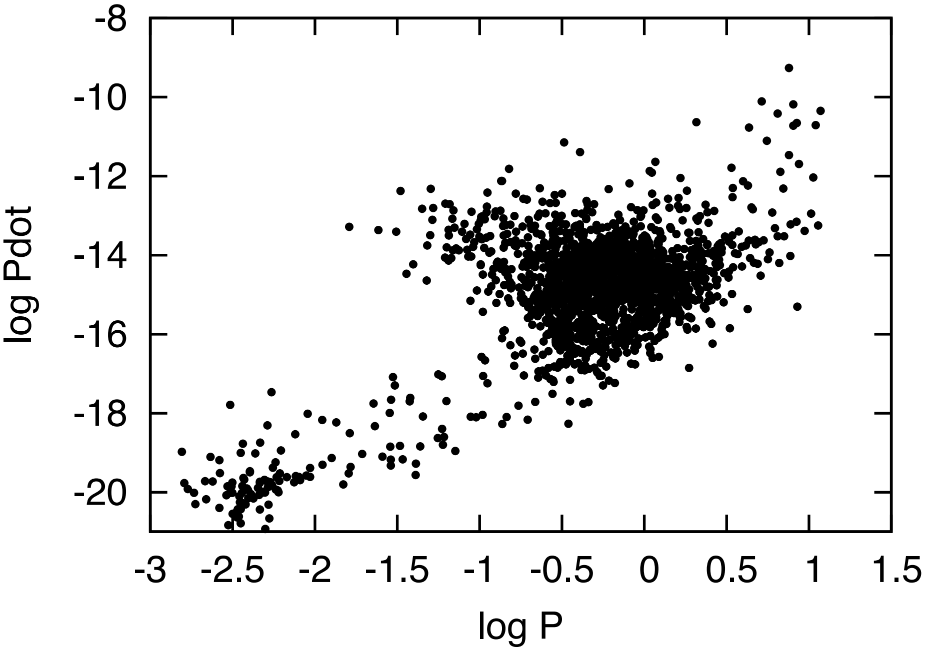

Figure 3: A plot of $\dot{P}$ versus P for pulsars, known as the P-$\dot{P}$ diagram. Data adopted from ATNF Pulsar Catalogue [97]

number of neutron increases. Therefore, it is generally believed that pulsars are rotating neutron stars.

In figure 2, we show the mass-radius relation of neutron star. Thereafter, we adopt $M_{\rm NS} = 1.4M_\odot$ and $R_{\rm NS} = 10^6$ cm for fiducial pulsars.

It has observationally known that spin period of pulsars increases with time. The P-$\dot{P}$ diagram is shown in figure 3. The spin-down luminosity associated with loss of rotational energy is

$$L_{\rm sd} = \frac{4\pi^2 I\dot{P}}{P^3} \sim 4.4 \times 10^{32} \left(\frac{P}{1{\rm s}}\right)^{-3} \left(\frac{\dot{P}}{10^{-14}{\rm ss}^{-1}}\right) \left(\frac{M_{\rm NS}}{1.4M_\odot}\right) \left(\frac{R_{\rm NS}}{10^6{\rm cm}}\right)^2 {\rm erg\ s}^{-1}, \tag{30}$$

where I is the moment of inertia, $I = (2/5)M_{\rm NS}R_{\rm NS}^2$. The spin-down luminosity may be estimated by magnetic-dipole radiation of a magnetized object rotating in vacuum,

$$L_{\rm sd} = \frac{32\pi^4 B_{\rm NS}^2 R_{\rm NS}^6}{3c^3P^4} \sin^2\alpha, \tag{31}$$

where $B_{\rm NS}$ is the magnetic field strength at the surface and α is the angle between rotation and magnetic axes. Even if vacuum model is very far from reality, this model gives an insight into the key properties of the real magnetosphere of the neutron star. Indeed, this luminosity is responsible for the energy release needed to supply the Crab Nebula with relativistic electrons [122]. Using eqs.(30) and (31) and assuming $\sin\alpha \sim 1$, the magnetic field strength can be estimated as

$$B_{\rm NS} = 3.4 \times 10^{12} \left(\frac{P}{1{\rm s}}\right)^{1/2} \left(\frac{\dot{P}}{10^{-14}{\rm ss}^{-1}}\right)^{1/2} \left(\frac{M_{\rm NS}}{1.4M_\odot}\right)^{1/2} \left(\frac{R_{\rm NS}}{10^6{\rm cm}}\right)^{-2} {\rm G}. \tag{32}$$

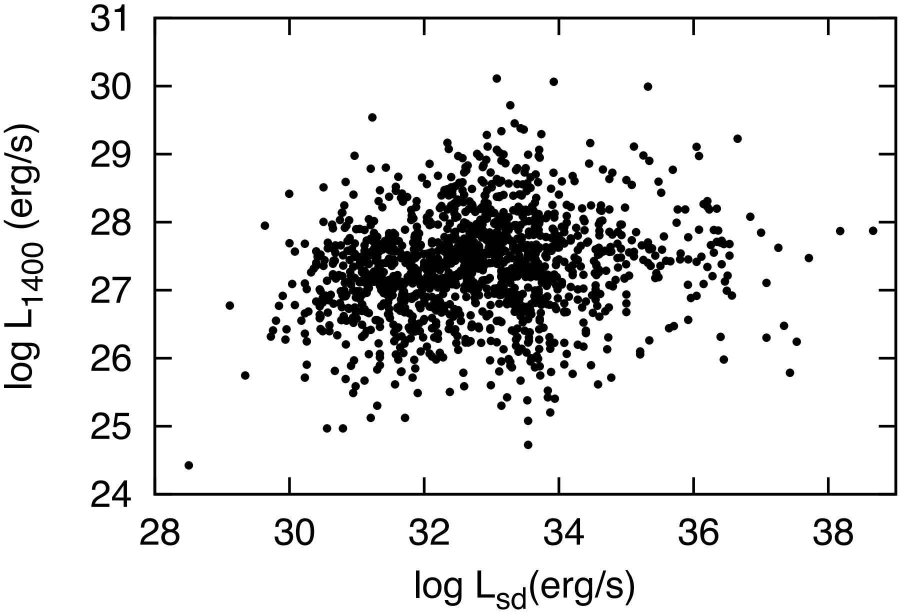

Figure 4: A plot of luminosity at 1400 MHz L_{1400} and spin-down luminosity $L_{\rm sd}$. Data adopted from ATNF Pulsar Catalogue [97]

Therefore, pulsars are considered as strongly magnetized neutron stars. Indeed, if the neutron star is supposed to evolve from a normal star (radius $R_{\rm s} \sim 10^{11}$ cm) with the magnetic field $B_{\rm s} \sim 100$G, from the conservation law of magnetic flux

$$R_{\rm s}^2 B_{\rm s} = R_{\rm NS}^2 B_{\rm NS}, \tag{33}$$

the magnetic field $B_{\rm NS}$ of the neutron star with $R_{\rm NS}$ is of order

$$B_{\rm NS} \sim \left(\frac{R_{\rm s}}{R_{\rm NS}}\right)^2 B_{\rm s} \sim 10^{12}{\rm G}. \tag{34}$$

If magnetic field decay can be neglected, we can estimate the spin-down age $\tau_{\rm c}$ from eq.(32) as

$$\tau_{\rm c} = \frac{P}{2\dot{P}} = 1.6 \times 10^6 \left(\frac{P}{1{\rm s}}\right)\left(\frac{\dot{P}}{10^{-14}{\rm ss}^{-1}}\right)^{-1} {\rm yr}. \tag{35}$$

For example, the spin-down age for Crab pulsar ($P = 0.033$s, $\dot{P} = 4.2 \times 10^{-13}{\rm ss}^{-1}$ [97]) is $\tau_{\rm c} \sim 10^3$ yr (assuming that initial spin period is negligibly small relative to current one). This value coincides with that of the Crab Nebula that came into existence, as is known, during the explosion of the historical supernova AD 1054.

3.1.2 Pulsed emission properties in each energy band

Radio Most pulsars, including first discovered pulsar [65], are detected at radio band. The intrinsic luminosity of radio emission is only 10^{-4}-10^{-6} of the spin-down luminosity.

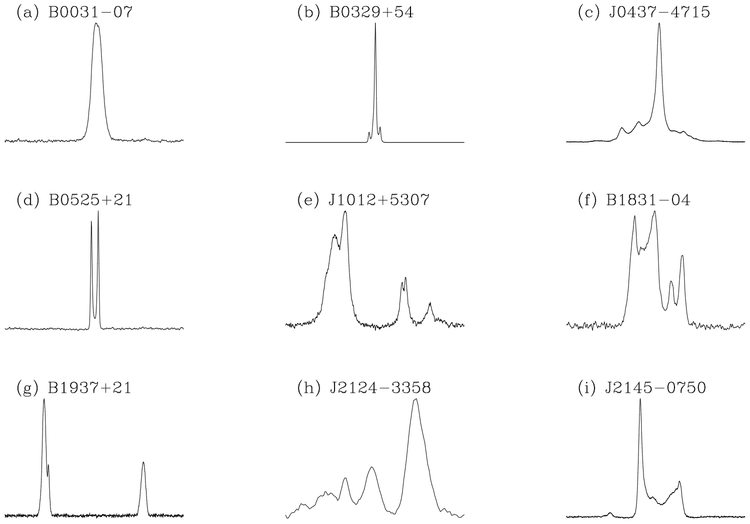

Figure 5: A variety of integrated pulse profiles taken from the available literature. References: Panels a, b, d, f [54], Panel c [19], Panels e, g, i [82], Panel h [22]. Each profile represents 360 degrees of rotational phase.

This corresponds to 10^{26}-10^{29} erg s^{-1}, which is 4-7 orders less than the luminosity of the Sun. We plot spin-down luminosity and radio luminosity L_{1400} at 1400 MHz in figure 4. The correlation between them is very weak and this is contrast to high-energy emission.

For a given pulsar, even though the individual pulses have different shapes, the integrated pulse profile is usually very stable for any observations at the same radio frequency. Some integrated pulse profiles at radio are shown in figure 5. The properties different from other wavelength are that pulse width are very narrow and that clear double-peak structure is relatively rare.

The physical generation mechanism of the radio pulses remains as a challenging problem. A requirement to any emission models is that the radiation should be coherent. If we receive a pulse of peak flux density S_{peak} with duration Δt from a given pulsar, the brightness temperature of the emission T_{b} is

$$\begin{aligned} T_{\mathrm{b}} &= \frac{S_{\mathrm{peak}}}{2\pi k_{\mathrm{B}}}\left(\frac{\nu\Delta t}{d}\right)^2 \\ &\sim 10^{24}\left(\frac{S_{\mathrm{peak}}}{\mathrm{Jy}}\right)\left(\frac{\nu}{\mathrm{GHz}}\right)^{-2}\left(\frac{\Delta t}{\mathrm{ms}}\right)^{-2}\left(\frac{d}{\mathrm{kpc}}\right)^2 \mathrm{K}, \end{aligned} \tag{36}$$

where ν is observed frequency and k_{B} is Boltzmann constant. Typically, brightness temperature is in the range 10^{23}-10^{26}K, which far exceeds the conceivable temperature of materials within the pulsar magnetosphere. A solution of this problem is to associate the radiation with some form of coherent radiation in which the particles radiate in bunches rather than singly. When N charged particles must bunch less than the wavelength of the emitted radiation, the intensity of the coherent radiation can be N^2 times that of an individual charge because the radiated power depends on the square of the oscillating charge. Alternatively,

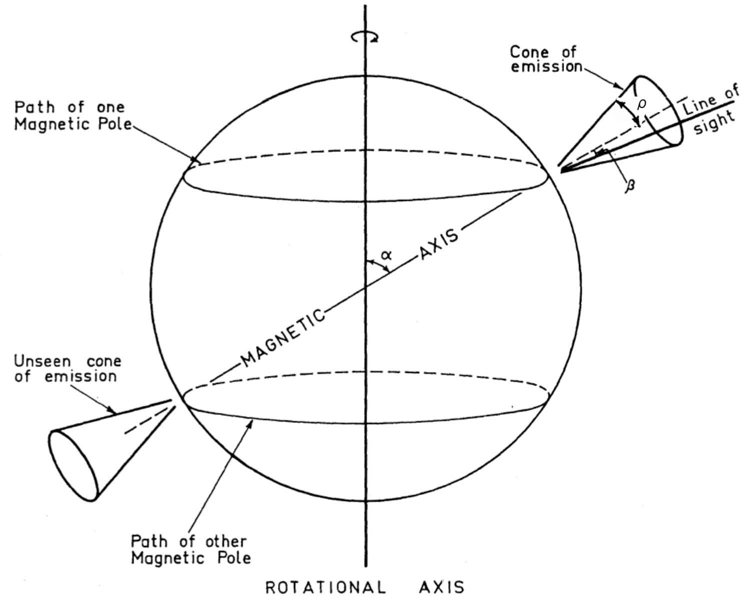

Figure 6: A phenomenological model for pulse shape morphology. The radiation beam is shown as a symmetrical cone, angular width $2\rho_{\text{cone}}$, at inclination angle α, cut by a line of sight with impact parameter β_{i} (denoted β in this figure). Figure adopted from Radhakrishnan & Cooke (1969) [121].

the emission might be some form of maser emission associated with plasma phenomena in the magnetosphere.

Although there is no common viewpoint on the nature of the pulsar coherent radio emission, it turned out that the basic observed properties of the radio emission could be interpreted by using phenomenological model. It is so-called hollow cone model [121]. In this model, the emission cone whose center corresponds to the magnetic axis is located near the neutron star surface. As will be described in detail in section 3.3, the secondary particle generation is impossible in the rectilinear magnetic field by two reasons; (1) the intensity of the curvature radiation is low, (2) the photon emitted by relativistic particles propagates at a small angle to the magnetic field. Therefore, as shown in figure 6, in the central regions of the open magnetic field lines, a decrease in secondary plasma density should be expected. If we make a rather reasonable assumption that the radio emission must be directly connected with the outflowing plasma density, there must be a decrease in the radio emission intensity in the center of the directivity pattern. Therefore, we should expect a single mean profile in pulsars in which the line of sight intersects the directivity pattern far from its center and the double profile for the central passage.

As a result, it was possible to explain the basic properties of the radio emission such as (a) the pulse width and even its statistical dependence on the pulsar period, and (b) the characteristic S-shaped change in the position angle of the linear polarization along the mean profile.

As to (a), the geometry of the radiation beam is shown in figure 6. The beam is shown as the section of a cone with angular width $2\rho_{\text{cone}}$, at an inclination angle α to the rotation

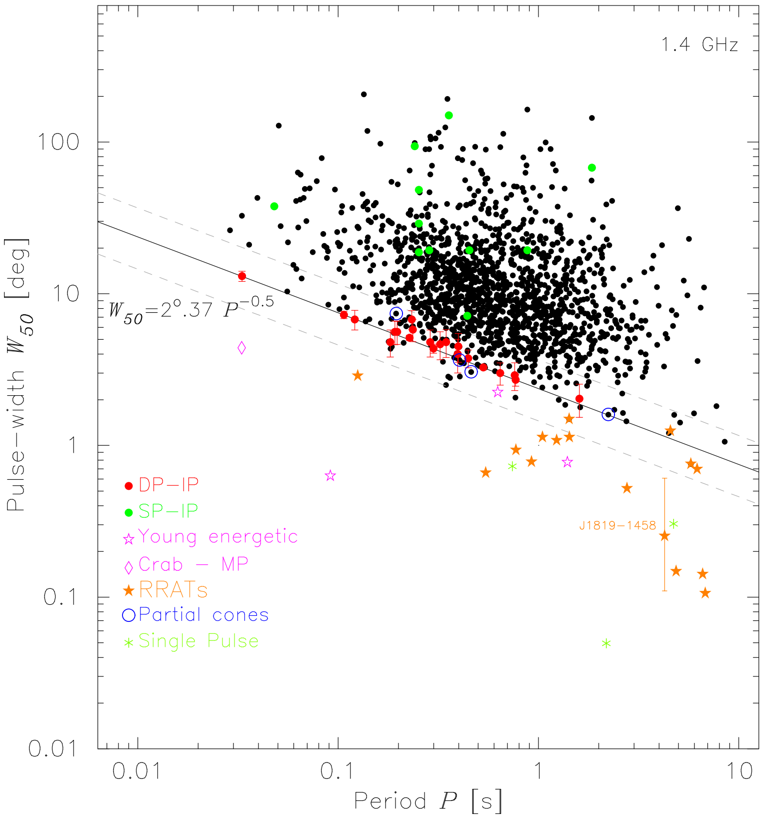

Figure 7: Plot of pulse-width W_{50} measured at 1.37 GHz for 1543 normal pulsars. Data of 1522 pulsars are from ATNF Pulsar Catalogue [97], and of 21 pulsars are from Maciesiak & Gil (2011) [96]. Figure adopted from Maciesiak & Gil (2011) [96].

Figure 8: Left: pulse profile at 1418MHz observed Arecibo (solid) of PSR J0659+1414, as well as the degree of linear polarization (dashed) and circular polarization (dotted). The bottom panel shows the P.A. of the linear polarization and an rotating vector model fit. Figure adopted from Weltevrede et al. (2010) [173]. Right: the geometrical model for polarization position angle, showing the polarization position angle ψ of linearly polarized radiation from a single point P, which moves across the arc ST as the pulsar rotates. The zero of longitude ϕ is defined as the meridian through the magnetic axis, and the position angle PRQ=ψ is measured with respect to the projected direction of the rotation axis ψ_0. The conical emission beam has an opening semi-angle $\rho_{\rm cone}$ (denoted ρ in right figure). The swing of polarization position angle depends on the inclination angle α and the impact parameter $\beta_{\rm i}$ (denoted β in the right figure), which is the closest approach between the observer direction and the magnetic axes. Figure adopted from Lyne & Manchester (1988) [95]

axis. The line of sight cuts the beam at an impact angle $\beta_{\rm i}$ to the center of the cone. The angle $\rho_{\rm cone}$ of the radiating cone can be determined from the observed profile width W by the relation

$$\rho_{\rm cone} = 2\sin^{-1}\left[\sin^2\frac{W}{4}\sin\alpha\sin(\alpha+\beta_{\rm i}) + \sin^2\frac{\beta_{\rm i}}{2}\right]^{1/2}. \tag{37}$$

This relation depends on both α and $\beta_{\rm i}$. This accounts for a large part of the scatter in the observed beamwidth, for example in the half-power widths W_{50} shown in figure 7. However, in some pulsars the inclination is known to be close to 90 degrees, since the presence of an interpulse shows that radiation is received from both poles. These pulsars are shown as red points in figure 7. Considering only these pulsars, the wide scatter is reduced and clearly defined lower limit gives a beamwidth $\propto P^{-0.5}$. This dependence agrees with eq.(59).

As to (b), the very high degree of polarization of many pulsars, notably in the youngest, is detected. For example, an integrated pulse profile of PSR J0659+1414 is shown in the left panel of figure 8. This figure also shows the integrated polarization, with the linearly and circularly polarized components respectively shown by dashed and dotted lines. This pulsar is typical in its degree of linear polarization, which approaches ∼100%, and in its almost monotonic sweep of position angle seen in the left panel of figure 8. The position angle of the linear component appears to be closely linked to the orientation of the dipolar magnetic field at the emitter, and the changing position angle through the observed beam can be related to that of the magnetic field direction with the rotation of emitting region. The change and in particular time variation of the position angle at the center of the beam, are related by simple geometry to the angle of inclination α and impact parameter $\beta_{\rm i}$, which is angle between magnetic axis and line of sight.

Radhakrishnan & Cooke (1969) [121] showed that the sweep of position angle could be fitted by a remarkably simple model, now generally known as the rotating vector model (RVM), based on the Hollow cone model. This relates the polarization vector to the position angle of a portion of a single magnetic field line, which is supposed to be the sole source of emission. As the single vector crosses the line of sight, its projected position angle changes smoothly, in an S-shaped curve, up to 180 degrees. The rate of change at the center of the curve mainly depends on the closest angular approach of the line of sight to the magnetic pole, providing an important indicator of the geometry of the rotating pulsar, inclination angle α and viewing angle ζ. The geometry of the RVM is shown in the right panel of figure 8. A simple expression for the position angle ψ is obtained using the viewing angle $\zeta = \alpha + \beta_{\rm i}$, which is the inclination of the observer direction to the rotation axis:

$$\tan(\psi - \psi_0) = \frac{\sin\phi \sin\alpha}{\sin\zeta\cos\alpha - \cos\zeta\sin\alpha\cos\phi}, \tag{38}$$

where ψ_0 is the projection direction of the rotation axis. An example of fitting result is shown in the left lower panel of figure 8. Therefore, in this thesis, we assume that the radio emission region is located near the magnetic pole based on the Hollow cone model.

Note that in the observed light curve, the reference phase $\phi = 0$ is assumed to be located at the peak maximum of radio emission in most studies (e.g., [2]). However, in the model, the conventional reference phase $\phi = 0$ occurs when the magnetic axis, spin axis, and line of sight lie all in the same plane. This preference phase does not agree with observational one. Since it is generally assumed that radio emissions arise at non-zero altitude in most empirical studies. This fact is important for the discussion about the peak separation between radio and other wavelength (e.g., [168]).

GeV γ-ray GeV γ-ray emission is a very important tool for the investigation of the particle acceleration region. First reason is that, most energy emitted from pulsars is in 0.01-10 GeV range. Figure 9 shows spectra for seven γ-ray pulsars, plotted as $\log \nu S_\nu$ against $\log \nu$ (the lower horizontal scale gives the logarithm of the energy in keV). The observed luminosity of γ-ray emission is $\sim 10^{-1}$ of the spin-down luminosity. Figure 10 shows the observed γ-ray luminosity above 100MeV and spin-down luminosity. Note that in most models described in section 3.3, observed γ-ray luminosity is not always consistent to intrinsic γ-ray luminosity because of non-uniform beam shape. In figure 10, we have here assumed uniformly phase-averaged beaming across the sky (beaming factor $f_\Omega = 1$) as a rough indication. Second reason is that, GeV photons are emitted by curvature radiation process from the particles with the maximum Lorentz factor. The maximum Lorentz factor of particles is derived by the condition that acceleration force $eE_\parallel$ equals to the radiation drag force for curvature radiation, where $E_\parallel$ is electric field component parallel to magnetic field. Although the radiation drag force for inverse Compton scattering also works, it is not significant for almost all γ-ray pulsars [93]. For typical γ-ray pulsars, the maximum Lorentz factor is

$$\gamma \sim 2.8 \times 10^7 \left(\frac{P}{0.1{\rm s}}\right)^{-1/4} \left(\frac{R_{\rm cur}}{R_{\rm LC}}\right)^{1/2} \left[\frac{\eta_{\rm acc}}{0.1}\frac{B_{\rm NS}}{10^{12}{\rm G}}\left(\frac{r}{R_{\rm LC}}\right)^{-3}\right]^{1/4}, \tag{39}$$

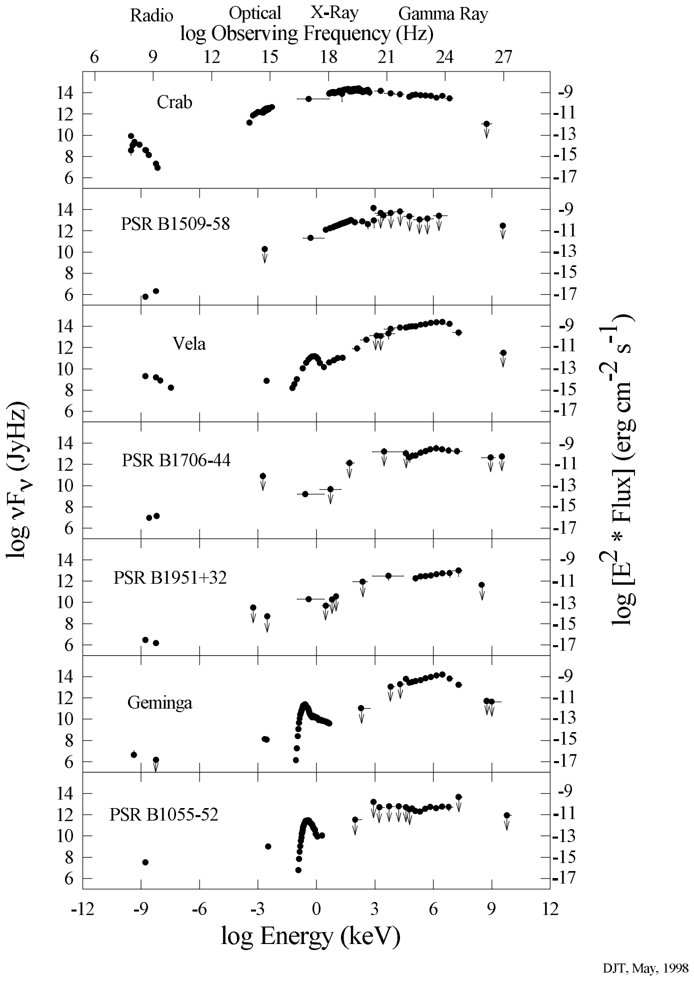

Figure 9: Spectra of seven pulsars plotted as $\log \nu S_\nu$ against $\log \nu$ (on the lower horizontal scale, log energy in keV). Figure adopted from Thompson et al. (1999) [159].

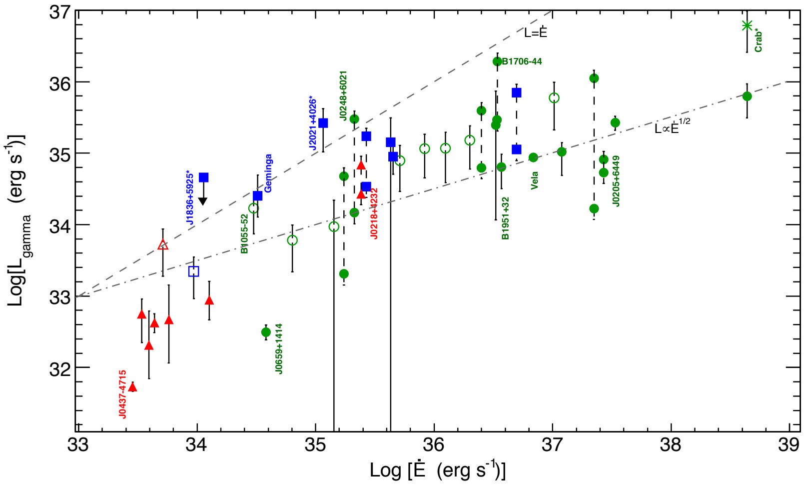

Figure 10: Observed pulsar luminosities above 100MeV plotted against the spin-down luminosity $L_{\rm sd}$. Observed luminosities are calculated using the beaming correction factor $f_\Omega = 1$. Figure adopted from Abdo et al. (2010a) [2].

where we define $E_\parallel = \eta_{\rm acc} B$ for accelerating electric field and generally $\eta_{\rm acc} < 1$. The characteristic energy of curvature radiation $E_{\rm cur} = \hbar\omega_{\rm cur}$ for the particle is

$$E_{\rm cur} \sim 1.4{\rm GeV} \left(\frac{P}{0.1{\rm s}}\right)^{-7/4} \left(\frac{R_{\rm cur}}{R_{\rm LC}}\right)^{1/2} \left[\frac{\eta_{\rm acc}}{0.1} \frac{B_{\rm NS}}{10^{12}{\rm G}} \left(\frac{r}{R_{\rm LC}}\right)^{-3}\right]^{3/4} . \tag{40}$$

Therefore, pulsed GeV emission comes from particle acceleration site in pulsar magnetosphere.

Before *Fermi* launched, detected γ-ray pulsars were only seven, shown in figure 9. However in two-years observation by *Fermi*, more than eighty γ-ray pulsars were detected [1]. Three main properties brought out by *Fermi* observations are that,

- a half of γ-ray pulsars are not detected in radio band [9, 131, 123].
- most γ-ray pulsars show double-peak structure and γ-ray peaks are not generally aligned with radio peak [2].
- spectral shape can be fitted by power-law + exponential cutoff, ruling out the super-exponential cutoff [5].

The physical meaning of these properties will be discussed in section V.

Hard X-ray X-ray spectra of pulsars can be fitted as (one or two) blackbody + power-law. In this subsection we focus on the power-law component. Blackbody component is discussed next.

About 70 pulsars with power-law component in X-ray range are so far detected [20]. However, X-ray follow-up observations of γ-ray pulsars are now proceeding [98], so that

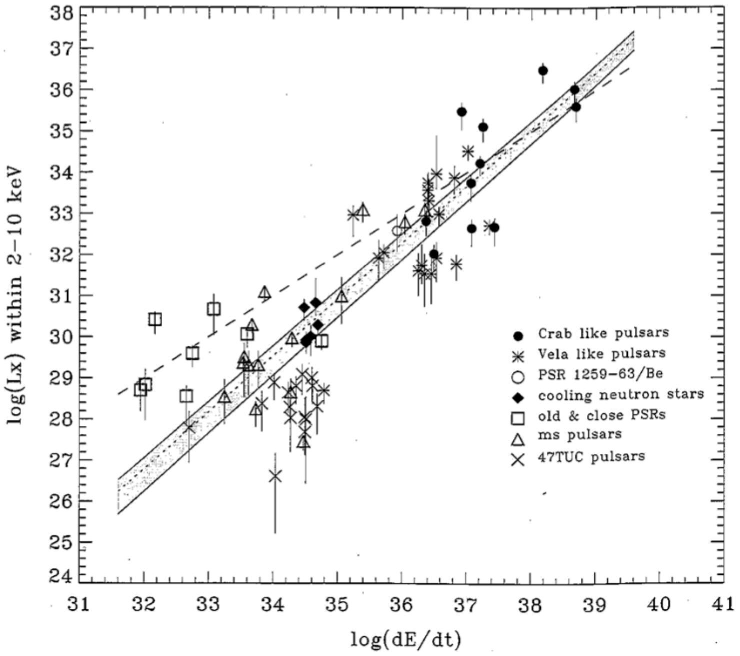

Figure 11: Observed pulsar luminosities at 2-10keV plotted against the spin-down luminosity $L_{\rm sd}$. Observed luminosities are calculated using the beaming correction factor $f_\Omega = 1$. The dashed line represents $L_x = 10^{-3} L_{\rm sd}$. The dotted line and gray shaded bar represent the linear correlation $L_x(2-10\text{keV}) = 10^{-15.72} L_{\rm sd}^{1.336}$ and its 1σ range. Figure adopted from Becker (2009) [20].

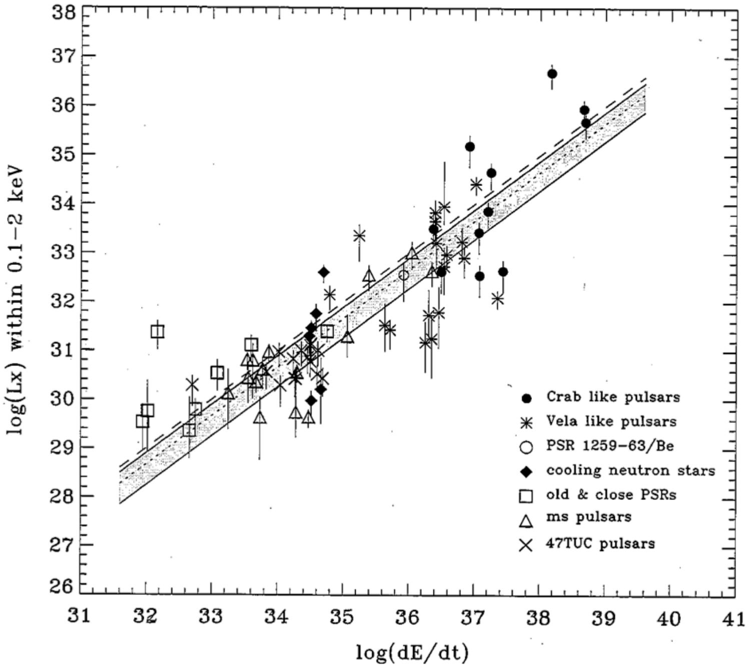

Figure 12: Observed pulsar luminosities at 0.1-2keV plotted against the spin-down luminosity $L_{\rm sd}$. The dashed line represents $L_x = 10^{-3} L_{\rm sd}$. The dotted line and gray shaded bar represent the linear correlation L_x(0.1-2keV)= $10^{-3.24} L_{\rm sd}^{0.997}$ and its 1σ uncertainty range. Figure adopted from Becker (2009) [20].

the number of non-thermal X-ray emitting pulsars will increase in near future. Observed hard X-ray luminosities are ~0.1% of the spin-down luminosities. Figure 11 shows both luminosities, and suggests a relationship between them. The best-fitted linear correlation is

$$L_x(2 - 10\text{keV}) = 10^{-15.72^{+0.7}_{-1.7}} L_{\rm sd}^{1.336^{+0.0036}_{-0.0014}}. \tag{41}$$

Because of a smaller contribution from thermal spectral components above ~2keV, the scatter in the data points below $\sim 10^{35}$ erg s^{-1} seems larger.

Observed shape of light curve in hard X-ray is relatively narrow and very similar to that in γ-ray. However, phases of hard X-ray peaks are not always aligned to that of γ-ray peaks. This feature is important information for the picture of electromagnetic cascade in the particle acceleration region. The non-thermal emission is considered as either synchrotron radiation or inverse Compton scattering of secondary particles (e.g., [150]). The synchrotron emitting particles are newly created pairs (e.g., [150]) and resonant cyclotron scattered particles by radio photons from magnetic pole (e.g., [60]). Radiative efficiency of each mechanism is different for different region. Therefore, information of both γ-ray and X-ray peak phases are important to understand which mechanisms are efficient in the pulsar magnetosphere.

Soft X-ray Thermal X-ray emission is detected from about 100 pulsars (e.g., [20]). Like the hard X-ray, observed thermal luminosity is linearly correlated with the spin-down luminosity, as shown in figure 12. Observed light curve shows sinusoidal curve, different from that of other wavelengths. The reason is that beaming effect is not operated for the thermal emission. The light curve shape roughly represents the emission from neutron star surface. The origin of pulse shape is believed to be hotter magnetic pole region than the overall surface (e.g., [69]). Although thermal emission is important for estimating the effect of polar cap heating due to return current and for seed photons of the photon-photon pair creation process, we do not discuss about soft X-ray emission in this thesis. The connection for particle acceleration region will be investigated in future works.

UV/optical So far, only 12 rotation-powered pulsars are detected in UV/optical band [104]. The pulses are detected for Crab [35], Vela [165], B0540+69 located in LMC [53], Geminga and B0656+14 [134, 135, 76]. Typical observed luminosities are 10^{-6}-10^{-7} of spin-down luminosities, with a little dependence on age [104]. The radiation is considered as synchrotron by non-thermal particles [152].

Most pulse profiles show double-peak structure. Peaks are relatively broad and are not generally aligned to those in γ-ray and X-ray. An important feature is that the power-law component fitted in the optical spectrum is not always consistent with the extrapolation of the power-law component in the X-ray spectrum (figure 13 [107]). The presence of two power-law components clearly indicates a break in the magnetospheric spectrum. No evident correlation is found between the optical power-law spectral index and the characteristic age [106]. Therefore, the origin of spectral break is not yet understood.

Sub-TeV γ-ray Very recently, pulsed emission at energy 25-400 GeV from the Crab pulsar was detected by the observations with the VERITAS and MAGIC arrays of Cherenkov telescopes [13, 11, 12]. Figure 14 shows the spectrum. The characteristic energy of curvature radiation for the pulsar is

$$E_{\mathrm{cur}} \sim 26.6\mathrm{GeV}\left(\frac{\eta_{\mathrm{acc}}}{0.1}\right)^{3/4}\left(\frac{r}{R_{\mathrm{LC}}}\right)^{-2}, \tag{42}$$

where we use $R_{\mathrm{cur}} = (rR_{\mathrm{LC}})^{1/2}$ for static dipole approximation. If 400GeV photons are emitted by curvature radiation process, radial distance to the emission region is $r \sim 0.25R_{\mathrm{LC}} \sim 40R_{\mathrm{NS}}$. Since 400 GeV photons have to be absorbed due to magnetic pair creation process at $r < 70R_{\mathrm{NS}}$ for the magnetic field $B_{\mathrm{NS}} \sim 3\times10^{12}$G [88], the curvature radiation is unlikely to the origin of the emissions.

Possible ideas, inverse Compton scattering of secondary and tertiary particles [93, 11, 12] in magnetosphere and bulk Comptonization in wind region [28] are proposed. Since this emission is so far detected in the Crab pulsar only, we do no more discuss this energy range.

3.2 Pulsar Magnetosphere

3.2.1 Goldreich-Julian Critique

The pulsar model described in section 3.1.1 is based on approximations, the vacuum exterior of it and free escape of radiation. In this subsection, we will describe that this approximation is not valid based on Goldreich-Julian critique [50]. Here we use a simple model for the

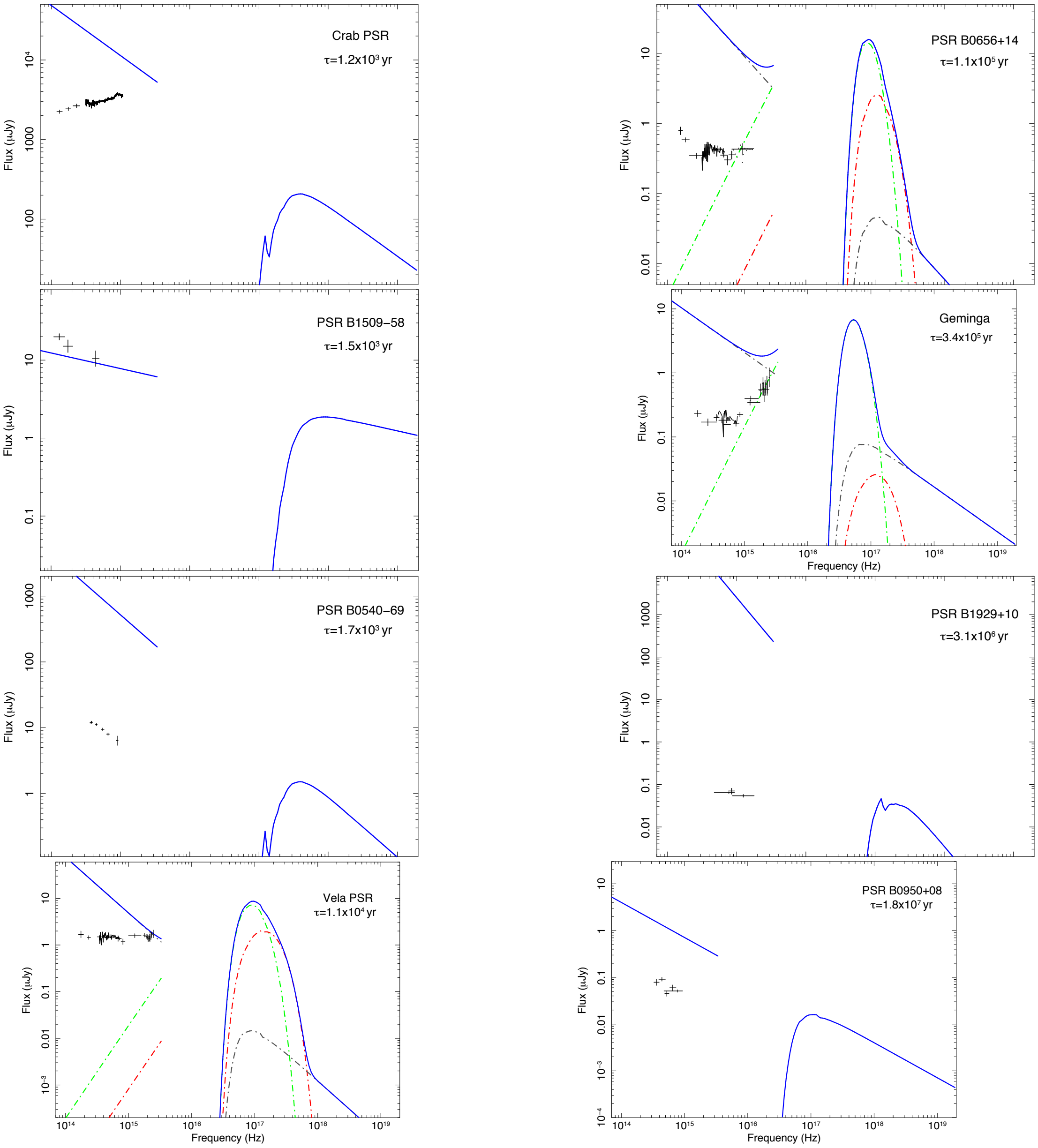

Figure 13: Optical spectral energy distribution of all rotation powered pulsars with an optical counterpart and flux measurements in at least two bands. Different X-ray spectral components are shown by the dotted red, green (blackbody), and blue (power-law) lines while the solid blue lines show the composite spectra. Only best-fits are plotted for clarity. Figure adopted from Mignani et al. (2010) [107].

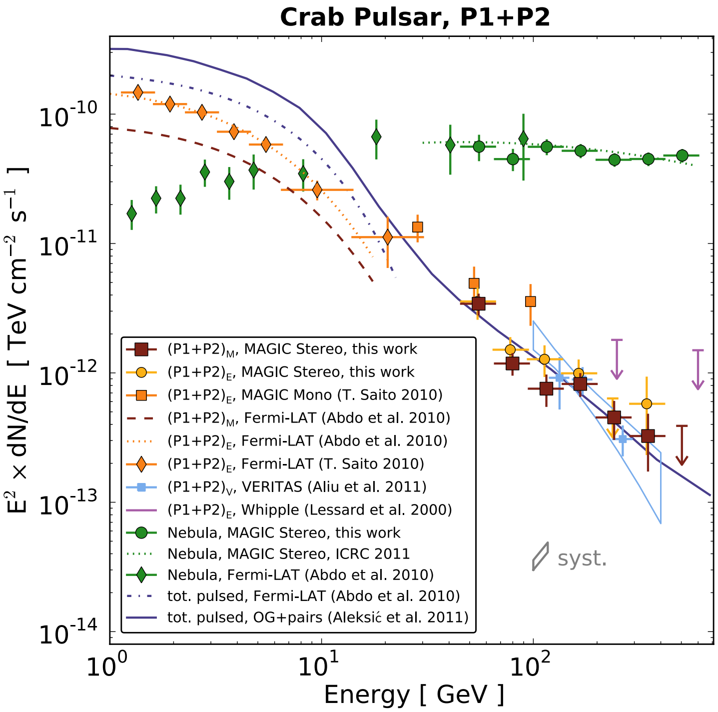

Figure 14: Compilation of spectral measurements of MAGIC and Fermi-LAT for both two peaks together. The VERITAS spectrum is also shown. For comparison, the Crab Nebula measurements of MAGIC and FERMI-LAT are also shown. Figure adopted from Aleksić (2011) [12].

pulsar magnetosphere by treating the neutron star as a conducting, rotating sphere of mass $M_{\rm NS}$, radius $R_{\rm NS}$, angular velocity Ω and with a surface magnetic field $B_{\rm NS}$. The inner magnetic-field configuration is assumed to be uniform with $\mathbf{B} = B_{\rm NS}\mathbf{e}_z$, where both magnetic and rotation axes are aligned with the z-axis. The outer magnetic field is dipolar with the moment $\mu_{\rm dip} = B_{\rm NS}R_{\rm NS}^3$. We start with the assumption that the exterior is vacuum. Then, we solve Maxwell's equations both inside and outside a rotating spherical conductor and match the solutions at the surface. Because the surface gravity of a neutron star is $g_{\rm NS} = (GM_{\rm NS}/R_{\rm NS}^2) \sim 1.9 \times 10^{14}$cm s^{-2}, the scale height of the hydrogen atmosphere at a temperature T is $H_{\rm atm} = (k_B T/m_H g_{\rm NS}) \sim 0.4(T/10^6{\rm K})$ cm. This is smaller than the other relevant length scales in the problem and hence the boundary between the conductor and vacuum can be thought of as a sharp discontinuity.

The velocity at any point $\mathbf{r}$ in the conductor, corresponding to the uniform rotation, is given by $\mathbf{v} = \mathbf{\Omega}\times\mathbf{r} = (\Omega r\sin\theta)\mathbf{e}_\phi$, where the standard spherical coordinates (r, θ, ϕ) is used. When the neutron star rotates, a particle with charge q in the interior feels a Lorentz force $(q/c)(\mathbf{v}\times\mathbf{B})$ and the motion generates an electric field $\mathbf{E}$ compensated for the magnetic force. The vanishing of the net force implies that

$$\mathbf{E} = -\frac{\mathbf{v}\times\mathbf{B}}{c} = -\frac{\mathbf{\Omega}\times\mathbf{r}}{c}\times\mathbf{B} = -\frac{\Omega B_{\rm NS} r\sin\theta}{c}(\sin\theta\mathbf{e}_r + \cos\theta\mathbf{e}_\theta). \tag{43}$$

This electric field satisfies the condition $\nabla\times\mathbf{E} = 0$ and hence can be expressed as $\mathbf{E} = -\nabla\phi_{\rm in}(r,\theta)$. Integrating along $r\sin\theta$ from the origin to the surface, we can determine $\phi_{\rm in}(r,\phi)$ as

$$\phi_{\rm in} = \left(\frac{\Omega B_{\rm NS}}{2c}\right) r^2\sin^2\theta + {\rm const.} = -\left(\frac{\Omega B_{\rm NS} r^2}{3c}\right)[P_2(\cos\theta) - 1] + \phi_{\rm con}, \tag{44}$$

where $P_2(\cos\theta) = 3\cos^2\theta - 1$ is the Legendre polynomial and $\phi_{\rm con}$ is a constant. Because $\mathbf{E}\cdot\mathbf{B} = 0$ inside the star, the magnetic field lines are equi-potentials labeled by the voltage, which in turn is determined by the location at which the particular field line emerges on the star's surface. Outside the star, the electric field is given by $\mathbf{E} = -\nabla\phi_{\rm out}(r,\theta)$, where $\phi_{\rm out}(r,\theta)$ satisfies the Laplace equation $\nabla^2\phi_{\rm out} = 0$. Taking the general solution in the form

$$\phi_{\rm out}(r,\theta) = \sum_{l=1}^{\infty}\frac{a_l}{r^{l+1}}P_l(\cos\theta) \tag{45}$$

and matching the potential at the surface of the star $r = R_{\rm NS}$, we easily see that the exterior solution must be

$$\phi_{\rm out}(r,\theta) = -\frac{\Omega B_{\rm NS}R_{\rm NS}^5}{6cr^3}(3\cos^2\theta - 1) \tag{46}$$

where the constant $\phi_{\rm con}$ in eq.(44) is set to $\phi_{\rm con} = -(\Omega B_{\rm NS}R_{\rm NS}^2/3c)$. The electric field outside the star is given by

$$\mathbf{E}(r,\theta) = -\frac{\Omega B_{\rm NS}R_{\rm NS}^5}{2cr^4}(3\cos^2\theta - 1)\mathbf{e}_r - \frac{\Omega B_{\rm NS}R_{\rm NS}^5}{cr^4}\sin\theta\cos\theta\mathbf{e}_\theta. \tag{47}$$

The magnetic field is that of a dipole,

$$\mathbf{B} = \frac{B_{\rm NS}R_{\rm NS}^3\cos\theta}{r^3}\mathbf{e}_r + \frac{B_{\rm NS}R_{\rm NS}^3\sin\theta}{2r^3}\mathbf{e}_\theta. \tag{48}$$

The solution also ensures that the radial component B_r of the magnetic field and the tangential component E_θ of the electric field are continuous at the surface. The equation for the field lines with a magnetic dipole will be of interest later on. These lines $r(\theta)$ satisfy the equation $(B_r/B_\theta) = (dr/rd\theta) = (2\cos\theta/\sin\theta)$, which can be integrated to give

$$r/\sin^2\theta = \text{const.} \tag{49}$$

It is important to determine the charge and the current distributions that give rise to these fields by the equations $\rho = (\nabla\cdot\mathbf{E}/4\pi)$ and $\mathbf{J} = (c/4\pi)\nabla\times\mathbf{B}$. They are given in the interior as

$$\rho_{\text{in}} = \left(\frac{\nabla\cdot\mathbf{E}}{4\pi}\right) = -\left(\frac{\Omega B_{\text{NS}}}{2\pi c}\right),\ \mathbf{J}_{\text{in}} = 0 \text{ (interior)}. \tag{50}$$

Outside the star, both charge and current vanish:

$$\rho_{\text{out}} = \left(\frac{\nabla\cdot\mathbf{E}}{4\pi}\right) = 0,\ \mathbf{J}_{\text{out}} = 0 \text{ (exterior)}. \tag{51}$$

In order to determine the charge and the current on the stellar surface, the discontinuities in the electric and the magnetic fields have to be calculated. The charge density at the surface is given by $\rho_{\text{sur}} = [E_r]/4\pi$, where $[E_r]$ denotes the discontinuity in the radial component of the electric field across the surface. Using this relation, the surface density is described as

$$\rho_{\text{sur}} = \frac{1}{4\pi}(-\phi^{\text{out}}_{,r} + \phi^{\text{in}}_{,r}) = \frac{\Omega B_{\text{NS}} R_{\text{NS}}}{12\pi c}[2 - 5P_2(\cos\theta)]. \tag{52}$$

Similarly, the surface current is given by

$$\mathbf{J}_{\text{sur}} = \frac{c}{4\pi}(\mathbf{B}^{\text{out}} - \mathbf{B}^{\text{in}}) = \frac{3cB_{\text{NS}}}{8\pi}\sin\theta\mathbf{e}_\theta. \tag{53}$$

Next, we will show that, for realistic values of a neutron star, the region outside the star is unlikely to be a vacuum in contrast to the assumption used in the above discussion. Using the scaling obtained above, the voltage and the electric field near the star's surface are

$$\phi_{\text{sur}} \sim \frac{\Omega B_{\text{NS}} R_{\text{NS}}^2}{2c} \sim 3\times10^{17}\text{V}\left(\frac{P}{0.1\text{s}}\right)^{-1}\left(\frac{B_{\text{NS}}}{10^{12}\text{G}}\right)\left(\frac{R_{\text{NS}}}{10^6\text{cm}}\right)^2, \tag{54}$$

and

$$E \sim \frac{\Omega R_{\text{NS}}}{c}B_{\text{NS}} \sim 2\times10^9\text{esu}\left(\frac{P}{0.1\text{s}}\right)^{-1}\left(\frac{B_{\text{NS}}}{10^{12}\text{G}}\right)\left(\frac{R_{\text{NS}}}{10^6\text{cm}}\right). \tag{55}$$

The electric force on a charged particle is very much stronger than the gravitational force (by a factor of 10^{13} for an electron), and hence charged particles can be pulled out from the neutron star surface to create a magnetosphere around the star. Whether this actually occurs or not depends on the details of solid-state physics near the surface of the neutron star. There are binding forces on charged particles in the surface due to the lattice structure in a strong magnetic field, such that particles are free only if the surface layers are above the thermal emission temperature. For electrons, this temperature is [160]

$$T_e \sim 3.6\times10^5\text{K}\left(\frac{Z}{26}\right)^{0.8}\left(\frac{B_{\text{NS}}}{10^{12}\text{G}}\right)^{0.4}, \tag{56}$$

and that for ions is

$$T_i \sim 3.5 \times 10^5 \mathrm{K} \left(\frac{B_{\mathrm{NS}}}{10^{12}\mathrm{G}}\right)^{0.73}, \tag{57}$$

where Z is the atomic number of matter in the surface layer. If surface temperature is satisfied with $T_s > T_{i,e}$, charged particles are boiled of the surface layers. Measured surface temperatures of pulsars are typically $T_s > 0.5\text{-}3.0 \times 10^6$ K, above T_e and T_i. Even if $T_s < T_{\mathrm{i,e}}$, charged particles can be generated by the cosmic γ-ray background radiation due to magnetic pair-creation process. A comprehensive analysis [139] showed that the cosmic γ-ray background leads to the generation of 10^5 primary particles per second. This is quite enough for the neutron star magnetosphere to be efficiently filled with electron-positron plasmas. Therefore, assuming for a moment that ejection of charged particles does happen, we review the question how the structure of the magnetosphere is changed because of the particle ejection.

The charged particle pulled out from the surface will spiral along the magnetic field lines and will drift perpendicular to them. The rapid spiral motion will cause the radiative loss of the transverse motion so that the residual motion will be along the magnetic field line. It should also be noted that the particles moving along the magnetic field lines will be accelerated by the electric field component $E_{\parallel} = (\mathbf{E}\cdot\mathbf{B}/|\mathbf{B}|)$ in the direction of the magnetic field. Near the surface, $E_{\parallel}$ is

$$E_{\parallel} = \frac{\mathbf{E}\cdot\mathbf{B}}{|\mathbf{B}|} = -\frac{\Omega R_{\mathrm{NS}}}{c} B_{\mathrm{NS}} \cos^3\theta. \tag{58}$$

The global motion of the charged particle will depend on whether the magnetic field line attached to it is closed or open. The open field means the line reaching the light cylinder $R_{\mathrm{LC}} \equiv c/\Omega$, and the plasma attached can not be strictly corotating with the neutron star outside R_{LC}. A line starting within an angular region $\theta < \theta_{\mathrm{pc}}$ near the polar cap will cross the light cylinder whereas that for $\theta > \theta_{\mathrm{pc}}$ will loop back before reaching the light cylinder. The last open field line, starting at $r = R_{\mathrm{NS}}$, $\theta = \theta_{\mathrm{pc}}$ and separating open zone and closed zone, should have $r = R_{\mathrm{LC}}$ at $\theta = \pi/2$. Dipole field line given by eq.(49) implies $\sin\theta_{\mathrm{pc}} = (R_{\mathrm{NS}}/R_{\mathrm{LC}})^{1/2}$. The corresponding radius R_{pc} of the polar cap region is given by

$$R_{\mathrm{pc}} \sim R_{\mathrm{NS}} \sin\theta_{\mathrm{pc}} = R_{\mathrm{NS}} \left(\frac{R_{\mathrm{NS}}}{R_{\mathrm{LC}}}\right)^{1/2} = 1.4 \times 10^4 \mathrm{cm} \left(\frac{R_{\mathrm{NS}}}{10^6 \mathrm{cm}}\right)^{3/2} \left(\frac{P}{1\mathrm{s}}\right)^{-1/2}. \tag{59}$$

Charged particles pulled out from the polar cap region can generally redistribute themselves around the star, forming a corotating magnetosphere. If the inertia of the particles is neglected, they will rearrange themselves for no net electromagnetic force to act on them; that is, $\mathbf{E} + (\mathbf{v}/c) \times \mathbf{B} = 0$, where $\mathbf{v} = \boldsymbol{\Omega} \times \mathbf{r}$. From the resulting electric field $\mathbf{E}$, the charge density ρ is determined by the relation $\nabla \cdot \mathbf{E} = (4\pi\rho)$. That is

$$4\pi c\rho = \nabla \cdot [\mathbf{B} \times (\boldsymbol{\Omega} \times \mathbf{r})] = -\frac{2\boldsymbol{\Omega}\cdot\mathbf{B}}{1 - \frac{r^2 \sin^2\theta}{R_{\mathrm{LC}}^2}}, \tag{60}$$

showing that the region with $\boldsymbol{\Omega}\cdot\mathbf{B} = \Omega B_z > 0$ will have negative ρ and that with $\Omega B_z < 0$ will have positive ρ. This charge density is called Goldreich-Julian charge density, ρ_{GJ} [50].

The number density of charges near the surface is approximately given by

$$\frac{\rho_{\rm GJ}}{e} \sim 10^{11}{\rm cm}^{-3}\left(\frac{B_z}{10^{12}{\rm G}}\right)\left(\frac{P}{1{\rm s}}\right)^{-1}. \tag{61}$$

Charged particles from the polar cap region will move along the magnetic field lines towards the light cylinder $R_{\rm LC}$, where the relativistic effects will lead to a breakdown of the approximation that the inertia of the particles is neglected. At the same time, the plasma cannot corotate with the star there. This is also obvious from the fact that a corotating plasma near the light cylinder will acquire speeds close to the speed of light. The structure of field lines as well as the charge density in the magnetosphere are drastically modified near $R_{\rm LC}$. The field lines are expected to be swept back near the light cylinder and are called open field lines. The plasma will flow away from the pulsar along the open field lines, which arise from a region near the polar cap in the above-simplified analysis. The potential difference $\Delta\phi$ between the center and the edge of the polar cap can be estimated from a dipole solution. If we have for $\theta_{\rm pc} \ll 1$

$$\Delta\phi = \frac{\Omega B_{\rm NS}R_{\rm NS}^2}{2c}\cdot\frac{R_{\rm NS}}{R_{\rm LC}} = 6\times10^{12}{\rm V}\left(\frac{B_{\rm NS}}{10^{12}{\rm G}}\right)\left(\frac{P}{1{\rm s}}\right)^{-2}. \tag{62}$$

This is the same order as the potential difference along the magnetic field lines over a distance $\sim R_{\rm NS}$, $\Delta\phi \sim (\mathbf{E}\cdot\mathbf{B}/B)R_{\rm NS}$. Charged particles, flowing along open field lines, will be accelerated by a voltage of this order elsewhere. This corresponds to energy of $6\times10^{12}{\rm eV}(B_{\rm NS}/10^{12}{\rm G})(P/1{\rm s})^{-2}$ and can make electrons highly relativistic with a Lorentz factor of $\gamma \sim 10^7(B_{\rm NS}/10^{12}{\rm G})(P/1{\rm s})^{-2}$, where P is measured in seconds.

Finally in this subsection, we compare the spin-down luminosity for the case of vacuum and of surrounding plasma. In general, a model of forming magnetosphere will have a poloidal current system. The currents leave and return to the star within two polar caps. The total torque $L_{\rm tor}$ exerted on the star is given by

$$L_{\rm tor} = 2\int_0^{\theta_{\rm pc}} \frac{rB_\phi}{4\pi}B_r 2\pi R_{\rm NS}^2 \sin^2\theta d\theta. \tag{63}$$

For illustration, we write the net total current from the star between the pole and the angle θ as $I(\theta) = K\theta(\theta_{\rm pc}-\theta)$, where K and also $I(\theta)$ are negative in sign. The value of $I(\theta)$ with the maximum modulus is $I_m = K\theta_{\rm pc}^2/4$, reached at $\theta = \theta_{\rm pc}/2$. By Ampére's law, the associated B_ϕ at θ is given by

$$(2\pi r\sin\theta)B_\phi = 4\pi I(\theta)/c. \tag{64}$$

Over the small angle polar caps, $B_r \sim B_{\rm NS}$, and the torque $L_{\rm tor}$ becomes

$$L_{\rm tor} \sim \frac{2B_{\rm NS}R_{\rm NS}^2}{c}\int_0^{\theta_{\rm pc}} K\theta(\theta_{\rm pc}-\theta)\theta d\theta = \frac{KB_{\rm NS}R_{\rm NS}^2}{6c}\theta_{\rm pc}^4 = \frac{2I_mF_{\rm pc}}{3\pi c}, \tag{65}$$

where $F_{\rm pc} \sim (\pi R_{\rm NS}^2\theta_{\rm pc}^2)B_{\rm NS}$ is the poloidal flux over the northern cap. The associated energy loss rate $L_{\rm sd}$ is $\Omega|L_{\rm tor}|$. The rotating magnetospheric charges will modify the poloidal field, but as first approximation it may be taken as still roughly like a vacuum dipolar field out to

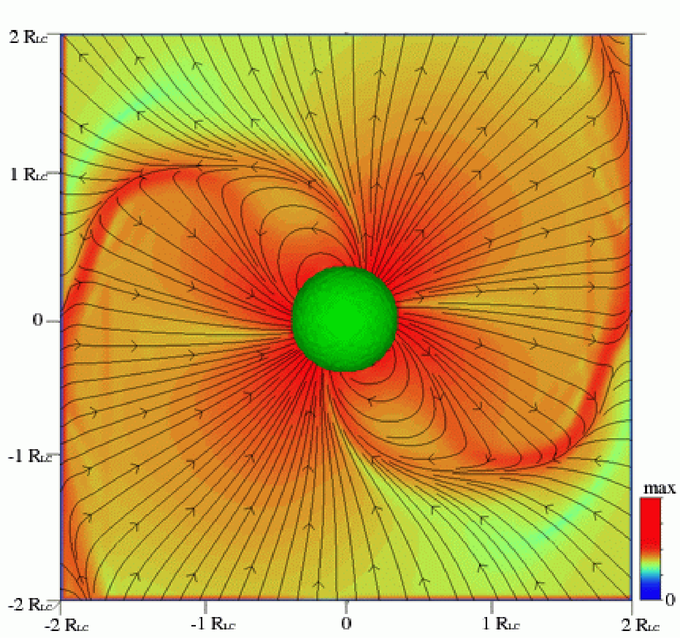

Figure 15: Oblique pulsar magnetosphere with magnetic inclination $\alpha = 60°$ in the corotating frame. Magnetic field lines in the $\mu - \Omega$ plane. Color represents absolute value of the total current $|\nabla \times \mathbf{B}|$. Figure adopted from Spitkovsky (2006) [142].

the light cylinder. Assuming also that $\theta_{\rm pc}$ is given by the last open field line to reach the light cylinder, we have $\sin^2\theta_{\rm pc}/R_{\rm NS} = \Omega/c$, or $\theta_{\rm pc} = (\Omega R_{\rm NS}/c)^{1/2}$, with poloidal component B_p at the light cylinder typically $(B_{\rm NS}/2)(\Omega R_{\rm NS}/c)^3$. In stellar wind theory [170], $|B_\phi| \sim B_p$ at the Alfvénic surface, where poloidal component of particle velocity equals to the Alfvénic one. From eq.(64), if a similar relation holds at the light cylinder, $|I(\pi/2)| \sim cB_{\rm NS}(\Omega/c)^2 R_{\rm NS}^3/4$, yielding the energy loss associated with the torque eq.(65)

$$L_{\rm sd} \sim \frac{8\pi^4 B_{\rm NS}^2 R_{\rm NS}^6}{3c^3 P^4}. \tag{66}$$

This is the same order as that of vacuum dipole model, eq.(31).

3.2.2 Force-free approximation

As a global pulsar magnetosphere in last subsection, the electric field component parallel to the magnetic field would pull charged particles out of the pulsar, opening up magnetic field lines that cross the light cylinder, thus producing an MHD wind beyond it. Following the work of Goldreich and Julian (1969) [50], a number of attempts were performed to construct more realistic pulsar magnetosphere [100, 132, 103, 114, 102, 37, 113, 57, 157, 80, 99]. For the force-free approximation they used, two necessary consitions are that

- the plasma energy density is much smaller than that of the electromagnetic field.
- the amount of plasma is enough to screen the accelerating electric field $E_\parallel$.

The force-free approximation implies that in the energy momentum conservation law $\nabla_\alpha T^{\alpha\beta}$ $= 0$ we can disregard the particle contribution, where $\alpha, \beta = 0, 1, 2, 3$. Using the explicit form of the energy-momentum tensor of the electromagnetic field

$$T^{\alpha\beta}_{\rm em} = \begin{pmatrix} \frac{(E^2+B^2)}{8\pi} & \frac{c}{4\pi}\mathbf{E}\times\mathbf{B} \\ \frac{c}{4\pi}\mathbf{E}\times\mathbf{B} & -\frac{1}{4\pi}(E^iE^k + B^iB^k) + \frac{1}{8\pi}(E^2+B^2)\delta^{ik} \end{pmatrix}, \tag{67}$$

we obtain for the space components the known equation

$$\frac{1}{c}\mathbf{J}\times\mathbf{B} + \rho\mathbf{E} = 0, \tag{68}$$

or

$$(\nabla\times\mathbf{B})\times\mathbf{B} + (\nabla\cdot\mathbf{E})\mathbf{E} = 0. \tag{69}$$

Recently, the non-axisymmetric, oblique rotating magnetosphere was for the first time presented by Spitkovsky (2006) [142], who used a time-dependent numerical code to advance the electromagnetic field under the force-free approximation to steady state. He numerically solved the time dependent Maxwell equations

$$\frac{\partial\mathbf{B}}{\partial t} = -c\nabla\times\mathbf{E} \tag{70}$$

$$\frac{\partial\mathbf{E}}{\partial t} = c\nabla\times\mathbf{B} - 4\pi\mathbf{J} \tag{71}$$

under ideal magnetohydro dynamics condition

$$\mathbf{E}\cdot\mathbf{B} = 0 \tag{72}$$

and force-free condition, eq.(68). The time-evolution of these equations requires an expression for the current density $\mathbf{J}$ as a function of $\mathbf{E}$ and $\mathbf{B}$,

$$\mathbf{J} = \frac{c}{4\pi}\nabla\cdot\mathbf{E}\frac{\mathbf{E}\times\mathbf{B}}{B^2} + \frac{c}{4\pi}\frac{(\mathbf{B}\cdot\nabla\times\mathbf{B} - \mathbf{E}\cdot\nabla\times\mathbf{E})\mathbf{B}}{B^2} \tag{73}$$

[56]. His simulations confirmed the general picture of current closure established by Contopoulos et al. (1999) [37] and produced a structure very similar to that of their solution [37] in the axisymmetric case. Similar simulations were performed by Kalapotharakos & Contopoulos (2009) [74]. In general, the 3D magnetosphere, just like the axisymmetric one, consists of regions of closed and open field lines with a large-scale electric current circuit established along open magnetic field lines. In the 3D case, the current sheet needed for the global current closure is in fact undulating, as foreseen in the kinematic solution of Bogovalov (1999) [27]. In figure 15, an example of the simulations is shown.

The force-free approximation may be valid within the light cylinder. However, when charged particles approach to the light cylinder, then Lorentz factors are significantly increasing and the particle energy is no longer neglected compared with the electromagnetic energy. Under the ideal magnetohydrodynamical condition, there is no particle acceleration region. Therefore it is necessary to improve this point in more realistic models. Very recently, Li et al. (2011) [89] and Kalapotherakos et al. (2011) [75] calculate the force-free pulsar magnetospheres under the non-ideal magnetohydrodynamical condition. However, their approach to modeling resistive pulsar magnetospheres is too simple. They use a form of Ohm's law in which they neglect several terms such as inertial effects, pressure, the Hall effect and spatial dependence of conductivity.

Thus, there are some significant problems in force-free model. However, the solutions of the non-axisymmetric, oblique rotating magnetosphere have a significant advantage. All observed pulsars show "pulse". This means that all pulsars are essentially the non-axisymmetric system. Therefore, it is useful to compare non-axisymmetric force-free solutions with observational results as the starting point for detailed studies of pulsar magnetospheres under more general conditions.

Note that simulations including particle inertia and/or non-ideal MHD effects such as particle (e.g, [83, 140, 117, 141, 163, 164]) and two-fluid simulations [79] have already been done. However, these calculations are only axisymmetric case, so that direct comparisons with the observation are difficult.

3.3 Particle Acceleration and Emission Models

Under the force-free approximation, there is no particle acceleration region in the pulsar magnetosphere. High-energy emission, however, suggests violation of force-free approximation elsewhere. High-energy pulsed emissions have been possibly considered in the polar cap [39], slot gap [111] and outer gap [30] models. In this subsection, we will review these three models; especially we focus on their differences such as the location, spectrum shape and multi-wavelength properties. Then, we compare these models with *Fermi* observational results.

3.3.1 Polar cap model

Based on the Goldreich-Julian model [50], two distinct zones are formed in the pulsar magnetosphere. The separating line is called the last-open field line. Particles located in closed zone are always captured and corotate with the central star, whereas those in open zone are ejected to infinity. Consequently, the plasma must be continuously generated from the magnetic pole region of the star.

It is necessary to take into account the secondary plasma generation in the magnetic pole region [146] and detailed model of the process was studied by Ruderman and Sutherland (1975) [129]. The model is so-called polar cap model. It is based on the magnetic pair creation process in the strong magnetic field. The longitudinal electric field is generated by a continuous escape of particles along the open field lines beyond the magnetosphere. As a result, the longitudinal electric field region forms in the vicinity of the magnetic poles, and the height is determined by the secondary plasma generation condition. The chain of processes is summalized as

1. the primary particle acceleration by the longitudinal electric field induced by the difference between the charge density ρ and the Goldreich-Julian (GJ) charge density $\rho_{\rm GJ}$.
2. the emission of curvature photons with characteristic frequency $\omega < \omega_{\rm cur}$.

3. the photon propagation in the curved magnetic field up to the secondary electron-positron pair generation.

4. the secondary particle acceleration, the emission of curvature photons, which, in turn, give rise to the new generation of secondary particles.

It is important that a greater part of secondary particles is generated over the acceleration region, where the longitudinal electric field is rather small, so that the secondary plasma can escape from the neutron star magnetosphere.

In order to estimate the longitudinal electric field we consider, for simplicity, one-dimensional equation

$$\frac{dE_{\parallel}}{dh} = 4\pi(\rho - \rho_{\rm GJ}) \tag{74}$$

which can be used if the gap height H is smaller than the polar cap radius $R_{\rm pc}$. The polar cap model strongly depends on the boundary condition at the stellar surface. As mentioned before, observed surface temperatures of pulsars are typically $T_s > T_e$, T_i. Therefore, particles can freely escape from the neutron star surface. In this condition, it is logical to take here

$$E_{\parallel}(h = 0) = 0, \tag{75}$$

and the charge density ρ is close to $\rho_{\rm GJ}$. The longitudinal electric field must also be zero on the upper boundary of the acceleration region

$$E_{\parallel}(h = H) = 0. \tag{76}$$

Otherwise, the secondary particles with one of the signs would fail to escape to infinity. The longitudinal electric field is specified only by a difference between the ρ and $\rho_{\rm GJ}$, which can be written near the surface as

$$\rho_{\rm GJ} = -\frac{\mathbf{\Omega} \cdot \mathbf{B}}{2\pi c}. \tag{77}$$

On the other hand, for the relativistic plasma moving with velocity $v \sim c$, we have

$$\rho = C(\Psi)B, \tag{78}$$

where $C(\Psi)$ is constant along the magnetic field lines. As we see, the charge densities, eqs.(77) and (78) change differently along the magnetic field line. Thus, the GJ charge density, besides the factor B, also contains the geometric factor. As a result, the charge-separated relativistic plasma in its motion fails to satisfy the condition $\rho = \rho_{\rm GJ}$, which gives rise to the particle acceleration in the longitudinal electric field, which leads to hard photon emission, and, hence, to secondary electron-positron plasma generation. Therefore, beyond the acceleration region, the field must be always close to zero.

Note that the boundary conditions, eqs.(75) and (76) can be satisfied simultaneously only if the electric charge density on the acceleration region boundaries does not coincide with the GJ density, i.e., when the derivative $dE_{\parallel}/dh \neq 0$ here. As a result, eq.(74) can be rewritten as

$$\frac{dE_{\parallel}}{dh} = A_{\rm a}\left(h - \frac{H}{2}\right), \tag{79}$$

where

$$A_{\rm a} = 4\pi \frac{d(\rho - \rho_{\rm GJ})}{dh}\bigg|_{h=H/2}. \tag{80}$$

Finally, we have for inclination angle $\alpha > \epsilon_{\rm A}$

$$A_{\rm a} = \frac{3}{2}\frac{\Omega B_{\rm NS}}{cR_{\rm NS}}\theta_{\rm m}\cos\phi_{\rm m}\sin\alpha. \tag{81}$$

Here $\theta_{\rm m} \sim \epsilon_{\rm A}$ is the polar angle, $\phi_{\rm m}$ is an azimuthal angle relative to the magnetic dipole axis, and $\epsilon_{\rm A} = (R_{\rm NS}/R_{\rm LC})^{1/2}$ is the small geometrical parameter. Solution of eq.(79) is approximated as

$$E_{\parallel} = -E_{\rm A}\frac{h(H-h)}{H^2}, \tag{82}$$

where

$$E_{\rm A} \sim \frac{3\pi}{2}|\rho_{\rm GJ}|\frac{H^2}{R_{\rm NS}}\theta_{\rm m}\cos\phi_{\rm m}\tan\alpha. \tag{83}$$

A particle backflow is needed for this solution to exist. Critical value can be determined from eq.(74),

$$\frac{J_{\rm back}}{J_{\rm GJ}} \sim \epsilon_{\rm A}\frac{H}{R_{\rm NS}} \sim 10^{-4}. \tag{84}$$

Arons and his co-workers studied this model [46, 133, 15].

Daugherty and Harding (1994, 1996) [38, 39] use a Monte Carlo simulation of a polar cap model of γ-ray pulsars to estimate light curves and phase-resolved spectra. Their proposed polar cap model is based on the following assumptions:

1. The γ-ray emission is initiated by the acceleration of electrons from the neutron star surface, just above the magnetic polar cap regions that enclose the open magnetic field lines extending to the light cylinder.

2. The emission originates from curvature radiation produced by the electrons as they follow the open magnetic field lines.

3. The processes of magnetic pair creation by neutron star magnetic field and synchrotron radiation by the emitted pairs produce photon-pair cascades, from which the observed γ-ray emission emerges.

4. The model requires that $\alpha \sim \theta_{\rm b}$, where $\theta_{\rm b}$ is the half-angle of the γ-ray beam emerging from the polar cap.

5. The acceleration of the electrons occurs over an extended distance above the polar cap surface, so that they reach their peak energies at heights of a few neutron star radii. Above these heights, overlying force-free plasma cuts off the acceleration.

In their simulation, they calculate energy balance equation

$$\frac{d\gamma}{dh} = (\beta c)^{-1}\left[\left(\frac{d\gamma}{dt}\right)_{\rm acc} - \left(\frac{d\gamma}{dt}\right)_{\rm cr} - \left(\frac{d\gamma}{dt}\right)_{\rm cs}\right], \tag{85}$$

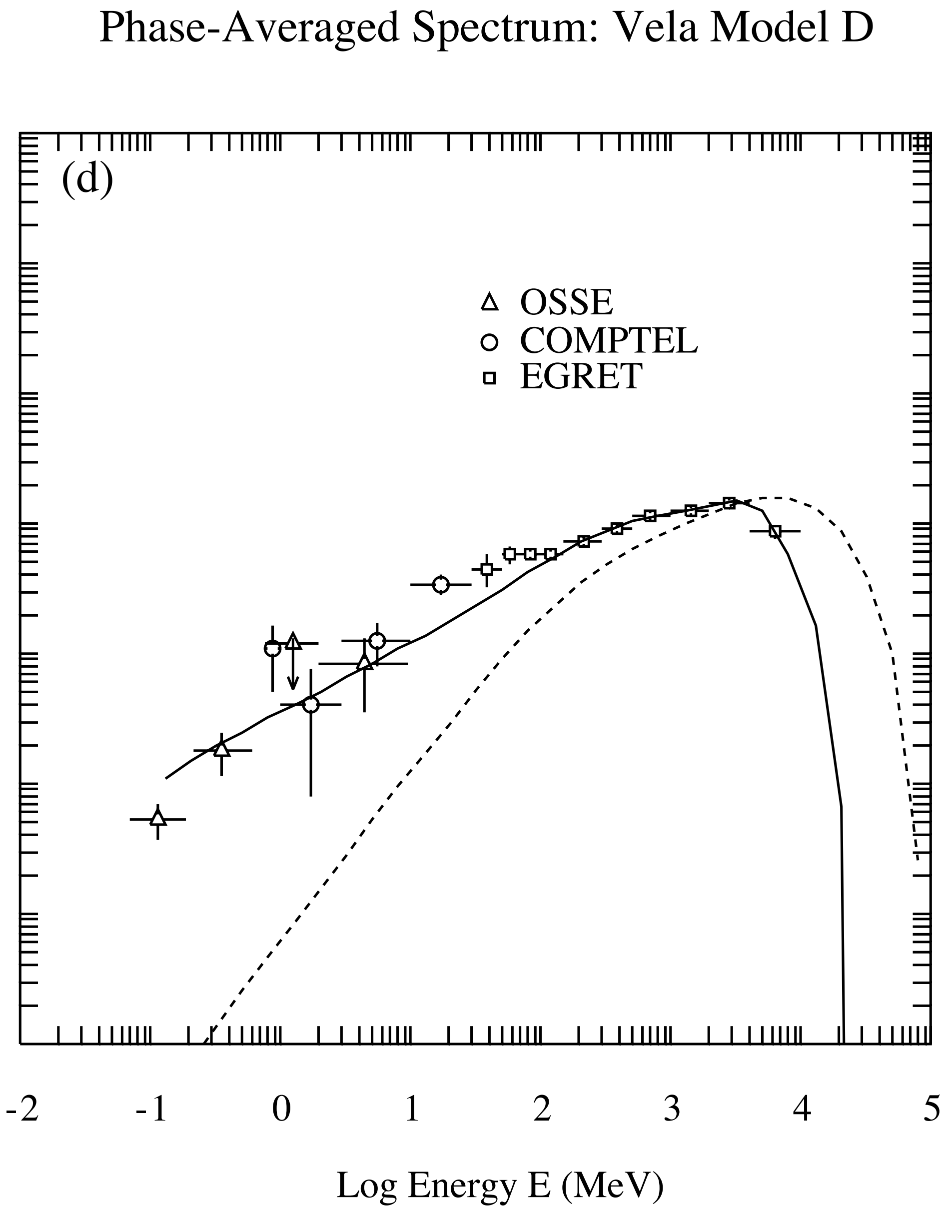

Figure 16: Phase-avelaged photon spectrum for Vela pulsar. Solid lines show full cascade γ-ray emission, while dashed lines show initial curvature radiation. Also shown are observations by EGRET, as well as COMPTEL and OSSE. Figure adopted from Daugherty and Harding (1996) [39].

for each particle. Here h is the distance traversed along the field lines. The subscript acc denotes the energy gain due to electrostatic acceleration. They assume that this gain is proportional to $E_{\|}$. Unfortunately, current models of pulsar magnetopheres do not agree with the behavior of $E_{\|}$ near the polar cap surface. They use the following equation

$$\begin{aligned} E_{\|}(h) &= \frac{m_{\mathrm{e}}c^2}{e}\left(\frac{d\gamma}{dh}\right)_{\mathrm{acc}} \\ &= \frac{m_{\mathrm{e}}c^2}{e}\left[a_0 + a_1\left(\frac{h-h_0}{R_{\mathrm{NS}}}\right)\right]\Theta\left(\frac{h-h_0}{R_{\mathrm{NS}}}\right)\Theta\left(\frac{H-h}{R_{\mathrm{NS}}}\right), \end{aligned} \tag{86}$$

where $\Theta(x)$ is the unit step function (0 for $x < 0$, 1 for $x > 0$), and the constants a_0, a_1 and h_0 are taken as free parameters. If we let set $a_0 = 0$, we have crude approximation of eq.(79). Remaining two energy loss terms are

$$\left(\frac{d\gamma}{dt}\right)_{\mathrm{cr}} = \frac{2}{3}\frac{e^2}{m_{\mathrm{e}}c}\frac{\gamma^4}{R_{\mathrm{cur}}^2}, \tag{87}$$

for curvature radiation energy loss and

$$\left(\frac{d\gamma}{dt}\right)_{\mathrm{cs}} = c\int d\varepsilon \int d\Omega_{\mathrm{p}} n_{\mathrm{ph}}(\varepsilon, \Omega_{\mathrm{s}})(1-\beta\cos\Psi_{\mathrm{b}})\int d\varepsilon'_{\mathrm{s}}\int d\Omega'_{\mathrm{s}}\frac{d\sigma'}{d\varepsilon'_{\mathrm{s}}d\Omega'_{\mathrm{s}}}(\varepsilon_{\mathrm{s}}-\varepsilon), \tag{88}$$

for Compton scattering loss rate [41, 145], where $\varepsilon = \hbar\omega/m_{\mathrm{e}}c^2$ is the incident photon energy in units of the electron rest mass energy, $n_{\mathrm{ph}}(\varepsilon, \Omega_{\mathrm{p}})$ is the number density of incident background photons within energy and solid angle increments $d\varepsilon$ and $d\Omega_{\mathrm{p}}$, and Ψ_{b} denotes the angle between these photons and the local electron beam directions. The quantity $d\sigma'/d\varepsilon'_{\mathrm{s}}d\Omega'_{\mathrm{s}}$ is the magnetic Compton scattering cross section in the local electron rest frame, where the prime denotes quantity evaluated in the frame and the subscript s labels scattered photon quantity.

Using eq.(85), Daugherty and Harding (1996) [39] track primary particles injected in neutron star surface, emitted γ-ray photon, and created secondary particles. Examples of their calculated results for Vela pulsar are shown in figure 16. The γ-ray spectrum is in overall agreement with observations. The most important feature predicted in the spectrum is a very sharp cutoff, because we observe partially attenuated γ-ray due to strong magnetic field.

Daugherty and Harding (1996) [39] discuss the multi-wavelength light curve based on the polar cap model. However, they did not discuss the origin of the non-thermal emission mechanism, but the phases of the peaks. So far, only γ-ray and radio light curves were calculated in the polar cap model as far as we know.

3.3.2 Slot gap model

Secondly, we introduce the slot gap model, which was discovered by studies of the geometry of the polar cap accelerators [15, 14]. Due to the geometry of the field lines and the assumed boundary conditions of the accelerator, the altitude of the pair formation front (PFF) varies with magnetic colatitude across the polar cap [14, 59]. On field lines well inside the polar

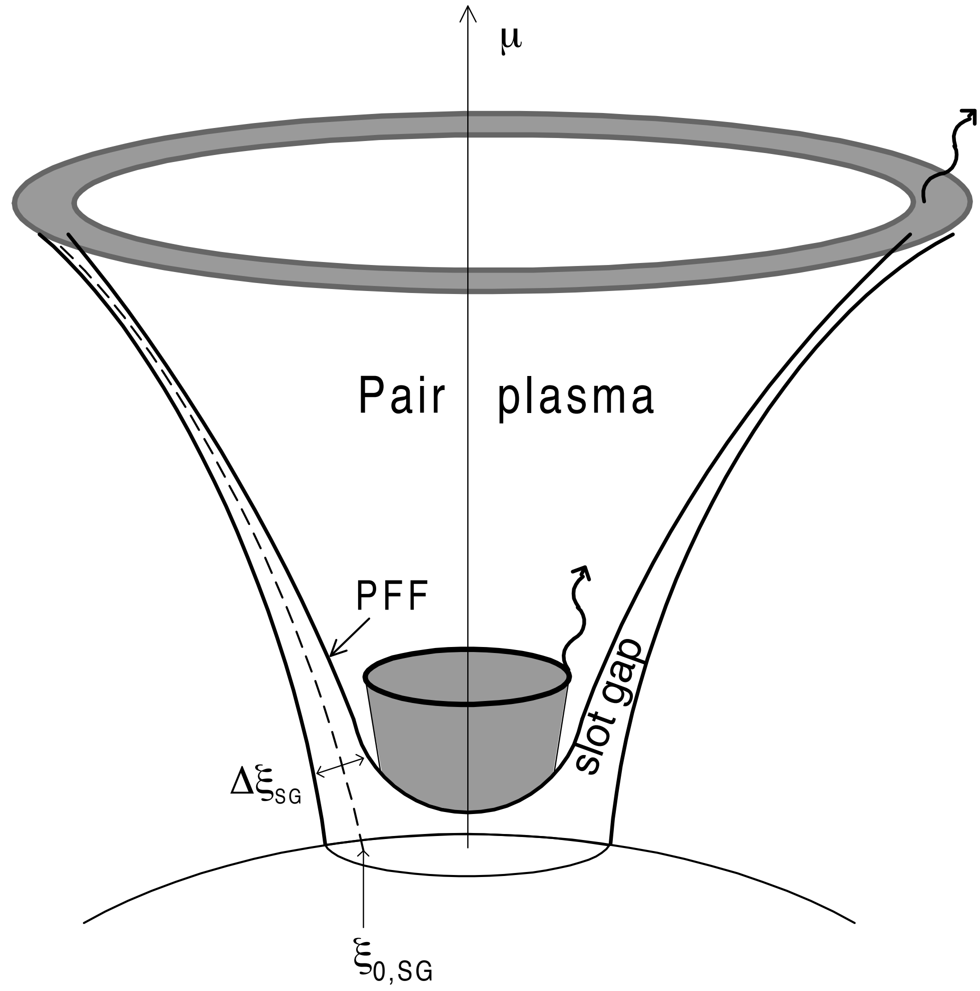

Figure 17: Schematic illustration of polar cap geometry, showing the outer boundary of the open field line region (where $E_{\parallel} = 0$) and the curved shape of the pair formation front (PFF) which asymptotically approaches the boundary at high altitude. The slot gap exists between the pair plasma that results from the pair cascades above the PFF and the outer boundary. A narrow beam of high-energy emission originates from the low-altitude cascade on the field lines interior to the slot gap. $\Delta r_{\mathrm{ov,SG}}$ (denote $\Delta\xi_{\mathrm{SG}}$ in this figure) is the slot gap thickness and $r_{\mathrm{ov,SG}}$ (denote $\xi_{0,\mathrm{SG}}$ in this figure) is the colatitude at the center of the slot gap. Figure adopted from Muslimov & Harding (2003) [110].

cap rim, $E_\parallel$ is relatively strong and PFF is located near the surface. But at the polar cap rim, which is assumed to be a perfectly conducting boundary, $E_\parallel$ vanishes. Near this boundary, the electric field is decreasing and a larger distance is required for the electrons to be accelerated to the Lorentz factor needed to energetic photons for pair production. PFF thus curves upwardly to the boundary and a narrow slot gap is formed near the last-open field line [14] (see figure 17). Since $E_\parallel$ is unscreened in the slot gap, particles are continuously accelerated and radiate photons to high altitude along the last open field lines. The width of the slot gap is a function of $\Lambda_{\rm SG} \equiv P_1 B_{\rm NS,12}^{-4/7}$ of pulsar period and surface magnetic field [110], where $P_1 = P/1{\rm s}$ and $B_{\rm NS,12} = B_{\rm NS}/10^{12}{\rm G}$, and can be expressed in magnetic colatitude as a fraction of the polar cap half-angle $\Delta r_{\rm ov,SG}$, where $r_{\rm ov} \equiv \theta_{\rm m}/\theta_{\rm pc}$

$$\Delta r_{\rm ov,SG} \sim \begin{cases} 4\Lambda_{\rm SG}, & \Lambda_{\rm SG} < 0.075 \\ 0.3, & \Lambda_{\rm SG} > 0.075. \end{cases} \tag{89}$$

The particles can achieve very high Lorentz factors ($\gamma \sim 3 - 4 \times 10^7$ at altitudes of several stellar radii) which are limited by curvature radiation loss [111]. Since the slot gap is very narrow for young pulsars having short periods and high fields, the corresponding solid angle of the gap emission $\Omega_{\rm p,SG} \propto \theta_{\rm pc}^2 r \Delta r_{\rm ov,SG}$ is quite small. Even though only a small fraction of the polar cap flux is accelerated in the slot gap, the radiated flux $F_{\rm SG} = L_{\rm SG}/\Omega_{\rm p,SG} d^2$ can be substantial. The total luminosity divided by solid angle from each pole is (from Muslimov & Harding 2003 [110])

$$\begin{aligned} \frac{L_{\rm SG}}{\Omega_{\rm p,SG}} = & \;\epsilon_\gamma \quad [0.123\cos^2\alpha + 0.51\theta_{\rm pc}^2 \sin^2\alpha]{\rm erg\ s^{-1} sr^{-1}} \\ & \times \begin{cases} 9\times 10^{34} L_{\rm sd,35}^{3/7} P_{0.1}^{5/7}, & B < 0.1 B_{\rm c} \\ 2\times 10^{34} L_{\rm sd,35}^{4/7} P_{0.1}^{9/7}, & B > 0.1 B_{\rm c} \end{cases} \end{aligned} \tag{90}$$

where $P_{0.1} \equiv P/0.1{\rm s}$, $L_{\rm sd,35} \equiv L_{\rm sd}/10^{35}{\rm erg\ s^{-1}}$ and ϵ_γ is the conversion efficiency of primary particle energy to high energy emission.

Harding et al. (2008; hereafter HSDF08) [60] proposed a 3D slot gap model of optical-to-γ-ray emission from the slot gap accelerator. Here, we review how their model characterizes the observational properties.

Muslimov & Harding (2003, 2004) [110, 111] presented the solutions for the electric fields in the low-altitude or the high-altitude limits of the slot gap. Both solutions assume a space-charge-limited-flow of electrons from the surface. The space-charge density at the surface with relativistic frame dragging effect, from eq.(4) of Muslimov & Harding (2003) [110] is

$$\rho_0 = \frac{-\Omega B_{\rm NS}}{2\pi c \alpha_0}\left[(1-\kappa)\cos\alpha + \frac{3}{2}\theta_0 H(1)\sin\alpha\cos\phi_{\rm m}\right], \tag{91}$$

where $\phi_{\rm m}$ is the magnetic azimuthal angle and $\theta_0 \sim [\Omega R_{\rm NS}/cf(1)]^{1/2}$ is the polar cap half-angle. Here, $\kappa = (r_{\rm g}/R_{\rm NS})(I/I_0 \sim 0.15 I_{45}/R_{\rm NS,6}^3)$ is the general relativistic parameter for the frame-dragging effect, $r_{\rm g}$ is the neutron star gravitational radius, $R_{\rm NS,6} \equiv R_{\rm NS}/10^6$ cm, and $\alpha_0 = (1 - r_{\rm g}/R_{\rm NS})^{1/2}$. In addition, $f(1) \sim 1.4$ and $H(1) \sim 0.8$ are general relativistic correction. Since $\rho(r)$ decreases faster than $\rho_{\rm GJ}(r)$ above the surface, the deficit $(\rho - \rho_{\rm GJ})$ increases with distance, developing a parallel electric field, $\nabla \cdot \mathbf{E}_\parallel = 4\pi(\rho - \rho_{\rm GJ})$. The treatment of the electric field in the slot gap by Muslimov & Harding (2003, 2004) [110, 111] differs from that of Arons & Scharlemann (1979) [15] and Arons (1983) [14] by taking into account the screening of the electric field by pairs on field lines interior to the slot gap. This treatment forms fully conducting boundaries on both the inner and outer edges of the gap, causing a lower electric field. From eq.(58) of Muslimov & Harding (2004) [111], the low-altitude solution for $\mathbf{E}_{\|}$ is

$$\mathbf{E}_{\|,\mathrm{low}} \sim -3\left(\frac{\Omega R_{\mathrm{NS}}}{c}\right)^2 \frac{B_{\mathrm{NS}}}{f(1)}\nu_{\mathrm{SG}}\left[\frac{\kappa}{\eta^4}\cos\alpha + \frac{1}{2}\theta_0 H(1)\delta(\eta)\sin\alpha\cos\phi_{\mathrm{m}}\right], \tag{92}$$

where $\delta(\eta)$ [109] varies between ~ 0.5 and 1, $\eta = r/R_{\mathrm{NS}}$, and $\nu_{\mathrm{SG}} = (1/4)\Delta r_{\mathrm{ov,SG}}^2$ is a parameter related to the slot gap width, $\Delta r_{\mathrm{ov,SG}}$, given by eq.(89). The solution in eq.(92) is valid for the radii $\eta \lesssim \eta_{\mathrm{c}}$, where η_{c} is a parameter determined by matching smoothly to the high-altitude solution. The high-altitude solution for $\mathbf{E}_{\|}$, valid for $\eta \gtrsim \eta_{\mathrm{c}}$, is given by eq.(53) of Muslimov & Harding (2004) [111],

$$\mathbf{E}_{\|,\mathrm{high}} \sim -\frac{3}{8}\left(\frac{\Omega R_{\mathrm{NS}}}{c}\right)^3 \frac{B_{\mathrm{NS}}}{f(1)}\nu_{\mathrm{SG}}\left\{\left[1 + \frac{1}{3}\kappa\left(5 - \frac{8}{\eta_{\mathrm{c}}^3}\right) + 2\frac{\eta}{\eta_{\mathrm{lc}}}\right]\cos\alpha + \frac{3}{2}\theta_0 H(1)\sin\alpha\cos\phi_{\mathrm{m}}\right\}. \tag{93}$$

The frame dragging effect on the accelerating field persists even at larger distances from the surface, since the high altitude space-charge-limited-flow solution depends on surface boundary conditions. HSDF08 [60] combined the low- and high-altitude solutions by the interporation

$$\mathbf{E}_{\|} \sim \mathbf{E}_{\|,\mathrm{low}} \exp[-(\eta - 1)/(\eta_{\mathrm{c}} - 1)] + \mathbf{E}_{\|,\mathrm{high}} \tag{94}$$

and determined η_{c} to give a smooth transition between $\mathbf{E}_{\|,\mathrm{high}}$ and $\mathbf{E}_{\|,\mathrm{low}}$.

An estimate of the full potential drop of the slot gap can be obtained by summing that of the low-altitude potential (eq.(12) of Muslimov & Harding 2003 [110]) from surface up to η_{c} and that of the high-altitude potential (eq.(52) of Muslimov & Harding 2004 [111]) at the η_{lc}:

$$\phi_{\mathrm{tot}}^{\mathrm{SG}} = \phi_{\mathrm{low}}^{\mathrm{SG}}(\eta_{\mathrm{lc}}) + \phi_{\mathrm{high}}^{\mathrm{SG}}(\eta_{\mathrm{lc}}) = \phi_{\mathrm{NS}}\theta_0^2\nu_{\mathrm{SG}}0.5(1+\kappa)\cos\alpha, \tag{95}$$

where $\psi_{\mathrm{NS}} \equiv (\Omega R_{\mathrm{NS}}/c)B_{\mathrm{NS}}R_{\mathrm{NS}}$. For an example of the Crab pulsar, $B_{\mathrm{NS}} = 8 \times 10^{12}$G, $\Omega = 190$ rad s^{-1}, $\nu_{\mathrm{SG}} = \Delta r_{\mathrm{ov,SG}}^2/4 = 4 \times 10^{-4}$, $\kappa = 0.14$, $\eta_{\mathrm{c}} = 1.2$ and $\phi_{\mathrm{tot}}^{\mathrm{SG}} \sim 1.3 \times 10^{13}$eV.

The particle flux from the slot gap is

$$\dot{n} = \frac{\rho}{e}cA_{\mathrm{sur}} \tag{96}$$

where

$$A_{\mathrm{sur}} = \pi R_{\mathrm{NS}}^2\theta_0^2\Delta\xi_{\mathrm{SG}} \tag{97}$$

is the surface area of the slot gap, with $\rho = \rho_0$ for the primary electrons. $\mathcal{M}_{\mathrm{pair}}$ is the pair multiplicity. Again for the case of the Crab, $\dot{n}_{\mathrm{SG}} \sim 7 \times 10^{32}\mathrm{s}^{-1}$.

HSDF08 [60] modeled radiation over the entire spectrum from optical to γ-ray wavelengths. For these emissions, they simulate the radiation from primary electrons accelerating in the gap and secondary ones produced in cascades near the neutron star surface, and also simulate that electrons are flowing on field lines interior to the gap.

Primary electrons accelerating in the gap will produce curvature radiation up to γ-ray energies. The curvature radiation losses will be balanced by the acceleration due to $\mathbf{E}_\parallel$ so that the particles reach steady-state Lorentz factors. The energy spectrum from a single electron with γ is

$$N_{\rm CR}(\epsilon) = \sqrt{3}\frac{e^2}{c}\gamma\kappa\left(\frac{\varepsilon}{\varepsilon_{\rm cur}}\right), \tag{98}$$

where ε is the radiated photon energy in units of $m_{\rm e}c^2$ and

$$\varepsilon_{\rm cur} = \frac{3}{2}\frac{\hbar}{m_{\rm e}cR_{\rm cur}}\gamma^3, \tag{99}$$

and the function $\kappa(x)$ is defined as

$$\kappa(x) \equiv 2x\int_{2x}^{\infty} K_{5/3}(x')dx'. \tag{100}$$

The photon spectrum is approximated by a power law with an exponential cutoff at $\varepsilon_{\rm cur}$,

$$\frac{N_{\rm CR}(\varepsilon)}{d\varepsilon} = \frac{(2\pi)^{1/3}\alpha_f}{(\lambda m_{\rm e}c)^{1/3}}\left(\frac{c}{R_{\rm cur}}\right)^{2/3}\varepsilon^{-2/3}\exp(\varepsilon/\varepsilon_{\rm cur}). \tag{101}$$

Relativistic particles moving parallel to magnetic field lines can gain the perpendicular momentum by absorbing low-energy photons at cyclotron resonance. The resonant absorption of radio emission by relativistic particles in pulsar magnetospheres, followed by spontaneous synchrotron emission, was first proposed by Shklovsky (1970) [138] as a mechanism for generating the optical radiation. The absorption of photons at the cyclotron resonant frequency in the rest frame of the particle results in an increase in the particle pitch angle. The particle then spontaneously emits cyclotron or synchrotron radiation, depending on whether its momentum perpendicular to the magnetic field, in the frame in which the parallel momentum vanishes, is nonrelativistic or relativistic. Blandford & Scharlemann (1976) [26] computed the cross section for the cyclotron resonant absorption and applied it to the Crab pulsar, and found that a reradiated cyclotron radiation flux was too small to explain the optical emission. However, they assumed that the perpendicular momentum remained nonrelativistic, in which case the applicable rate is that of cyclotron emission from the first excited Landau state, which is smaller than that from highly excited states. Lyubarski & Petrova (1998) [92] performed a more detailed analysis of the distribution functions of particles undergoing the synchrotron-resonant absorption of radio photons and found that the particles can increase their pitch angles rapidly enough in the outer magnetosphere to attain relativistic perpendicular momentum. They found that the pitch angle excitation rate due to resonant absorption is much higher than the de-excitation rate due to synchrotron radiation until very large pitch angles. Resulting synchrotron radiation explains the optical and X-ray spectrum of the Crab and other young pulsars [120]. Harding, Usov & Muslimov (2005) [62] showed that cyclotron resonant absorption of radio emission could work very efficiently for millisecond pulsars, especially for those pulsars with unscreened accelerating electric field.

HSDF08 [60] apply the formulation of Harding, Usov & Muslimov (2005) [62] to model the synchrotron radiation components from both primary electrons accelerating in the slot gap and from non-accelerating pairs on field lines just inside the slot gap. In the case of the primary electrons, the calculation closely parallels that of Harding, Usov & Muslimov (2005) [62], who found that accelerating particles undergoing cyclotron resonant absorption would reach a steady state where the synchrotron radiation losses are balanced by the acceleration gain. The resonant absorption condition is

$$B' = \gamma\varepsilon_0(1-\beta\mu), \tag{102}$$

where ε_0 is the energy of the radio photon in the lab frame (in units of $m_{\rm e}c^2$), $\beta = (1 - 1/\gamma^2)^{1/2}$, $B' = B/B_{\rm c}$ is the local magnetic field strength in units of the critical magnetic field, $\mu = \cos\theta$, and θ is the angle in the frame between the photon and the particle momentum directions (to good approximation the direction of particle momentum is the same as the magnetic field direction). If this condition is met, the radio photon energy is at the local cyclotron energy in the particle rest frame. The resonant condition is not satisfied near the neutron star surface, where the magnetic field is too strong, but may be achieved when the particle reaches the lower magnetic fields at high altitudes. When a particle is undergoing absorption initially in low Landau states, the rate of cyclotron emission is much lower than that of absorption. The Landau state and pitch angle of the particle will therefore increase continuously until equilibrium between the gain by resonant absorption and the loss by synchrotron emission. Since this equilibrium is achieved at high Landau states, the emission is synchrotron rather than cyclotron.

Lyubarski & Petrova (1998) [92] identified two regimes of resonant absorption as the pitch angle of a particle increases. When $\alpha_{\rm p} \ll \theta$ (i.e., the pitch angle of the particle, $\alpha_{\rm p}$ is less than the incident angle of the radio photons, θ), the particle pitch angle increases but the total momentum stays roughly constant. When $(\theta - \alpha_{\rm p}) \ll \theta$, the pitch angle stays constant while the total momentum increases. Petrova (2002) [119] has derived the solution for the distribution function of electrons undergoing resonant absorption of radio emission in a pulsar magnetosphere. In the case where $\alpha_{\rm p} \ll \theta$ (eq.(2.17) in Petrova 2002), the mean square of the pitch angle is

$$\langle\alpha_{\rm p}^2\rangle = 4R_{\rm NS}\int_{\eta_{\rm r}}^{\eta} a(\eta')d\eta', \tag{103}$$

where $\eta = r/R_{\rm NS}$, and $\eta_{\rm r}$ is the radio emission altitude,

$$a(\eta) = \frac{2\pi^2 e^2(1-\beta\mu)I_0}{\gamma^2 m_{\rm e}^2 c^4}\left[\frac{\varepsilon\gamma(1-\beta\mu)}{B'}\right]^{\nu},\ \eta > \eta_{\rm r}, \tag{104}$$

where I_0 is the intensity of observed radio emission measured in erg cm^{-2} s^{-1} Hz^{-1} and ν is the radio spectral index. Thus, we can write the change of the perpendicular momentum due to cyclotron resonant absorption as

$$\left(\frac{dp_\perp}{dt}\right)^{\rm abs} = 2a(\eta)c\frac{\gamma^2}{p_\perp} + \frac{p_\perp}{p}\left(\frac{dp}{dt}\right)^{\rm abs}, \tag{105}$$

where we used the relationship $p_\perp = p\langle\alpha_p^2\rangle^{1/2}$. Thus, we assume that $p_\perp$ is proportional to the root mean square value of the pitch angle. HSDF08 [60] also make the further approximate the evolution of the particle distribution function. Since the primary and secondary electrons are continuously accelerating, γ remains very high and $p_\perp/p = \sin\alpha_p \ll 1$. According to Petrova (2003) [120], the width of the $p_\perp$ distribution is of order $p_\perp$, so that the large variations in γ and p in r along the field lines are much more important in calculating the spectrum than the spread in the $p_\perp$ distribution.

Combining eqs.(104) and (105), the rate of resonant absorption can be written

$$\left(\frac{p_\perp}{dt}\right)^{\rm abs} = D\frac{\gamma^\nu}{p_\perp} + \frac{p_\perp\gamma}{\gamma^2-1}\left(\frac{d\gamma}{dt}\right)^{\rm abs}, \ \gamma < \gamma_{\rm r}, \tag{106}$$

where

$$D = 5.7\times10^9 {\rm s}^{-1}\gamma_{\rm res}^{-\nu}\left(\frac{d_{\rm kpc}}{\eta}\right)^2 F_{\rm radio}[{\rm mJy}](1-\beta\mu), \tag{107}$$

and we also can neglect $(d\gamma/dt)^{\rm abs}$ in eq.(106), since it is small compared to $(d\gamma/dt)$ from acceleration or curvature and synchrotron losses. In the above expression, we have assumed that $I_0 = F_{\rm radio}\Omega_{\rm p,r}d^2/A_{\rm abs}$, where $F_{\rm radio}$ is the measured flux (in mJy), $d_{\rm kpc}$ is the source distance (in kpc), $\Omega_{\rm p,r} \sim A_{\rm abs}/r^2_{\rm abs}$ is the radio emission solid angle, with the cross-sectional area $A_{\rm abs}$ and radius at the absorption radius $r_{\rm abs}$. Also, from the resonant condition, $\gamma < \gamma_{\rm res}$, we have $\gamma_{\rm res}$ where

$$\gamma_{\rm res} = \frac{B'}{\varepsilon(1-\beta\mu)} = 2.8\times10^5\frac{B_8}{\varepsilon_{\rm GHz}(1-\beta\mu)}. \tag{108}$$

The resonant terms will switch on only when the resonant condition is satisfied.

When $\theta - \alpha_p \ll \theta$, HSDF08 [60] assume that the pitch angle remains at the value $\alpha_p = \theta/2$ and the total mean particle momentum evolves as [120]

$$\bar{p} = \frac{\Gamma[3/(3-\nu)]}{\Gamma[2/(3-\nu)]}\left[\frac{(3-\nu)a_1}{b_1\theta^2}\right]^{1/(3-\nu)}, \tag{109}$$

where

$$a_1(\eta) = \frac{4\pi^2e^2J_1'^2I_0}{c^2}\left(\frac{\epsilon_0\theta}{B'm_{\rm e}c}\right)^\nu, \ \eta > \eta_{\rm r}, \tag{110}$$

and

$$b_1 = \frac{2e^2B'^2}{3\hbar^2c}. \tag{111}$$

Here, J_l is the Bessel function and J_l' is its derivative.

At each step along a field line, the particle radiates an instantaneous synchrotron spectrum, given by [147]

$$\dot{N}_{\rm SR}(\varepsilon) = \frac{2^{2/3}}{\Gamma(1/3)}\alpha_f B'\sin\alpha_p\varepsilon^{-2/3}\varepsilon_{\rm SR}^{-1/3}\exp(-\varepsilon/\varepsilon_{\rm SR}), \tag{112}$$

where $\sin\alpha_p = p_\perp/p$, $p^2 = \gamma^2 - 1$ and $\varepsilon_{\rm SR} = (3/2)\gamma^2B'\sin\alpha_p$ is the synchrotron critical energy. It is important to point out that the radiation power produced in this process comes mainly from the parallel energy of the relativistic particles, not from the power of the radio emission (which is relatively much smaller). The absorption of radio photons increases the pitch angles of the particles that already have very high γ. For high γ, the pitch angle remains approximately constant, while the particle radiates synchrotron radiation, because the radiated photons are emitted nearly perpendicular to the magnetic field in the frame of circular motion, and therefore nearly along (within angle $\sim 1/\gamma$) the particle momentum in the lab frame. The particle then recoils in a direction opposite to its motion, decreasing $\gamma_\perp$ and $\gamma_\parallel$ in proportion to each other, allowing the parallel component of energy to be tapped.

The primary electrons will also scatter radio photons without the cyclotron resonance. HSDF08 [60] treat this component as a non-resonant Compton scattering, which will be in the Thomson limit since $\gamma\varepsilon_0 \ll 1$. The spectrum of scattered photons can be written

$$\frac{dN_{\rm ICS}}{d\varepsilon_s d\mu_s} = \frac{c}{\gamma(1-\beta\mu_s)} \left[\int d\phi \int d\varepsilon \int_{\mu_{\rm min}}^{\mu_{\rm max}} d\mu n_{\rm ph}(\varepsilon,\mu) \frac{d\sigma'(\varepsilon,\mu')}{d\varepsilon'_s d\mu'_s}(1-\beta\mu) \right], \tag{113}$$

where ε and ε_s are the incident and scattered photon energies in the lab frame, μ and μ_s are the cosines of the incident and scattered photon angles in the frame, and $n_{\rm ph}(\varepsilon,\mu)$ is the number density of incident radio photons. The primes denote the corresponding quantities in the frame by the Lorentz transformations

$$\begin{aligned} \varepsilon' &= \gamma\varepsilon(1-\beta\mu), & (114) \\ \mu' &= \frac{\mu-\beta}{(1-\beta\mu)}, & (115) \end{aligned}$$

with same type of expression for the scattered quantities. The differential cross section for scattering of an electron in a magnetic field, averaged over photon polarization, in the Thomson limit, is written (e.g., Dermer 1990 [41])

$$\begin{aligned} \frac{d\sigma'(\varepsilon',\mu')}{d\varepsilon'_s d\mu'_s} &= \frac{3}{8}\sigma_{\rm T}\delta(\varepsilon_s-\varepsilon_s) \\ &\times \left\{ (1-\mu_s'^2)(1-\mu'^2) + \frac{1}{4}(1+\mu_s'^2)(1+\mu'^2) \left[\frac{u^2}{(u+1)^2} + \frac{u^2}{(u-1)^2} \right] \right\}, \end{aligned} \tag{116}$$

where $u = \varepsilon'/B'$. Since the primary electrons have high Lorentz factors, the incident photons will be beamed into a narrow cone with $\theta' \sim 1/\gamma$, so that $\mu' \sim 1$. The radio photons will also lie at energies near or above the cyclotron resonance in the electron rest frame, and the cross section of non-resonant part of the scattering is approximated as

$$\frac{d\sigma'(\varepsilon',\mu')}{d\varepsilon'_s d\mu'_s} = \frac{3}{16}\sigma_{\rm T}\delta(\varepsilon'_s-\varepsilon_s)(1+\mu_s'^2)(1+\mu'^2). \tag{117}$$

For the incident radio photon distribution local to the primary electrons, we use the form

$$n_{\rm ph}(\varepsilon,\mu) = n_{\rm r}\delta(\varepsilon-\varepsilon_0)\Theta(\mu), \tag{118}$$

where $n_{\rm r}$ is the local radio photon density. HSDF08 [60] approximate the energy density distribution as a δ-function at energy ε_0. We estimate the radio photon density as

$$n_{\rm r} = \frac{L_{\rm r}}{\varepsilon_0 A(r) c}, \tag{119}$$

where

$$L_{\rm r} = 2.87 \times 10^{10} P^{-1.3} \dot{P}^{0.4} {\rm mJy\ kpc^2\ MHz}, \tag{120}$$

and $A(r) \sim \pi r^2[(\bar{\theta} + w_e)^2 - (\bar{\theta} - w_e)^2]$, assuming interaction mostly with photons from the conal component, where w_e is the width of the radio cone beam. For the angular distribution HSDF08 [60] adopt

$$\Theta(\mu) = \frac{1}{(1-\beta\mu)^3}\left[1 - \frac{(1-\mu^2)\cos^2\phi}{\gamma_r^2(1-\beta\mu)^2}\right], \tag{121}$$

which is expected for relativistic particles with Lorentz factor γ_r. Eq.(121) describes the distribution of coherent radio emission from pairs with Lorentz factors in the range $\gamma_r \sim 10^2$. In order to calculate the spectrum of scattered photons, we change variables from μ to ε' in eq.(113) by means of the Lorentz transform in eq.(114). The ϕ integration can be done easily. We then make use of the δ-functions to perform the ε and ε' integrations and perform the integration over the scattered photon angle μ_s numerically.

The Lorentz factors, γ, and perpendicular momentum, $p_\perp$ (in units of $m_{\rm e}c^2$), of each particle will evolve along the field lines according to its equation of motion, which may be written

$$\frac{d\gamma}{dt} = \frac{eE_\parallel}{m_{\rm e}c} - \frac{2e^4}{3m_{\rm e}^3c^5}B^2p_\perp^2 - \frac{2e^2\gamma^4}{3R_{\rm cur}^2} + \left(\frac{d\gamma}{dt}\right)^{\rm abs}, \tag{122}$$

$$\frac{dp_\perp}{dt} = -\frac{3}{2}\frac{c}{r}p_\perp - \frac{2e^4}{3m_{\rm e}^3c^5}B^2\frac{p_\perp^3}{\gamma} + \left[\frac{dp_\perp(\gamma)}{dt}\right]^{\rm abs}. \tag{123}$$

The terms of the right-hand side of eq.(122) are acceleration, synchrotron losses, curvature radiation losses, and cyclotron/synchrotron absorption. The terms of the right-hand side of eq.(123) are adiabatic changes along the dipole field line, synchrotron losses, and cyclotron/synchrotron resonant absorption. The inverse Compton scattering losses for the primary particles and pairs may be neglected, since the acceleration and synchrotron loss rates are much larger.

By substituting eq.(105) into the right-hand sides of eqs.(122) and (123), we get

$$\frac{d\gamma}{dt} = A_1E_\parallel - B_1B_8^2p_\perp^2 - C_1\gamma^4, \tag{124}$$

$$\frac{dp_\perp}{dt} = -A_2\eta^{-1}p_\perp - B_1B_8^2p_\perp^3\frac{1}{\gamma} + \left(\frac{dp_\perp}{dt}\right)^{\rm abs}, \tag{125}$$

where $A_1 = 1.76 \times 10^7$ s^{-1}, $B_1 = 1.93 \times 10^7$ s^{-1}, $C_1 = 5.6 \times 10^{-3}$ s^{-1}, $A_2 = 4.5 \times 10^4$ s^{-1}, $E_\parallel$ is in esu, and $B_8 \equiv B/10^8$G. Since Petrova (2002) [119] has assumed that p and γ are constant to compute the change in pitch angle due to resonant absorption, we have neglected the change in γ due to absorption in eq.(124). Both $E_\parallel$ and B_8 are functions of η. For the primary electrons, $E_\parallel$ is computed using eqs.(92), (93) and (94). For the pairs, $E_\parallel = 0$ is used.

HSDF08 [60] modeled the Crab spectrum and pulse profile using their gap model of emission from primary electrons accelerating in the slot gap and non-accelerating electron-positron pairs flowing along field lines outside the slot gap (i.e., field lines at smaller colatitude). Polar cap pair cascade models studied by Daugherty and Harding (1996) [39], and

Muslimov and Harding (2003) [110] find that pair multiplicity (number of pairs per primary particle) for the Crab is in the range 10^4-10^5, where the former study [39] should be applied to colatitudes nearer the magnetic axis while latter one [110] to the cascades extending to higher altitudes of 3-4 stellar radii, initiated by electrons accelerating in the slot gap. In simulating the radiation from pairs, HSDF08 [60] trace particles along all open field lines with an assumed broken power-law spectrum of energies

$$\mathcal{N}_{\rm pairs}(\gamma_{\rm p}) = \begin{cases} A_1\gamma_{\rm p}^{-\delta_1}, & \gamma_{\rm p}^{\rm min} < \gamma_{\rm p} < \gamma_{\rm p}^{\rm br}, \\ A_2\gamma_{\rm p}^{-\delta_2}, & \gamma_{\rm p}^{\rm br} < \gamma_{\rm p} < \gamma_{\rm p}^{\rm max}, \end{cases} \tag{126}$$

where the normalization constants are set to preserve the total pair multiplicity $\mathcal{M}_{\rm pairs}$ in each ring. HSDF08 [60] adopt parameters where the slot gap high-altitude emission reproduces the Crab phase-averaged spectrum. Pair multiplicity was varied in rings over the polar cap, such that

$$\mathcal{M}_{\rm pairs}(r_{\rm ov}) = \begin{cases} 4\times 10^3, & 0.25 < r_{\rm ov} < 0.5, \\ 2\times 10^4, & 0.5 < r_{\rm ov} < 0.9, \\ 4\times 10^5, & 0.9 < r_{\rm ov} < 0.99. \end{cases} \tag{127}$$

The multiplicity of cascades on the field lines near the magnetic axis is lower than that for cascades near the slot gap. Since $E_{\|}$ near the slot gap has a lower magnitude, primary electrons accelerate and produce extended cascades over much longer distances. The primary electrons also produce most of the cascades during their radiation reaction limited phase, further increasing the multiplicity of pairs near the slot gap.

Figure 18 shows phase plots of high-energy emission assuming the radio emission model described by Gonthier, Van Guilder and Harding (2004) [51] for three energy bands: 1 - 20 keV, 0.1 - 10 MeV and $>$ 100 MeV. The radiation distribution shown in the high-energy phase plots exhibits caustics, extended bright lines of emission from particles on the trailing field lines from each pole. Because of retardation, aberration and field line curvature, the emission at a wide range of altitudes arrives in the same phase, while emission on the leading edge of the open volume is spread out [108, 44]. Pulse profiles for these energy bands are obtained by displaying the intensity as a function of phase at a particular viewing angle ζ. At viewing angles that cut across caustics, the profiles show two peaks with phase separation less than 180°. HSDF08 [60] also show the phase plot at 400 MHz of the radio emission, which is dominated by the cone beam. The cone beam is shifted earlier in phase relative to the core beam due to the difference in aberration and retardation of the higher-altitude cone emission. Inclination angles in the range $\alpha = 40°-55°$ give the best combination of spectrum and profile to match the Crab. For large inclination angles, the parallel electric field reverses the direction on some field lines (see [110]), and for small inclination angles, radiation from the low-altitude pair cascades dominates the emission and produces double-peaked profiles for small viewing angles [110]. For inclination angle $\alpha = 45°$, viewing angles in the range $\zeta = 78° - 82°$ and $\zeta = 98° - 102°$ produce profiles having two peaks with phase separation near 0.4. The phase-averaged emission spectra are very similar even for the different angles in this range. The profiles for energy bands 1 - 20 keV and 0.1 - 10 MeV look identical because both are entirely due to pair synchrotron radiation which depends on geometry only. The profile for energies $>$ 100 MeV is significantly different, with the first peak larger

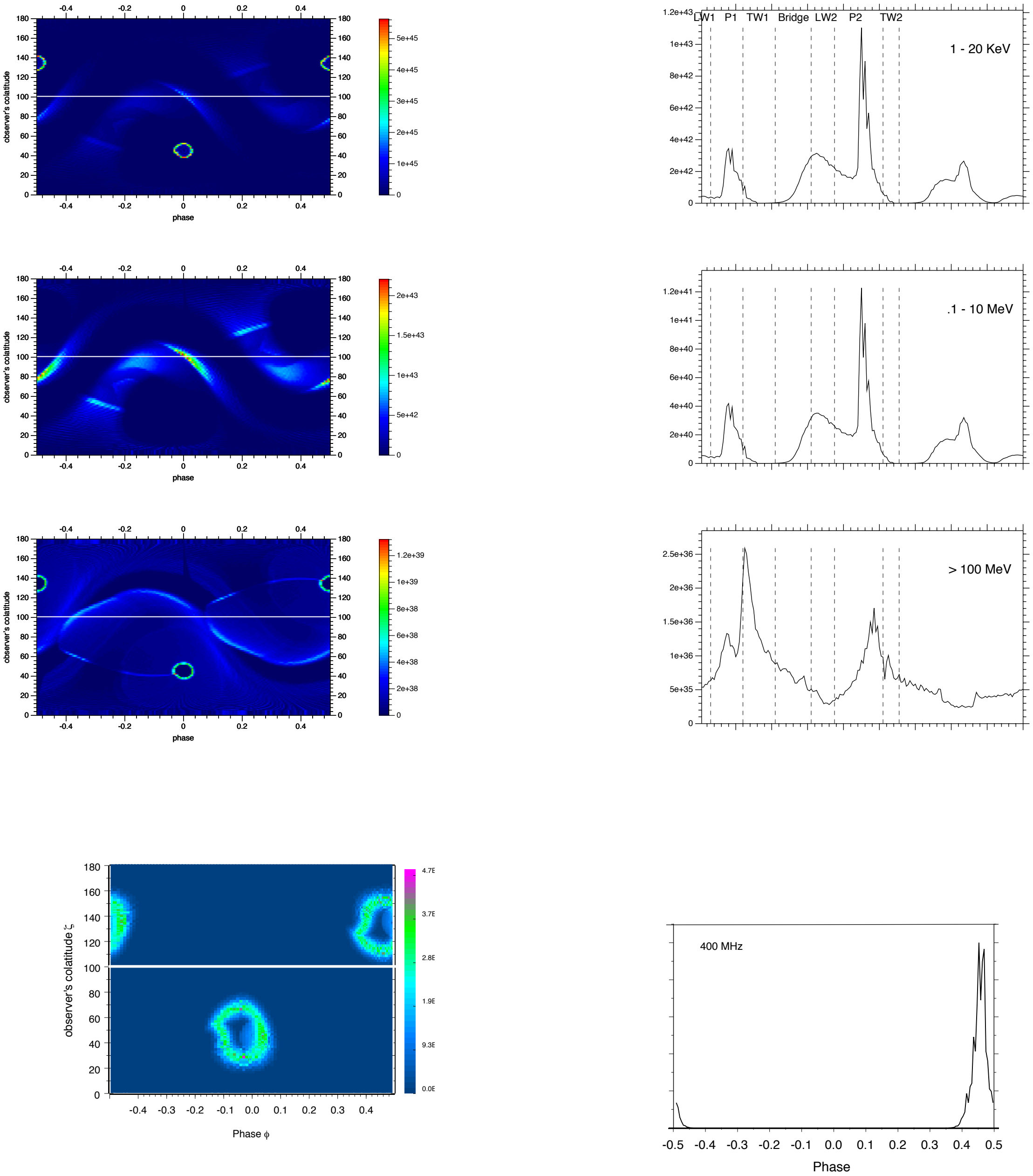

Figure 18: Model pulse profiles and intensity maps (observer angle ζ vs. rotation phase ϕ) in different frequency ranges as labeled for the case of standard radio beam model and inclination angle of $\alpha = 45°$. Profiles are shown for observer angle $\zeta = 100°$. The scale of the high-energy intensity maps is in units of photons s^{-1} sr^{-1} and the scale of the profiles is in units of photons s^{-1} sr^{-1} N_{ϕ}^{-1}, where $N_{\phi} = 180$ are the number of phase bins. The scale of the radio map is in mJy kpc^2 sr^{-1}. Figures adopted from HSDF08 [60].

than the second peak, and the phases somewhat shifted from those at lower energy. While the high-energy profiles can reasonably reproduce the observed ones, the profile at radio is not reproduced it. HSDF08 [60] modified the model of radio beam to extend emission region. Their extended cone-beam-model reproduces observed radio pulse profiles and the small modification dose not affect the high-energy emission. The phase-averaged flux for an observer at viewing angle ζ is the sum over the emission in the profile divided by source distance squared. For the viewing angle $\zeta = 100°$ shown in figure 18 and distance of 2 kpc, the phase-averaged flux is $\langle\Phi(> 100\mathrm{MeV})\rangle = 4.3 \times 10^{-6}$ photons s^{-1} cm^{-1} and $\langle\Phi(0.1$ - 10 MeV$)\rangle = 0.05$photons s^{-1} cm^{-1}, which are in good agreement with observed values.

Figure 19 shows the phase-averaged model spectrum for the case $\alpha = 45°, \zeta = 100°$. Four components are visible and three components make significant contributions to the total. Synchrotron radiation from pairs contributes at the lowest energies, from infrared and optical through hard X-rays, turning over around 20 MeV. This component reflects the pair spectrum in a range, with the low energy turnover determined by $\gamma_p^{\min}$, the high-energy turnover by $\gamma_p^{\max}$, the break dividing lower and upper slopes by γ_p^{br}, δ_1 and δ_2. Synchrotron radiation from primary electrons contributes at the mid-range of 20 - 300 MeV and has a smaller energy range, reflecting the smaller energy range of the primaries. Finally, curvature radiation from primaries contributes at the highest energies, from ~ 100 MeV to the turnover at around 5 GeV that is determined by the parameters of $E_\parallel$. The components due to non-resonant ICS from primaries and from pairs (which appears below the scale of the plot) are negligible. The non-resonant Compton scattering contribution is much lower than that of resonant absorption because the cyclotron absorption cross section is orders of magnitude higher, being a first order process, than the Thomson cross section for non-resonant ICS, being a second-order process. Furthermore, the particles absorb many photons at the resonant before radiating the most significant synchrotron emission, reaching high Landau levels. Thus resonant absorption ratio to ICS is even larger than the cross section ratio. Curvature radiation from pairs is also negligible since their Lorentz factors are much lower than that of the primary electrons. HSDF08 [60] have adjusted the model parameters within a reasonable range. The pair spectrum can be tuned to match the optical-to-X-ray spectrum very well by adjusting its energy range and shape, as well as the variation of multiplicity across the polar cap. The best fit values are not far from those of pair cascade calculations. The model spectrum does not match the high-energy spectrum quite as well, with the peak of the curvature spectrum that gives a high cutoff energy being somewhat above the data points, although the EGRET data points have large errors. Using re-examined sensitivity of the EGRET, Stecker et al. (2007) [143] concluded that phase-averaged spectral points for the Crab (and indeed those of all EGRET sources) should be systematically lowered by a factor of 2 above 1 GeV. HSDF08 [60] also plot these corrected points in figure 19 and they provide an improved match to the model spectrum. The multicomponent nature of the model spectrum produces dip around 20 MeV. The observed spectrum seems to show the dip.

The phase-resolved spectra are shown in figure 20, for the phase ranges adopted by Kuiper et al. (2001) [85] to study the Crab pulsed emission. The model spectra are obtained by summing the emission for the equivalent phase intervals (Peak 1 occurs at phase 0.41 and Kuiper et al.'s Peak 1 occurs at phase 0.0) in the phase plots at chosen viewing angle. The flux levels of the resulting model spectra were plotted with the data from the corresponding

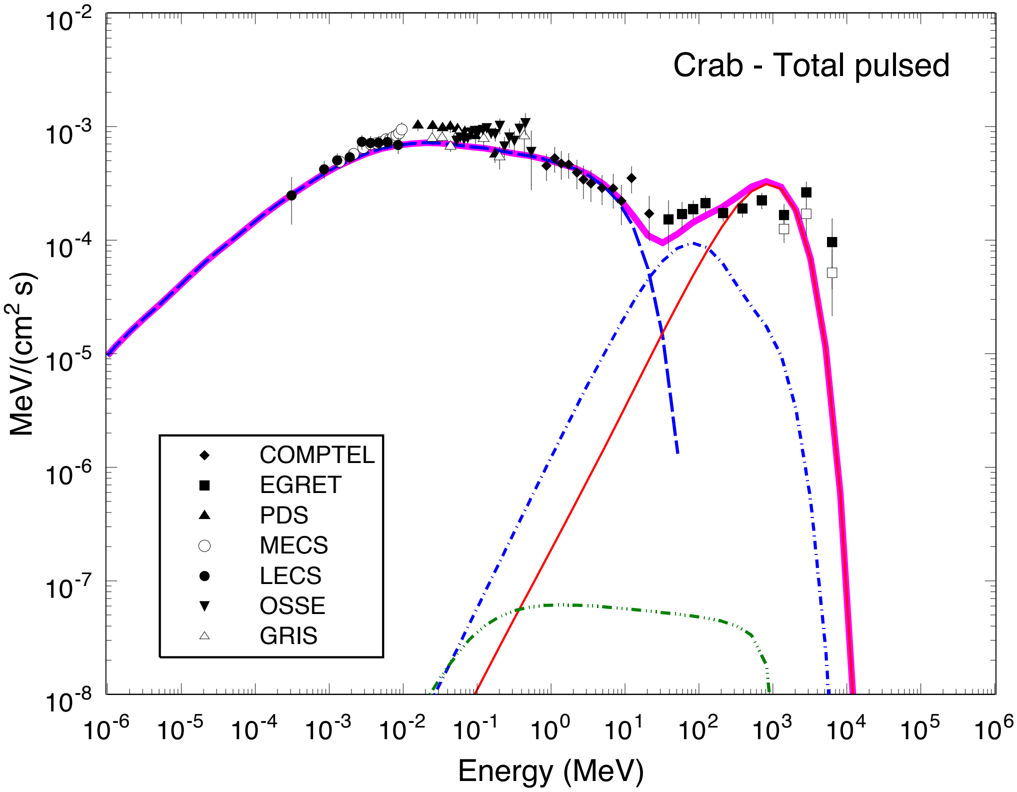

Figure 19: Model spectrum of phase-averaged total pulsed emission (heavy solid line) that is the sum of emission components from curvature (light solid line), synchrotron (dashed-dot line) and inverse Compton (dashed-dot-dot line) radiation of primary electrons in the slot gap and synchrotron radiation from pairs (dashed line) inside the slot gap. Data points are from Kuiper et al. (2001) [85]. The open squares are corrected EGRET values above 1 GeV from Stecker et al. (2007) [143]. Figure adopted from HSDF08 [60].

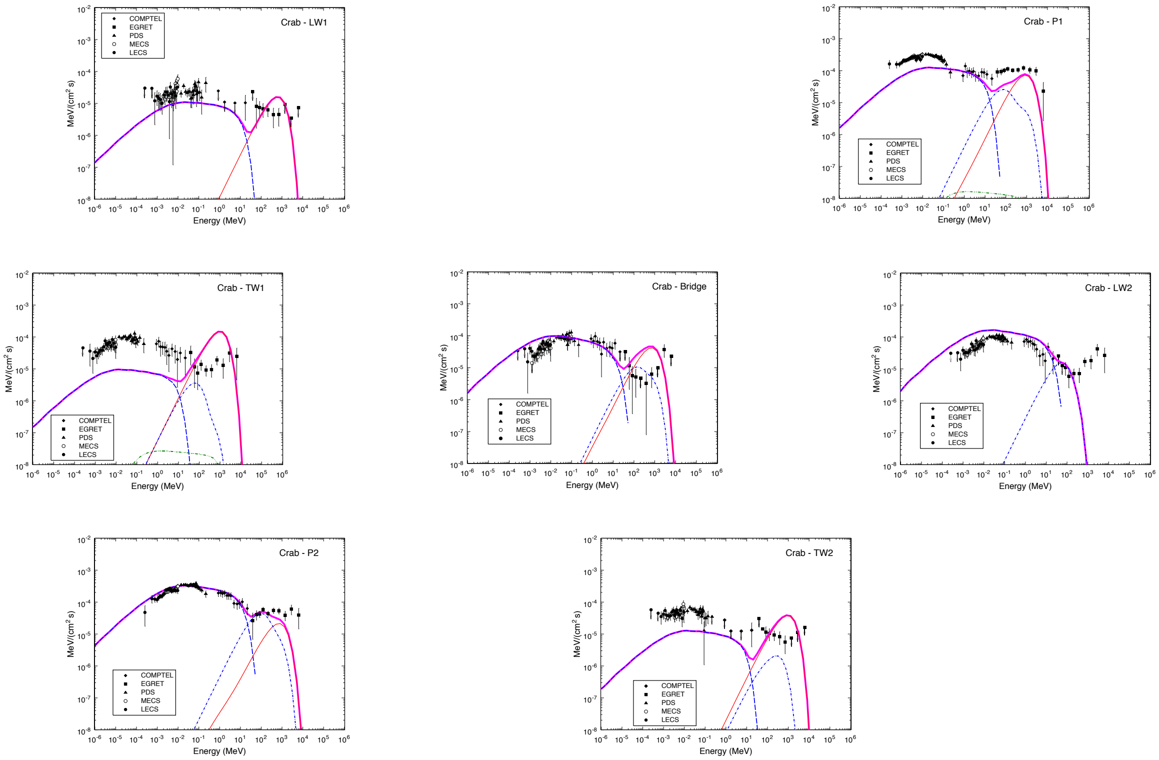

Figure 20: Model spectrum of total pulsed emission in different phase intervals (heavy solid line) that is the sum of emission components from curvature (light solid line), synchrotron (dashed-dot line) and inverse Compton (dashed-dashed-dot line) radiation of primary electrons in the slot gap and synchrotron radiation from pairs (dashed line) inside the slot gap. Figures adopted from HSDF08 [60].

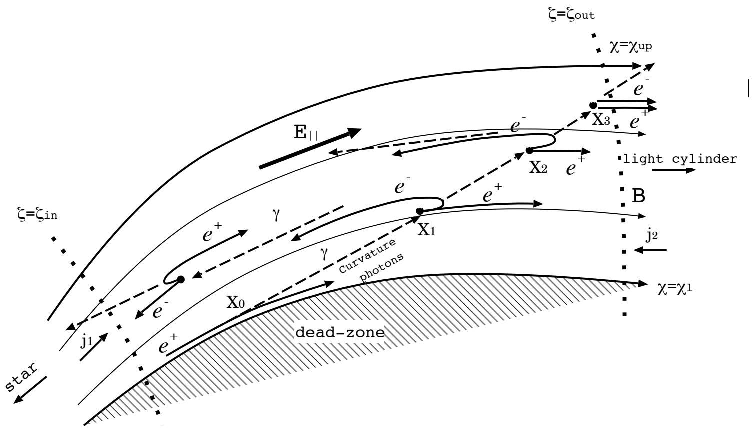

Figure 21: The pair creation cascade in the outer gap model. The γ-rays are radiated by the curvature process and are beamed in the direction of local magnetic field. The radiated γ-ray may convert into pairs by the pair creation process. The χ_1, $\chi_{\rm up}$, $\zeta_{\rm in}$ and $\zeta_{\rm out}$ present the lower, upper, inner and outer boundaries of the gap, respectively. Figure adopted from Takata, Shibata and Hirotani (2004) [148].

phase intervals without any renormalization. The data and model spectra match fairly well for the P1, P2 and bridge intervals. The primary synchrotron component makes a larger contribution in the peaks and the bridge, which is expected since the primary electrons radiate only along a narrow set of field lines.

In summary, the calculation based on the slot gap model [60] has explained the observations of Crab pulsar in optical to γ-ray bands. This model includes two distributions of particles radiating along open field lines at high altitude: primary electrons accelerating in the slot gap from the stellar surface to almost the light cylinder, and non-accelerating electron-positron pairs on field lines bordering and interior to the slot gap. All particles are flowing only in outgoing direction. In this model, three different components dominate the Crab phase-averaged spectrum, curvature and synchrotron radiation of primary electrons and synchrotron radiation of pairs. The synchrotron radiation is a result of cyclotron resonant absorption of radio photons in the low magnetic field at high altitude.

3.3.3 Outer gap model

We consider outer gap model. On some field lines, where $\mathbf{\Omega} \cdot \mathbf{B} = 0$, the GJ charge density changes the sign. Clearly, the charge-separated plasma flowing from the star could not ensure the condition $\rho = \rho_{\rm GJ}$. Therefore, the existence of an outer gap in the vicinity of the line $\rho_{\rm GJ} = 0$ was put forward, in which the emerging longitudinal electric field also produces the secondary plasmas. However, because of a weak magnetic field, the magnetic pair creation becomes impossible. Therefore, the main particle generation mechanism is the photon-photon pair creation processes [30]. The chain of process is the following:

1. The occurrence of the longitudinal electric field, because of the condition $\rho \neq \rho_{\rm GJ}$.

2. The acceleration of primary particles.

3. The emission of curvature photons.
4. The secondary particles generated by the collision of curvature photons with soft X-ray photons from stellar surface.

The schematic view of the electromagnetic cascade in the outer gap model is shown in figure 21.

At present, Takata and Hirotani (e.g., [148, 66, 149]) have carried out thorough computations of the pair cascade processes in the outer gap. They consider a stationary structure in the magnetic meridional plane, which includes the magnetic and rotational axes. The magnetic field structure is assumed as a dipole field. In the meridional plane, they solve the Poisson equation of the accelerating electric field, the continuity equation for electrons and positrons on each magnetic field line, and the pair-creation process by γ-rays and surface X-rays. They assume that newborn particles via the pair-creation process in the gap are quickly saturated between the accelerating force and radiation reaction force, instead of solving the evolutions of the Lorentz factor and the pitch angle. The saturation treatment is a good assumption, and simplifies the problem to obtain an outer gap structure with an iterating method.

Here we review their approaches to characterize the observational properties of the outer gap model. The stationary electric potential, $\phi_{\rm nco}$, for the accelerating field is obtained from

$$\triangle\phi_{\rm nco}(\mathbf{r}) = -4\pi[\rho(\mathbf{r}) - \rho_{\rm GJ}(\mathbf{r})]. \tag{128}$$

Using the assumption that the gap dimension in the azimuthal direction is much larger than that in the meridional plane, we rewrite above equation as

$$\triangle_{r,\theta}\phi_{\rm nco}(\mathbf{r}) = -4\pi[\rho(\mathbf{r}) - \rho_{\rm GJ}(\mathbf{r})], \tag{129}$$

where $\triangle_{r,\theta}$ represents the (r,θ) parts of the Laplacian.

The continuity equation for the particles is written as

$$\mathbf{B}\cdot\nabla\left[\frac{v_\parallel N_\pm(\mathbf{r})}{B}\right] = \pm S(\mathbf{r}), \tag{130}$$

where $v_\parallel \sim c$ is the velocity along the field line, $S(\mathbf{r})$ is the source term due to the pair-creation process, and N_+ and N_- respectively denote the number densities of the outgoing and ingoing particles (i.e. the positrons and electrons in the present case). The pair creation contributes to the source term $S(\mathbf{r})$ in eq.(129). The creation rate is calculated from

$$\eta_{\rm p}(\mathbf{r}, E_\gamma) = (1-\cos\theta_{X\gamma})c\int_{E_{\rm th}}^{\infty} dE_X \frac{dN_X}{dE_X}(\mathbf{r}, E_X)\sigma_{\gamma\gamma}(E_\gamma, E_X), \tag{131}$$

where $dE_X(dN_X/dE_X)$ is the X-ray number density between energies E_X and E_X+dE_X, $\theta_{X\gamma}$ is the collision angle between a X-ray photon and a γ-ray photon, and $E_{\rm th} = 2(m_{\rm e}c^2)^2/(1-\cos\theta_{X\gamma})E_\gamma$ is the threshold X-ray energy for the pair creation. The cross section $\sigma_{\gamma\gamma}$ is given by eq.(18). In this case, $\beta_{\rm cm}$ is given by

$$\beta_{\rm cm}(E_\gamma, E_X) = \left(1 - \frac{2}{1-\cos\theta_{X\gamma}}\frac{(m_{\rm e}c^2)^2}{E_\gamma E_X}\right)^{1/2}. \tag{132}$$

In the gap, the GeV photons collide with the thermal X-ray photons from the stellar surface. At the radial distance r from the center of the star, the number density of thermal photon between energy E_X and $E_X + dE_X$ is given by

$$\frac{dN_X}{dE_X} = 2\pi \left(\frac{1}{ch}\right)^3 \left(\frac{R_{\rm eff}}{r}\right)^2 \frac{E_X^2}{\exp(E_X/k_{\rm B}T_{\rm s}) - 1}, \tag{133}$$

where $R_{\rm eff}$ is the effective radius of the emitting region, and $k_{\rm B}T_{\rm s}$ refers to the surface temperature. Both values of $R_{\rm eff}$ and $k_{\rm B}T_{\rm s}$ are observationally determined. With the soft photons from the stellar surface, the collision angle $\theta_{X\gamma}$ of the γ-ray photon after travelling a distance s from the emission point (r_0, θ_0) is obtained from

$$\cos\theta_{X\gamma}(\mathbf{r}) = \frac{s + r\cos\theta_{\rm em}}{r}, \tag{134}$$

where $\theta_{\rm em}$ is the angle between the emission and the radial directions at the emission point, which is $\cos\theta_{\rm em}^{+} = \sqrt{1 - (r_0 \sin\theta_0 \Omega/c)^2 B_r(r_0,\theta_0)/B(r_0,\theta_0)}$ for the outwardly propagating γ-rays, and $\cos\theta_{\rm em}^{-} = -\sqrt{1 - (r_0 \sin\theta_0 \Omega/c)^2 B_r(r_0,\theta_0)/B(r_0,\theta_0)}$ for the inwardly propagating γ-rays.

In order to calculate the source term $S(\mathbf{r})$ in eq.(129) at each point, the Monte Carlo method is used to simulate the pair creation. A γ-ray may convert into a pair at distance s with the probability

$$P_{\rm p}(s) = \frac{\int_0^s 1/l_{\rm p} ds}{l_{\rm p}}, \tag{135}$$

where $l_{\rm p} = c/\eta_{\rm p}$ is the mean-free path of the pair creation.

Saturated motion is assumed for the stationary electric field structure. By assuming that the particle's motion immediately saturates in the balance between the electric and the radiation reaction forces, the Lorentz factor at each point is calculated as

$$\gamma_{\rm sat}(R_{\rm cur}, E_{\parallel}) = \left(\frac{3R_{\rm cur}^2}{2e}E_{\parallel} + 1\right)^{1/4}. \tag{136}$$

In order to solve the Poisson equation (129), we need four boundary conditions, which are called inner, outer, upper and lower boundaries. The lower and upper boundaries are laid on the magnetic surfaces, and the lower boundary is defined by the last-open field line. The inner and outer boundaries are defined by the surfaces on which the accelerating electric field vanishes (i.e. $E_{\parallel} = 0$).

The inner, upper and lower boundaries are directly linked with the star without the potential drop. We then impose that the accelerating potential is equal to zero (i.e. $\phi_{\rm nco} = 0$) on the inner, upper and lower boundaries. The position of the inner boundary is not determined in advance because Dirichlet- and Neumann-type conditions are imposed on it. By moving the inner boundary step-by-step iteratively, the required positions are sought.

At the inner boundary, the condition $j_{\rm g} + j_2 - j_1 = B_z/B$ is satisfied. Here, $j_{\rm g}$ is the current in units of the GJ value carried by the pairs produced in the gap, j_1 and j_2 are the currents carried by the positions and electrons coming into the gap through the inner and outer boundaries, respectively.

In order to compute the synchrotron radiation with the pitch angle, the electric field distribution in the outer gap is used. This is obtained by solving the equation of motion, which describes the evolutions of the pitch angle of the particle. For most pulsars, the inverse-Compton process is less significant for energy loss of the particles than the synchrotron and curvature radiation. The momenta of the parallel ($p_{\parallel}/m_{\rm e}c = \sqrt{\gamma^2-1}\cos\alpha_{\rm p}$) and perpendicular ($p_{\perp}/m_{\rm e}c = \sqrt{\gamma^2-1}\sin\alpha_{\rm p}$) to the magnetic field are respectively described as

$$\frac{dp_{\parallel}}{dt} = eE_{\parallel} - f_{\rm rad,sc}\cos\alpha_{\rm p}, \tag{137}$$

and

$$\frac{dp_{\perp}}{dt} = -f_{\rm rad,sc}\sin\alpha_{\rm p} + \frac{c}{2B}\frac{dB}{ds}P_{\perp}. \tag{138}$$

Here, $f_{\rm rad,sc}$ represents the reaction force of the synchrotron and curvature radiation. The second term on the right-hand side of eq.(138) represents the adiabatic change along the dipole field line. The force $f_{\rm rad,sc}$ is described by [32],

$$f_{\rm rad,sc} = \frac{e^2c\gamma^4Q_2}{12r_c}\left(1+\frac{7}{r_c^2Q_2^2}\right), \tag{139}$$

where

$$r_c = \frac{c^2}{(r_{\rm B}+R_{\rm cur})(c\cos\alpha_{\rm p}/R_{\rm cur})^2 + r_{\rm B}\omega_{\rm B}}, \tag{140}$$

$$Q_2^2 = \frac{1}{r_{\rm B}}\left(\frac{r_{\rm B}^2+R_{\rm cur}r_{\rm B}-3R_{\rm cur}^2}{R_{\rm cur}^3}\cos^4\alpha_{\rm p} + \frac{3}{R_{\rm cur}}\cos^2\alpha_{\rm p} + \frac{1}{r_{\rm B}}\sin^4\alpha_{\rm p}\right) \tag{141}$$

$$r_{\rm B} = \frac{\gamma m_{\rm e}c^2\sin\alpha_{\rm p}}{eB}. \tag{142}$$

The radiation drag $f_{\rm rad,sc}$ equals to $f_{\rm rad,syn}$ (eq.7) for $R_{\rm cur} \gg r_{\rm B}$ while $f_{\rm rad,sc}$ equals to $f_{\rm rad,cur}$ (eq.12) for $R_{\rm cur} \ll r_{\rm B}$. The equations of motion (eqs.137 and 138) are solved up to the light cylinder for the outgoing particles (positrons) and to the stellar surface for the ingoing particles (electrons). The initial pitch angle of the newborn pairs is determined by the angle between the propagating direction of γ-rays and the direction of the magnetic field at the pair creation point.

In the outer gap model, the processes we needed are the curvature radiation, synchrotron radiation and inverse-Compton scattering. The power of the synchrotron-curvature process for a particle is calculated as [32]

$$\begin{aligned} F_{\rm sc,\omega} &= \frac{\sqrt{3}e^2\gamma\omega}{4\pi r_c\omega_c}\Bigg\{\left[\int_{\omega/\omega_c}^{\infty}K_{5/2}(y)dy - K_{2/3}(\omega/\omega_c)\right] + \frac{[(r_{\rm B}+R_{\rm cur})(c\cos\alpha_{\rm p}/R_{\rm cur})^2 + r_{\rm B}\omega_{\rm B}]}{c^4Q_2^2} \\ &\times \left[\int_{\omega/\omega_c}^{\infty}K_{5/2}(y)dy + K_{2/3}(\omega/\omega_c)\right]\Bigg\}, \end{aligned} \tag{143}$$

where

$$\omega_c = \frac{3}{2}\gamma^3\frac{c}{R_{\rm cur}}\left[\frac{(r_{\rm B}^3+R_{\rm cur}r^2r_{\rm B}-3r_{\rm B}R_{\rm cur})}{R_{\rm cur}r_{\rm B}^2}\cos^4\alpha_{\rm p} + \frac{3\rho}{r_{\rm B}}\cos^2\alpha_{\rm p} + \frac{R_{\rm cur}^2}{r_{\rm B}^2}\sin^4\alpha_{\rm p}\right]^{1/2}. \tag{144}$$

The emissions from the following four different types of electrons and positrons are calculated:

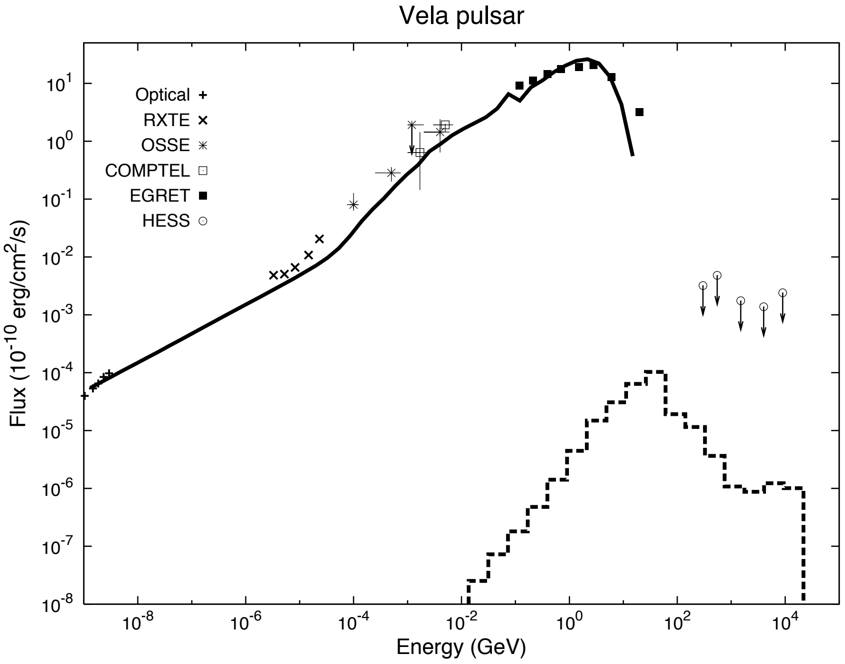

Figure 22: Spectrum of the Vela pulsar. The solid line shows the total spectrum of the curvature and synchrotron radiation from the primary and secondary particles. The observational data are taken from Shibanov et al. (2003) [136] for optical, Harding et al. (2002) [61] for *RXTE*, Strickman et al. (1996) [144] for the Oriented Scintillation Spectrometer Experiment (OSSE) and COMPTEL, Fierro et al. (1998) [47] for EGRET and Konopolko et al. (2005) [81] for the High Energy Spectroscopic System (HESS). Figure adopted from TCS08 [152].

1. primary particles, which are created inside the gap and are accelerated up to ultrarelativistic energy;
2. secondary particles created outside the gap via the pair creation with surface thermal X-ray photons;
3. secondary particles created outside the gap via the pair creation with magnetospheric non-thermal X-ray photons;
4. secondary particles created outside the gap via magnetic pair creation.

For magnetic pair creation, we assume that γ-ray photons are converted into pairs at the point $E_\gamma B \sin\alpha_{\rm p}/B_{\rm c} = 0.2 m_{\rm e} c^2$ [110].

Figure 22 shows an example of the calculated spectrum for Vela pulsar [152]. The solid line in figure 22 shows the spectrum of the total emissions, which include the curvature and synchrotron radiation from the primary and secondary particles. The observational data of the phase-averaged spectrum are also plotted. This figure shows that the calculated spectrum is consistent with the observations in whole energy bands.

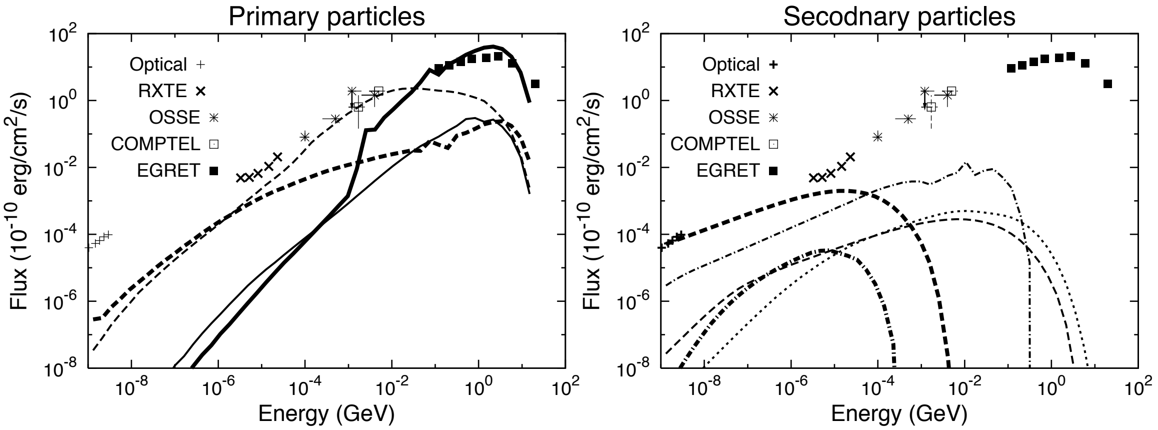

Figure 23: Spectrum of the Vela pulsar. Left: spectra of the curvature (solid lines) and synchrotron (dashed lines) radiation from the primary particles. The thick and thin lines show the emissions from the outgoing particles and ingoing particles, respectively. Right: spectra of the synchrotron radiation of the secondary particles. The dashed line shows the synchrotron spectra of the pairs produced through the pair-creation process by magnetospheric X-rays. The dash-dotted lines are the spectra of the pairs produced by the pair-creation process with surface thermal X-rays. The dotted line shows the spectra of the secondary pairs produced via the pair-creation process with the strong magnetic field. The thick and thin lines show the emissions from the outgoing particles and ingoing particles, respectively. Figure adopted from TCS08 [152].

Figure 23 shows the spectral components from the primary particles (left panel) and secondary particles (right panel). In the left panel, the solid and dashed lines show the spectra of the curvature radiation and the synchrotron radiation of the primary particles, respectively. The thick and thin lines represent the spectra of the outward emissions for the outgoing positrons and those of the inward emissions for the ingoing electrons, respectively.

For the outward emissions by the primary particles, the ratio of the curvature radiation $F_{\rm cur}$ (thick solid line in the left panel of figure 23) to the synchrotron radiation $F_{\rm syn}$ (thick dashed line in the left panel) is $F_{\rm cur}/F_{\rm syn} \sim 10^3$ in the radiation powers. The perpendicular momentum to the magnetic field lines quickly decreases via the synchrotron radiation, and its cooling length is much shorter than the gap width. Therefore, the synchrotron radiation from the primary particles is efficient only near the pair creation position around the inner boundary of the gap. On the other hand, the outward curvature radiation of the outgoing particles takes place at the whole outer gap, because the particles are always accelerated by the electric field in the gap. In such a case, the ratio of the total powers is estimated with

$$\frac{F_{\rm cur}}{F_{\rm syn}} \sim \frac{(2e^2\gamma^4\delta s/3R_{\rm cur}^2)}{m_{\rm e}c^2\gamma_\perp} \sim 2\times 10^3 \left(\frac{\gamma}{10^7}\right)^4 \left(\frac{\gamma_\perp}{10^3}\right)^{-1} \left(\frac{\delta s}{0.5R_{\rm LC}}\right), \tag{145}$$

where δs is the gap width. This estimation $F_{\rm cur}/F_{\rm syn}$ is consistent with the ratio of calculated flux. Although the total power of the outward synchrotron radiation is smaller than that of the curvature radiation, the emissions become important below 1 MeV bands, as the thick dashed line in the left panel of figure 23 shows.

For ingoing primary electrons (thin lines in the left panel), the traveling distance in the gap before escaping from the inner boundary is much shorter than the gap width, because most pairs are produced near the inner boundary. Also, because the maximum Lorentz factor of the ingoing electron is $\gamma \sim 10^7$, which is smaller than that of the outgoing positrons, the ratio of the radiation powers $F_{\rm cur}/F_{\rm syn}$ becomes about unity, as shown by the thin solid and dashed lines in the left panel of figure 23.

In the right panel of figure 23, the spectra of the synchrotron emissions for three types of secondary pairs are shown: the spectra for the secondary pairs produced by magnetospheric X-rays in the dashed lines, those for the pairs produced by surface X-rays in the dash-dotted lines, and those for the pairs produced via the magnetic pair-creation process in the dotted line. The thick and thin lines represent the synchrotron spectra from the outgoing and ingoing moving pairs, respectively.

The dash-dotted lines in figure 23 show that the synchrotron emissions from the outgoing pairs produced by surface X-rays are much fainter than those from the ingoing particles. For the outwardly propagating γ-rays, the pairs are produced by surface X-rays with a tail-on-like collision (i.e. $1-\cos\theta_{X\gamma} \ll 1$). For the ingoing propagating γ-rays, however, the pair creation occurs with a head-on-like collision (i.e. $1-\cos\theta_{X\gamma} \sim 2$). The collision angle is quite different so that the mean-free path of the outgoing γ-rays is much longer than that of the ingoing ones. Because smaller number produced by surface X-rays, the flux of the synchrotron emission for the outgoing pairs is much fainter than that for the ingoing pairs.

For secondary pairs produced by magnetospheric X-ray photons, however, the total energy of synchrotron emission for the outgoing particles is much larger than that for the ingoing particles (dashed lines in the right panel in figure 23). Because the collision angles with magnetospheric X-rays are not different between the outgoing and ingoing γ-ray

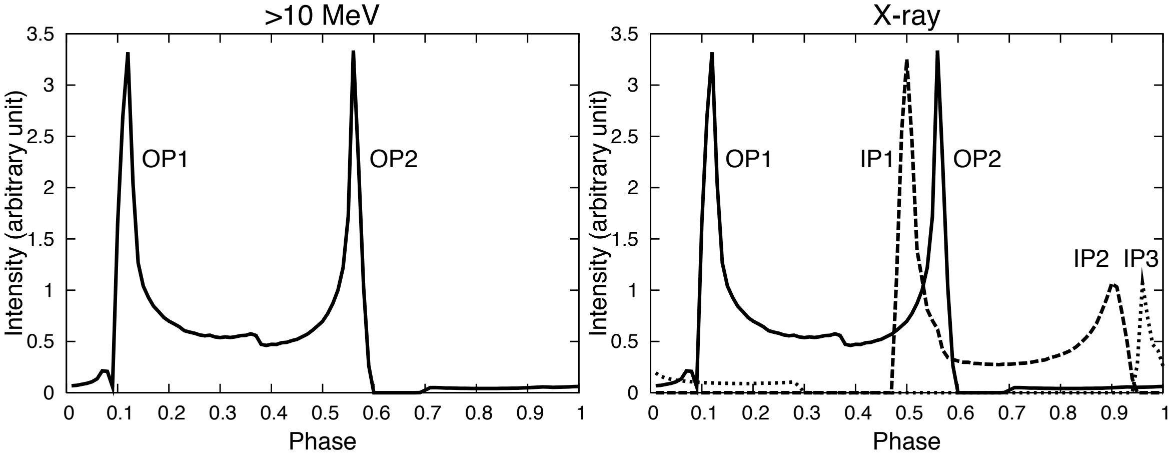

Figure 24: Pulse profile for the Vela pulsar. Left: expected pulse profile in γ-ray bands by the outward emissions. Right: expected pulse profile in X-ray bands. The solid line represents the pulse profile by the outward emissions. The dashed and dotted lines show the pulse profiles by the inward emissions outside and inside the null charge surface, respectively. Figure adopted from TCS08 [152].

photons, the difference between the numbers of created pairs originates from the numbers of γ-ray photons. Because the outgoing γ-rays are more than the ingoing γ-rays, as the left panel of figure 23 shows, more outgoing secondary pairs are produced than ingoing secondary pairs. Therefore, the synchrotron emissions for the outgoing pairs produced by magnetospheric X-rays are brighter than that for the ingoing ones.

From figure 23, we can see which emission process is important in different energy bands. Above 10 MeV, the curvature radiation of the outgoing primary particles (thick solid line in the left panel in figure 23) dominates the other emission processes. Between 100 keV and 10 MeV energy bands, the synchrotron radiation of the ingoing primary particles (thin dashed line in the right panel in figure 23) is major. In soft X-ray bands, the synchrotron emissions irrespective of the directions and produced particles, almost equally contribute to the calculated spectrum to explain the *RXTE* observations. In optical bands, the synchrotron emissions by the secondary pairs (figure 23, right) explain the observations.

Next, we discuss the expected pulse profiles in γ-ray, X-ray, and optical/UV bands using a three-dimensional model. According to figure 23, only outward curvature emissions contribute to the spectrum above 10 MeV. In order to calculate the pulse profile in γ-ray bands, the outward emissions from the inner boundary to the light cylinder are sufficient. Figure 24 (left) shows the expected pulse profile in γ-ray bands. Because only outward emissions contribute to the emissions, a double-peak pulse profile is seen, as general trend for the outer gap model [128, 169].

Unlike the spectrum above 10 MeV, both outgoing and ingoing particles contribute to the spectrum around 1 keV with synchrotron emissions, as figure 23 shows. The right panel of figure 24 shows the pulse profile consisted of both outward and inward emissions. It is expected that the peak positions of the outward synchrotron emissions are aligned for all energy bands above 10 MeV (OP1 and OP2 in figure 24). The dashed and dotted lines represent the pulse positions of the inward emissions beyond and below the null charge surface, respectively. As the dashed lines show, the inward emissions beyond the null charge surface make another two peaks, which are denoted by IP1 and IP2 in the figure, and the inward emissions below the null charge surface make one peak denoted by IP3. Therefore, the present model predicts a multi-peak structure for the pulse profile in X-ray bands for the Vela pulsar.

We compare the expected peak phases in X-ray bands with the peak phases observed by *RXTE* [61], which indicates five peaks in a single period. In *RXTE* observations, the two peaks, which are denoted Pk 1 and Pk 2-soft in figure 1 in Harding et al. (2002) [61], are aligned with those in the γ-ray bands. With the model by TCS08 [152], these two components of *RXTE* are explained by the synchrotron radiation of the outgoing particles, which produce two peaks (OP1 and OP2) relating to the γ-ray pulse profile. The other two peaks observed, which are denoted Pk 2-hard and Pk 3 in figure 1 in Harding et al. (2002) [61], correspond to the peaks denoted by IP1 and IP2, which come from the synchrotron emissions of the ingoing particles beyond the null surface. Remarkably, the model [152] produces the observed phase separation (~ 0.4) of the two peaks.

The observed small peak labeled *RXTE* Pk4 in Harding et al. (2002) [61] can be explained by the inward synchrotron emissions below the null charge surface, which create a peak (denoted with IP3) in figure 24. *RXTE* observations show that the phase of Pk4 is aligned with the radio pulse. The model [152] also expects that the phase of IP3 is close to the radio peak. Polarization studies for the observed radio emissions from young pulsars indicate that the height of the emission is between 1 and 10 per cent of the light cylinder radius [72]. For the inclination angle $\alpha = 65^\circ$, because the radial distance to the null charge surface on the last-open field lines in the meridional plane is about 10 per cent of the light cylinder, the radio emission region will be located near or below null charge surface. For example, if the radio emissions occur at the radial distance of 5 per cent of the light cylinder radius, the radio pulse will be observed at the pulse phase 0 for the observer with a viewing angle $\zeta \sim 97^\circ$. Therefore, there is a possibility that we observe the pulse peak (IP3) from the inward emissions below the null charge at the phase that aligned the radio peak.

The pulse peaks, whose phases are in phase with the two peaks in the X-ray band (*RXTE* Pk1 and Pk2-soft in Harding et al. 2002 [61]) and in the γ-ray bands (OP1 and OP2 in figure 24), disappear in optical/UV bands [126]. Furthermore, a new peak in the optical/UV bands is observed at the phase between the phases of OP1 and OP2 in figure 24. Two peaks in the X- and γ-rays disappear because the primary particles do not contribute to the emissions in optical/UV bands, as figure 23 (left) shows. The emissions from the secondary pairs take place at higher altitude than the altitude of the primary emission regions. In such a case, the phase of the pulse peaks of the outgoing secondary pairs are shifted inside the phases of the peaks produced by the outgoing primary particles. This may be the reason for the shift of the first peak observed in optical/UV bands.

In summary, the above calculation based on the outer gap model by Takata, Chang and Shibata (2008) [152] have explained the observations of Vela pulsar in optical to γ-ray bands. The emissions from both the outgoing and ingoing particles are required to explain the observed spectrum. This model predicts that the curvature radiation of outgoing primary particles is the major emission process above 10 MeV, the outward and inward synchrotron

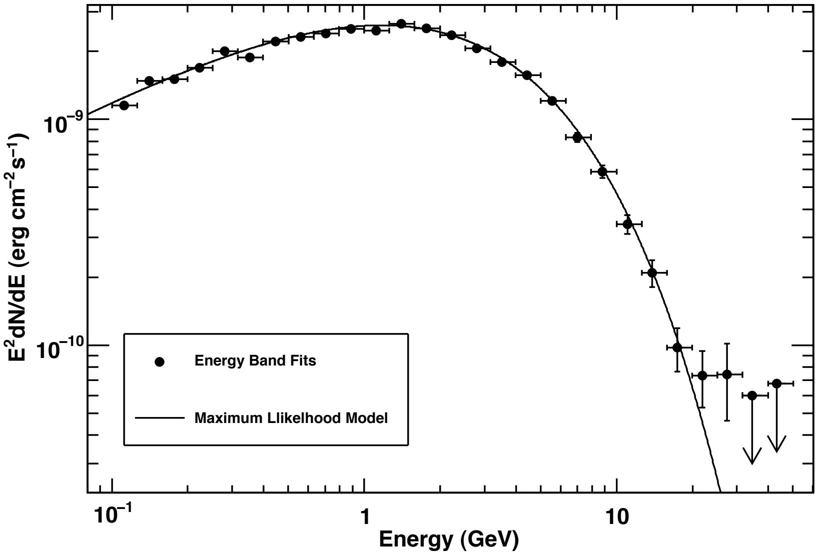

Figure 25: Phase-averaged spectrum for $E > 0.1 - 100$ GeV. Figure adopted from Abdo et al. (2010b) [3].

radiation of the secondary particles explains the optical/UV emissions.

3.3.4 Inner acceleration region vs outer acceleration region

The main differences between the inner acceleration model (polar cap model) and the outer acceleration models (outer and slot gap models) are (1) the cut-off shape in the observed γ-ray spectrum and (2) the relative phase of radio and γ-ray peaks in the observed light curve. In the polar cap model, the observed spectral shape in the GeV γ-ray band is expected to show super-exponential cutoff (figure 16). This is because the strength of the magnetic field at inner acceleration region is strong enough to absorb γ-ray photons and this magnetic pair-creation is very sensitive to the photon energy. In the light curve, γ-ray peaks are expected to align with the radio peaks because the emission also comes from inner region (section 3.1.2). On the other hand, if particle acceleration region is relatively far from the star such as outer gap and slot gap models, magnetic pair-creation process does not work. Especially, outgoing γ-ray photons are not significantly suffered by photon-photon collision, so that the observed cut-off shape in γ-ray is expected to fall relatively shallow (figures 19 and 22). In the outer acceleration models, γ-ray emission region is far from the radio emission region so that peaks of two wavelengths do not generally appear at the same phase in the observed light curve (figure 24).

Recently, *Fermi* has detected many γ-ray pulsars and showed that the phase-averaged and phase-resolved spectra above 200 MeV are well fitted by a power law plus exponential cut-off, and that a cut-off shape sharper than a simple exponential is rejected with high significance (e.g., [3]). Examples of γ-ray phase-averaged and phase-resolved spectra in Vela pulsar are shown in figures 25 and 26, respectively. *Fermi* also has revealed that observed

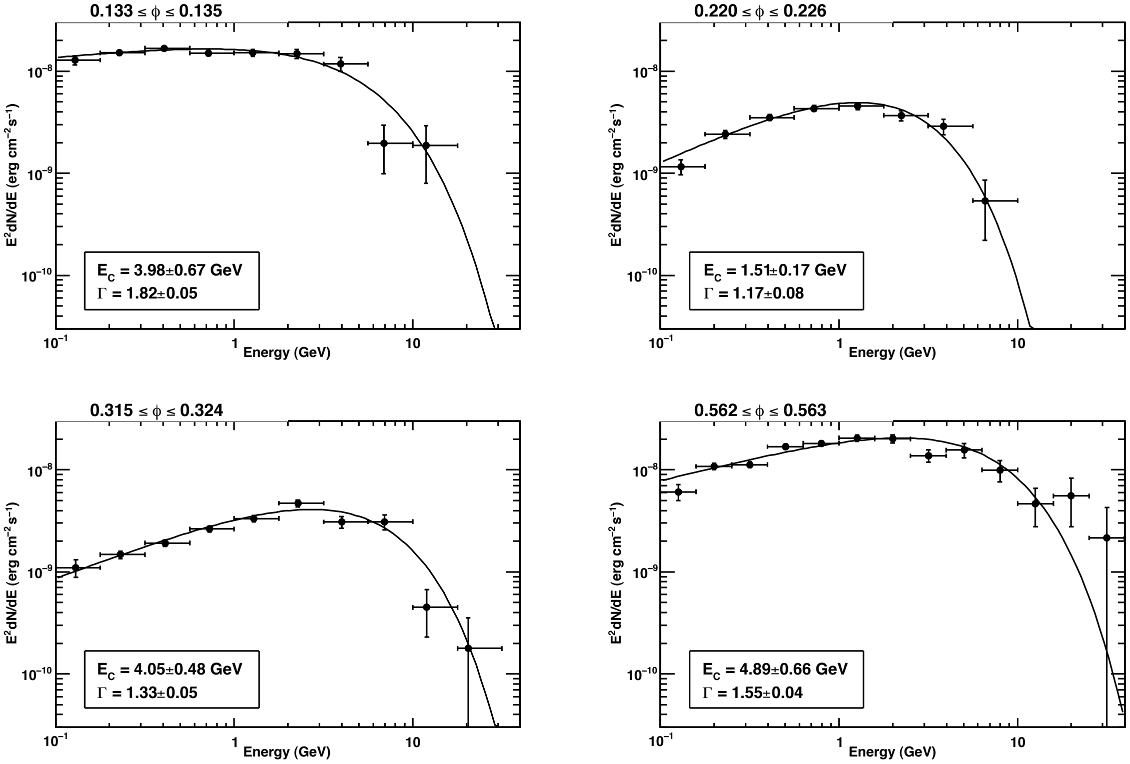

Figure 26: Spectral energy distribution in four phase intervals. The individual spectra have been exposure corrected to account for the fact that the fitting was done in a small phase bin. Figure adopted from Abdo et al. (2010b) [3].

γ-ray peaks are not aligned with the radio peaks. Furthermore, half of γ-ray pulsars cannot show radio pulsed emission [10]. Thus, the lack of hyper-exponential absorption in the spectrum, the appreciable offset from the radio peak and the presence of γ-ray pulsars without radio pulsed emission suggests that the γ-rays arise at high altitude in the magnetosphere.

3.3.5 Slot gap vs outer gap

The remaining two geometrical models can produce the general double peak profile of many γ-ray pulsars. In the outer gap model, emission starts near the null charge surface and extends toward the light cylinder. One magnetic pole dominates the emission in each hemisphere and the two peaks represent leading and trailing edges of the hollow cone of emission from this pole. If, on the other hand, emission extends well below the null charge surface toward the neutron star, both magnetic poles can contribute toward emission in a given hemisphere. This is the slot gap model. In this case, the leading image caustic from high altitudes should not be visible, and the first γ-ray pulse represents the trailing caustic from emission at below the null charge surface while the second pulse represents a trailing caustic at higher altitudes from the opposite pole. Although the appearance of leading peak should be determined by the detailed modeling of the gap, this condition highly depends on the outer boundary condition in the calculation of the electromagnetic field of the gap [111], which is theoretically uncertain so far. Dyks & Rudak (2003) [44] introduce a condition $R < 0.75R_{\mathrm{LC}}$ for emission region to avoid the appearance of the leading peak (they call "two-pole-caustic-model"). Thus, the calculated light curves are different for each model in the same combination of the geometrical parameter (α, ζ), so that the successful fit of the observed γ-ray light curve is important tool to distinguish two models.

Romani & Watters (2010) [127] compared their model with the observed γ-ray light curves. Their results suggested that the outer gap model is statistically preferred over slot gap model. An example of Geminga pulsar is shown in figure 27. However, difference in the peak phase and shape of the light curve depends on detailed distribution of the emissivity. Since their used emissivity is too simplified, their results cannot rule out the slot gap model.

Watters & Romani (2011) [168] have simulated the Galactic population of young pulsars and compared with the *Fermi* LAT sample, constraining the γ-ray pulsar models. In comparing with several γ-ray emission models, based on the vacuum dipole field structure, they found that the outer gap model is the best in almost all circumstances. This result is also consistent with the work by Takata, Wang & Cheng (2011a; 2011b; 2011c) [153, 154, 155] including millisecond pulsars. Thus, for the population as a whole there is statistically significant preference for the outer gap model. An example of the peak multiplicity is shown in figure 28. It is immediately apparent that the original two-pole-caustic-model (central bars) produces many three or four peak light curves not seen in the observed data. The gaps extending to $0.95R_{\mathrm{LC}}$ (wide right bars) make this disagreement worse. However, there are a handful of individual objects that do not fit easily into the predicted outer gap population. Such objects may well have significant lower altitude emission as posited by slot gap model. It should also be remembered that while these vacuum calculations give a clear preference for the outer gap geometries over slot gap ones, they are themselves not perfect fits and do not represent complete physical models. The real magnetosphere must include some currents and plasma that will certainly perturb the vacuum conclusion.

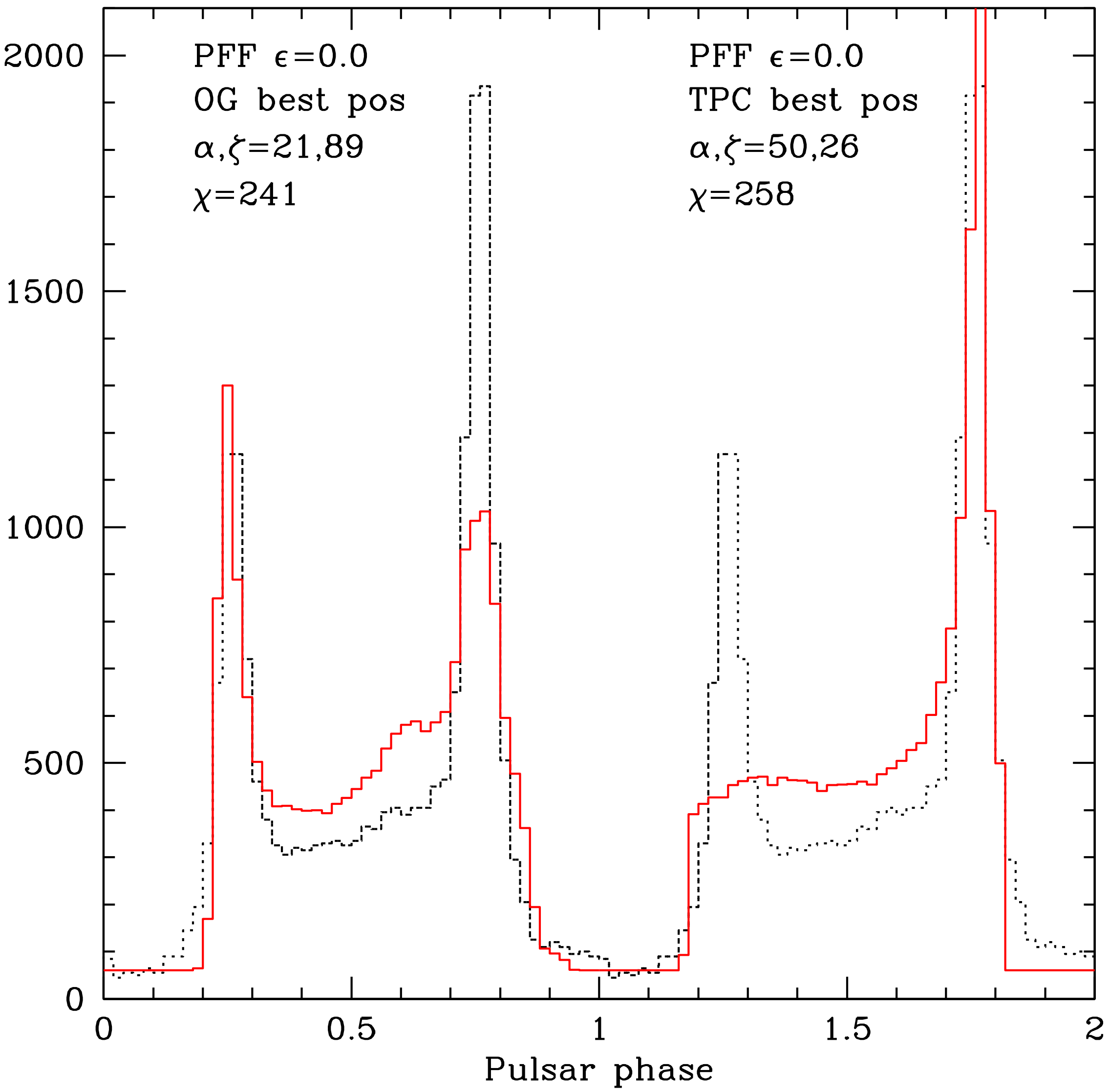

Figure 27: Light curves for two PFF models for PSR J0633+1746 (Geminga). The dotted pulse profiles show the LAT (> 100 GeV) data from Abdo et al. (2010a) [2]. The solid red lines are the calculated model light curves. The left model is for the best outer gap solution, the right model for the best slot gap solution. Figure adopted from Abdo et al. (2010b) [3].

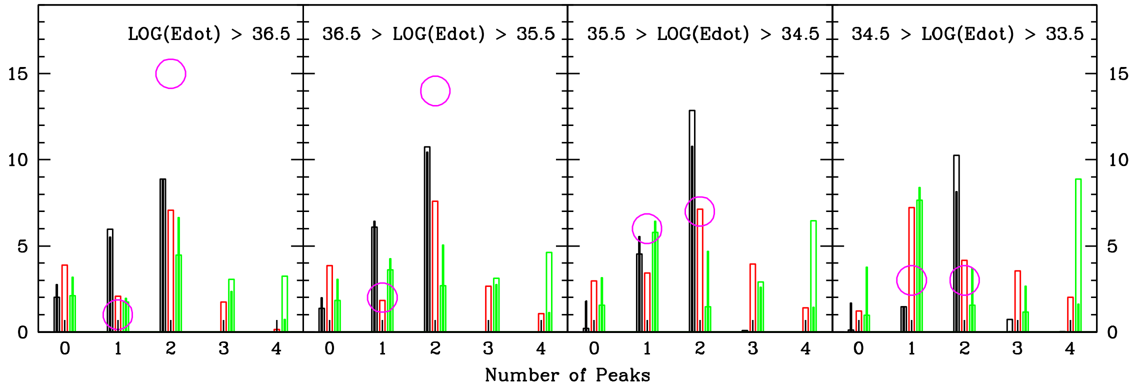

Figure 28: Peak multiplicity histograms in four different L_{sd} (denoted Edot in this figure) bins. The black bars are for the outer gap model, the red is for the Dyks and Rudak two pole caustic model, and the green is for the extended two pole caustic model. The distributtion of observed pulsars in each bin is given by the magenta circles. The thick hollow bars use a narrow Gaussian distribution of field lines around the different value of the gap width, appropriately. The thin filled bars use the full gap, stretching from the last closed field lines in to the field lines specified by the appropriate gap width value. Figure adopted from Watters & Romani (2011) [168].

3.4 Remarks to Further Model

Pulsars emit pulsed radiation over a wide range of energies from radio to γ-ray. Extremely precise periodicity and high frequency of pulsars make the magnetized neutron star interpretation undoubtable. The rotation of a magnetized neutron star creates a strong electric field that may be capable of pulling out charged particles from the surface. Thus the pulsar magnetosphere filled by the electron-positron plasmas is formed.

In numerical studies, the new efforts have been made in constructing the force-free model of pulsars. This class of models was in the past studied for the axisymmetric case only (e.g, [37]). However, recent studies show the dependence of the inclination angle on the magnetic field structure [142]. Although the inertia of particles is neglected in the model, the observational comparison becomes possible for all inclined pulsars.

On the other hand, recent observations by *Fermi* rule out the near-surface γ-ray emission proposed in polar cap cascade model [5]. Thus, pulsed γ-ray emission originates from the outer magnetosphere, as considered in the outer gap and slot gap models. The difference between two models we focus on this thesis is the location of the electromagnetic cascade process. In the outer gap model, the cascade process occurs beyond the null surface so that created particles are flowing both outward and inward directions. Although the γ-ray photons emitted by inward flowing ones are mostly absorbed, we can observe X-ray photons from these particles. In the slot gap model, the electromagnetic cascade process occurs near the star surface so that most particles are flowing out only. Therefore, in this thesis we focus on the outer gap model and investigate whether the emission by inward going particles needs to reproduce the observed multi-wavelength light curves or not.

TCS08 [152] considered a three-dimensional geometrical emission model to fit the observed light curves at different energy bands. By comparing the light curves of the Vela pulsar, they found that the X-ray emission is produced by both inward and outward emission from the gap region, and that UV/optical emission originates from secondary pairs at a higher altitude. The number of light curves of pulsars observed at γ-ray and other energy bands is increasing thanks to *Fermi*, so that it is worthwhile to investigate whether outer gap model is applicable to other sources.

4 MODEL

In this thesis, we investigate whether outer gap model can explain the observed multi-wavelength light curves of multiple γ-ray pulsars or not. The numerical method for fitting the light curve is well described by Romani & Watters (2010) [127] and Bai & Spitkovsky (2010a) [17], but we briefly summarize it in this section to explain one modification. Our model is almost the same as that used by TCS08 [152]. However, we explicitly introduce the altitude of the emission region as an additional parameter.

We assume that magnetic field structure is approximately described by a rotating dipole with magnetic moment $\mu_{\rm dip}$. The angular velocity is Ω, and the magnetic axis is declined by an angle α from the axis of rotation (the z-axis). The magnetic moment changes with time t as

$$\boldsymbol{\mu}_{\rm dip}(t) = \mu_{\rm dip}(\sin\alpha\cos\Omega t\hat{\mathbf{x}} + \sin\alpha\sin\Omega t\hat{\mathbf{y}} + \cos\alpha\hat{\mathbf{z}}). \tag{146}$$

The magnetic field produced by the rotating dipole (e.g. [68]) can be expressed using the retarded time $t_{\rm r} = t - r/c$ as

$$\mathbf{B} = -\left[\frac{\boldsymbol{\mu}_{\rm dip}(t_{\rm r})}{r^3} + \frac{\dot{\boldsymbol{\mu}}_{\rm dip}(t_{\rm r})}{cr^2} + \frac{\ddot{\boldsymbol{\mu}}_{\rm dip}(t_{\rm r})}{c^2 r}\right] + \hat{\mathbf{r}}\left[\hat{\mathbf{r}}\cdot\left(3\frac{\boldsymbol{\mu}_{\rm dip}(t_{\rm r})}{r^3} + 3\frac{\dot{\boldsymbol{\mu}}_{\rm dip}(t_{\rm r})}{cr^2} + \frac{\ddot{\boldsymbol{\mu}}_{\rm dip}(t_{\rm r})}{c^2 r}\right)\right], \tag{147}$$

where r is radial distance from the center of the star, and a dot denotes a derivative with respect to t.

We assume that radiation direction aligns with magnetic field in a frame rotating with angular velocity Ω in which the electric field vanishes. Physically, this means that the magnetosphere is filled with a co-rotation enforcing charge. The condition holds only within the light cylinder. The direction of particles in the lab frame is given by

$$\boldsymbol{\beta}_0 = \beta'_{\parallel}\hat{\mathbf{B}} + \boldsymbol{\Omega}\times\mathbf{r}/c, \tag{148}$$

where

$$\beta'_{\parallel} = -\hat{\mathbf{B}}\cdot(\boldsymbol{\Omega}\times\mathbf{r}/c) + \{[\hat{\mathbf{B}}\cdot(\boldsymbol{\Omega}\times\mathbf{r}/c)]^2 - (\boldsymbol{\Omega}\times\mathbf{r}/c)^2 + 1\}^{1/2}, \tag{149}$$

and $\hat{\mathbf{B}}$ is the unit vector along the magnetic field in lab frame. The particle velocity is highly relativistic, so we have made the approximation $|\boldsymbol{\beta}_0| \to 1$ in eq.(149). Thus the direction of radiation emitted tangential to the particle velocity vector is given by $\boldsymbol{\beta}_0$ in eq.(148). This direction is related to the periodic pulse phase. The observed phase ϕ is the sum of the azimuthal angle $\phi_{\rm em}$ at the emission point and the relativistic time delay [128]:

$$\phi = -\phi_{\rm em} - \frac{\mathbf{r}_{\rm em}\cdot\hat{\boldsymbol{\beta}}_0}{R_{\rm LC}}, \tag{150}$$

where $\mathbf{r}_{\rm em}$ is the emission point, and $R_{\rm LC}$ the light cylinder radius.

A certain mechanism is needed to fix the lower boundary of the particle acceleration region. In most works, including TCS08 [152], the lower boundary is chosen as the surface of the last-open field lines of a rotating dipole in a vacuum. The field lines are calculated by eq.(147) from the neutron star surface, and the last-open ones are defined as being just tangential to the light cylinder and they form a magnetic surface from the polar cap. The numerical procedure is described by Cheng, Ruderman & Zhang (2000) [31] in detail and we follow it. In the outer gap model, if particle acceleration occurs in an open zone, the curvature radiation from the accelerated particles forms a narrow cone along the magnetic field lines in a frame rotating with angular velocity Ω. These γ-ray photons are converted by colliding X-ray photons to $e^{\pm}$ pairs, which tend to screen the accelerating electric field. However, there is no supply of pairs on the last-open field lines and hence no screening of the electric field, since the γ-ray photons are emitted only toward higher altitudes above the last-open field lines [30]. The 'real' last-open field lines may be different from ones in a vacuum [125, 79], as we mentioned in previous section. We therefore take into account this possible deviation of the boundary. We assume that dipole magnetic field is an approximation within the light cylinder and use eq.(147) as the global magnetic field structure. Even if the overall structure is not different so much, critical value between open and closed field lines is very sensitive to the boundary value at the surface. Thus we introduce a parameter, altitude of the emission region as a correction factor in order to take into account the deviation of boundary from the vacuum field. In our model this parameter specifies the range of the emission region which is located above or below the last-open field lines within the light cylinder radius. Each different field line originating from the magnetic polar region is parameterized by magnetic colatitudes $\theta_{\rm m}$ and azimuthal angles $\phi_{\rm m}$. Following Cheng, Ruderman & Zhang (2000) [31], we define open volume coordinates on the polar cap, ($r_{\rm ov}$, $\phi_{\rm m}$), where $r_{\rm ov} \equiv \theta_{\rm m}/\theta_{\rm m}^{\rm pc,0}(\phi_{\rm m})$. The function $\theta_{\rm m}^{\rm pc,0}$ is the magnetic colatitude of the conventional polar cap angle and generally depends on the magnetic azimuth $\phi_{\rm m}$. The parameter $r_{\rm ov}$ corresponds to the altitude of the emission region: The last-open field lines of a rotating dipole in a vacuum correspond to $r_{\rm ov} = 1$, whereas those for higher altitudes have $r_{\rm ov} < 1$. Following Takata & Chang (2009) [151], the maximum value is chosen as $r_{\rm ov} = 1.36^{1/2}$, which corresponds to the polar cap angle $\theta_{\rm m}^{\rm pc} \sim 1.36^{1/2}\theta_{\rm m}^{\rm pc,0}$, obtained in the force-free limit by Contopoulos, Kazanas & Fendt (1999) [37]. We found that no significant caustics are formed in the sky map, even if the maximum value of $r_{\rm ov}$ is increased.

We assume that the radiation of different energy bands is emitted from different field lines characterized by altitude. The field line relevant to the γ- and X-rays is approximated as being the same one. The direction of the emission is tangential to the lines, and inward and outward directions are possible. Both location and direction affect the light curve profile of the energy bands. Following the model by TCS08 [152], the γ-ray radiation above 100 MeV is emitted by particles moving in an outward direction, whereas radiation at lower energy bands is emitted by those moving in both outward and inward directions. We use two conditions to constrain the emission region. First condition is the radial extension of the emission region. The outward emission is restricted to radial distances $r_{\rm n} < R_{\rm LC}$, and the inward one is restricted to $R_{\rm NS} < r < \min(3rn, R_{\rm LC})$. The outer boundary $3r_{\rm n}$ for inward emission comes from the results of dynamic model (TCS08 [152]), in which very few ingoing pairs are produced beyond the radial distance $r > 3r_{\rm n}$. Second condition is the azimuthal extension of the emission region. We use the magnetic azimuthal angle of the footprint of field line (i.e., the point where magnetic field line penetrates the neutron star surface) to characterize the field line for given $r_{\rm ov}$. Radial distance to the null charge surface on the field lines significantly depends on the magnetic azimuthal angle. In the outer gap model, most of the pairs are created around the null surface (TCS08 [152]). We expect that the gap activity is related to the distance to the null surface. Although the current density should be determined by global conditions, there is no study of the three-dimensional magnetosphere of an inclined rotator. In this paper, we assume that the field lines of both outward and inward emission are active only if the radial distance to null surface $r_{\rm n}$ is shorter than $R_{\rm LC}$. The azimuthal constraint is automatically satisfied for outward emission because the radial extension gives $r_{\rm n} < R_{\rm LC}$. However, for inward emission the condition becomes strong. The radial extension $R_{\rm NS} < r < \min(3r_{\rm n}, R_{\rm LC})$ allows for the regions $r < R_{LC}$ on the field lines with $r_{\rm n} > R_{\rm LC}$. They are not active, so that the corresponding regions should be excluded. The critical value $3r_n$ was obtained by fitting to Vela pulsar (TCS08 [152]). It may not be straightforward to apply it to other sources. The mean free path $\lambda(r)$ of the pair creation process between the γ-ray and thermal X-ray emissions from the stellar surface is estimated as $\lambda(r) \sim 5.6P^{13/21}(B_{\rm NS}/10^{12}{\rm G})^{-2/7}r$ [156]. The value at the null pointis $\lambda(r_{\rm n})$ found to be in a range of (2-3)$r_{\rm n}$ for our samples. Our light curves especially peak positions are not changed even by adopting $2r_{\rm n}$ as the outer boundary for inward emission.

Spatial distribution of the emissivity is approximated by the step function-type, but the peak positions weakly depend on the detailed emissivity distribution.

We assume that the overall structure of the light curve comes not from the emissivity distribution, but from a bunch of many field lines in the observation, that is, caustics. The appearance of caustics strongly depends on the observational viewing angle ξ and the intensity distribution. In this thesis, we focus on the peak phases of the light curve, so we adopt a simple, uniform emissivity along all magnetic field lines, which is independent of both the magnetic azimuthal angle $\phi_{\rm m}$ and the altitude $r_{\rm ov}$. The fitting does not completely reproduce the observations so, in Section 4, a simple improvement to the emissivity distribution is considered which leads to a much better fit.

We now explain our fitting method. For fixed inclination angle α and viewing angle ξ, the light curve as a function of phase ϕ depends only on the altitude $r_{\rm ov}$. The intensity is calculated in the range $r_{\rm ov} < 1.36^{1/2}$ with a bin width of 0.02. There are no significant caustics for larger $r_{\rm ov}$.

In the observed light curve, the reference phase $\phi = 0$ is assumed to be located at the radio emission peak maximum in most studies (e.g., [2]). However in the model of light curve, the conventional reference phase $\phi = 0$ occurs when the magnetic axis, spin axis and Earth line of sight lie all in the same plane. These two reference phases do not agree with each other since it is generally assumed that radio emissions arise at non-zero altitude in most empirical studies. Following Romani & Watters (2010) [127], we allow a shift of reference phase by $-0.1 \leq \delta\phi \leq 0.1$ in the model. This degree of freedom does not significantly affect the determination of the altitude parameter $r_{\rm ov}$, because we use the peak separation in the observed γ-ray and X-ray light curves which are emitted at the same $r_{\rm ov}$. For the sources showing a double-peak pulse shape in the observed γ-ray light curve, we use the peak separation. For those showing a single-peak, we use the phase separation between the γ-ray peak and one of X-ray peaks. This is the benefit of considering γ-ray and X-ray light curves simultaneously. Subsequently, we look for the altitude of the UV/optical emission region using the γ-ray upper limit of $r_{\rm ov}$.

5 RESULTS

In this section, we compare our model with pulse profiles observed at multiple wavelengths for seven pulsars. The sources are chosen using two criteria. One is that non-thermal pulses are detected in addition to the γ-ray and radio bands. Our concern is to explore whether or not the TCS08 model explains the emission region for different energy bands. The second criterion is that the geometrical parameters, α and ζ are observationally constrained by the relativistic Doppler-boosted X-ray pulsar wind nebula [112] or radio polarization data (e.g. [95]). The torus fitting method constrains the viewing angle ζ only. A small allowed range of $|\alpha - \zeta| \leq 10^\circ$ is assumed for samples in which only ζ is constrained due to the fact that radio emission from the pulsar polar region is detected. The geometrical parameters for the pulsars are listed in Table 5.2. We use these values, although there are some uncertainties in them. The results are summarized in figures 29 and 30. Figure 29 shows the intensity map for outward (upper panel) and inward (lower panel) emission as a function of the altitude of the emission region $r_{\rm ov}$ and rotational phase. The upper and lower panels in figure 30 are their pulse profiles for outward and inward emission in γ-ray and X-ray emission regions.

5.1 Vela pulsar (PSR J0835-4510)

We start with the Vela pulsar, which has been well studied to test the validity of our simple model. TCS08 [152] considered this source, but they used geometric parameters that are slightly different from ours.

Pulse profiles have been detected in optical to γ-ray bands. The observed pulse profile in γ-ray band by *Fermi* [3] shows a prominent double-peak structure and bridge emission between the two peaks. The first and second peaks are located at the phases $\phi \sim 0.13$ and $\phi \sim 0.56$, respectively, and the separation is $\Delta\phi = 0.43$. We show the intensity map for outward emission as a function of the altitude of the emission region and rotation phase in upper panel of figure 29(A). The emission altitude producing a peak separation $\Delta\phi = 0.43$ is $r_{\rm ov} \sim$ 1.05-1.06.

The X-ray data from *RXTE* [61] also shows a double-peak structure but the second peak broadens toward early phase. The calculated intensity map is shown for outward and inward emissions in the upper and lower panels of figure 29(A). The main double peaks are located at the same phases as those in the γ-ray band, so they are interpreted as being formed by outward emission. The broad component before the second peak at $\phi \sim 0.47$ is associated with the caustic formed by the inward emission, as shown in the lower panel. We attempted a fit without the inward emission, but found that the inward emission is needed in order to reproduce the observed X-ray pulse profile. The necessity of inward emission was discussed in TCS08 [152]. Thus, the peak positions of γ- and X-ray pulses can be explained with the same value of $r_{\rm ov} \sim$ 1.05-1.06. The contour map, however, shows a minor peak at $\phi \sim 0.8$ formed by the outward emission. The peak was not observed in the γ-ray band.

We compare our model with the UV data of Romani, Kargaltsev & Pavlov (2005) [126] and optical data of Gouiffes (1998) [52]. The pulse profiles in both bands are very similar, that is, they have a double-peak structure at the same phases. The peak phases however differ from those of the γ- and X-ray bands. The first peak of the UV/optical bands shifts to a later phase $\phi \sim 0.27$ and the second peak shifts to an earlier phase $\phi \sim 0.46$, so that

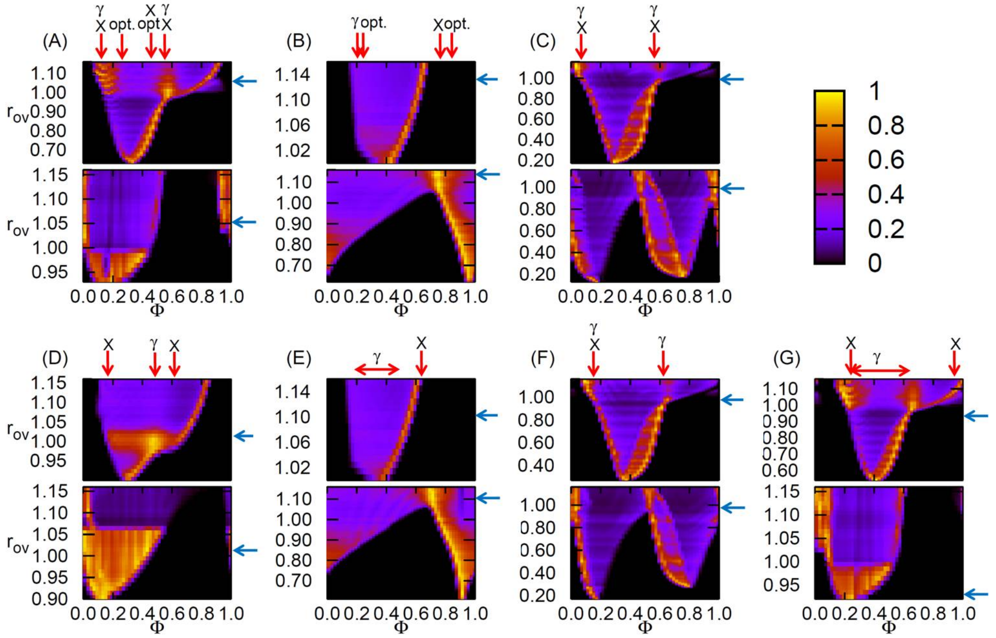

Figure 29: The intensity maps for seven pulsars. Upper left to right: PSRs J0835-4510 (A), J0659+1414 (B) and J0205+6449 (C). Lower left to right: PSRs J2229+6114 (D), J1420-6048 (E), J2021+3651 (F) and J1057-5226 (G). In each sample, upper panel is outward emission and lower is inward emission. The blue horizontal arrows show best-fit values of $r_{\rm ov}$ for γ-ray and X-ray emission regions. The red vertical arrows show the phase of peaks. The red horizontal arrows in (E) and (G) show the phase-range of broad peaks.

the peak separation becomes smaller. It can be seen from figure 29(A) that such a double-peak structure corresponds to $r_{\rm ov} \sim 0.65$-0.80 for the outward emission. The corresponding inward emission cannot be detected since its observable range is $r_{\rm ov} \geq 0.9$, as shown in the lower panel. The choice of outward emission with $r_{\rm ov} \sim 0.65$-0.80 is also supported by the fact that the second peak at $\phi \sim 0.46$ in the UV/optical ranges is sharper than the first one at $\phi \sim 0.27$, because of their different dependence on $r_{\rm ov}$. Thus, we have reproduced the pulse profiles of optical to γ-ray bands by the caustics model without any detailed assumptions about emissivity. From the fitting model, we found three conditions for the emission region. (1) The UV/optical emission region is located at an altitude above the γ- and X-ray emission region of $r_{\rm ov} \sim 1.05$-1.06. (2) There is a separation of altitude between the X-ray and optically dominant emission regions. (3) The UV/optical emission range, $\Delta r_{\rm ov} \sim 0.15$, is broader than that of γ/X-ray emission regions, $\Delta r_{\rm ov} \sim 0.02$.

5.2 PSR J0659+1414

The pulsar PSR J0659+1414 has also been observed in the γ-ray to optical bands. We use the γ-ray data from *Fermi* [173], X-ray data from *XMM-Newton* [40], UV data from Shibanov et al. (2005) [137] and optical data from Kern et al. (2003) [77]. The X-ray data is a combination of thermal (blackbody) and non-thermal (power-law) emissions and

TABLE 1 Pulsar parameters

Name (1)	$\log(L_{\rm sd})$ (erg s^{-1}) (2)	$\tau_{\rm c}$ (kyr) (3)	$\log(B_{\rm NS})$ (G) (4)	α (degrees) (5)	ζ (degrees) (6)	Reference (7)	$r_{\rm ov}$(γ-, X-ray) (8)	$r_{\rm ov}$(UV/optical) (9)	$r_{\rm n,lim}$ ($R_{\rm LC}$) (10)	$\lambda(r_{\rm n,lim})$ ($R_{\rm LC}$) (11)
J0835-4510	36.84	11	12.53	72	64	1,2	1.05-1.06	0.65-0.80	0.25	0.23
J0659+1414	34.58	110	12.67	29	38	3	1.13-1.14	0.90-1.04	0.30	0.60
J0205+6449	37.43	5	12.56	78	88	2	0.97-0.98	···	1.00	0.71
J2229+6114	37.35	11	12.31	55	46	2	1.01-1.02	···	0.40	0.29
J1420-6048	37.00	13	12.38	30	35	6,7	1.10-1.11	···	0.50	0.42
J2021+3651	36.53	17	12.50	75	85	5	0.97-0.98	···	0.40	0.40
J1057-5226	34.48	540	12.03	75	69	4	0.93-0.94	···	0.10	0.20

NOTES.-Col.(1):Pulsar name. Col.(2),(3),(4):The spindown luminosity, the characteristic age and the strength of surface magnetic field, which we adopt in Abdo et al. (2010a) [2]. Col.(5):The inclination angle. Col.(6):The viewing angle. Col.(7):Reference for cols.(5) and (6). Col.(8):The emission altitude in the γ-ray band. Col.(9):The emission altitude in the optical/UV band. Col.(10):Assumed limit of radial distance to null point. Col.(11):Mean free path for γ-ray photons at the limit of radial distance to the null point. REFERENCES.- (1)Johnston, Karastergiou & Willett (2006) [71] (2)Ng & Romani (2008) [112] (3)Everett & Weisberg (2001) [45] (4)Weltevrede & Wright (2009) [172] (5)Van Etten, Romani & Ng (2008) [161] (6)Weltevrede et al. (2010) [173] (7)Weltevrede & Johnston (2008) [171]

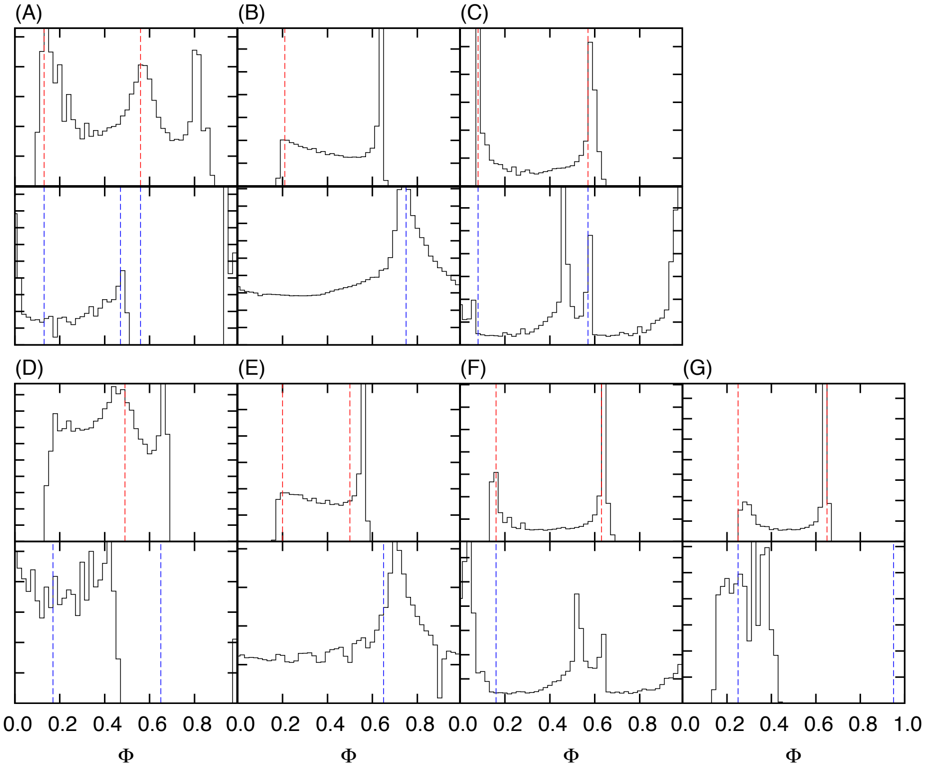

Figure 30: The calculated light curves for γ- and X-ray emission region. Upper left to right: PSRs J0835-4510 (A), J0659+1414 (B) and J0205+6449 (C). Lower left to right: PSRs J2229+6114 (D), J1420-6048 (E), J2021+3651 (F) and J1057-5226 (G). In each sample, upper panel is outward emission and lower is inward emission. The vertical axis is in arbitrary units. The red and blue short-dashed vertical lines show the phase of γ-ray and X-ray peaks as in figure 29. The peaks of PSRs J1420-6048 and J1057-5226 are so broad that the phase range is within two red vertical lines.

is consistent with a cooling middle-aged neutron star (e.g., [21]). At soft X-rays, the pulse fraction is low and the pulsations are sinusoidal, as is typical for thermal emissions from the surface of a neutron star with non-uniform temperature distribution. At higher energies (>1.5keV), where the non-thermal component dominates, the pulsed fraction increases and the profile becomes single peaked. We, therefore, consider the pulse profiles of hard X-rays (>1.5keV) only.

The pulse profile in the γ-ray band shows a relatively broad single peak, which lags the radio maximum peak by $\phi \sim 0.2$ in phase. The peak in the non-thermal X-ray pulse is at $\phi \sim$ 0.7-0.8, which is different from the phase of the γ-ray peak. This phase difference cannot be ignored, although the peaks in the γ- and X-ray data are rather broad, and hence the difference may be diminished somewhat by including the phase error. We interpret these pulse profiles as being emissions at different phases and different directions: the peak of γ-ray is formed by outward emission, whereas that of X-ray is formed by inward emission. The intensity maps are given in the upper panel (outward emission) and lower panel (inward emission) of figure 29(B), respectively. From this figure, we see that a peak separation $\Delta\phi = 0.55$ between the γ-ray and X-ray data corresponds to an emission altitude of $r_{\rm ov} \sim$ 1.13-1.14 by shifting the reference phase by $\delta\phi = 0.06$ to an earlier phase. The emission altitude cannot be fixed without the X-ray data: a shift of peak phase is allowed, so $r_{\rm ov}$ is unknown. This ambiguity is removed by considering multi-wavelength light curves. From the intensity map, we expect another very sharp caustic at $\phi \sim 0.65$, but there is no counterpart in the γ-ray observations (top panel of Fig. 4 in Weltevrede et al. (2010) [173]). We discuss this missing peak in later section. In the lower right panel of Fig. 4 in Weltevrede et al. (2010) [173], the light curve for inward emission is given. The X-ray data may be a combination of inward and outward emissions, but the X-ray profile observed by De Luca et al. (2005) [40] is similar to that of inward emission only. This means phenomenologically that outward emission of X-rays is weak in this source.

The pulse profiles in the UV [137] and optical bands [77] are almost the same shape and have a clear double-peak structure unlike the single peak in the γ- and X-ray bands. The first peak at $\phi \sim 0.02$ is later than the γ-ray peak and the second peak at $\phi \sim 0.10$ is later phase than the X-ray peak. From the upper panel of figure 29(B), we see that the observed first peak can be reproduced by outward emission at an altitude $r_{ov} < 1.10$. Here we have a weak condition because the peak position depends only weakly on $r_{\rm ov}$. For the second peak, the inward emission forms caustics for $0.90 < r_{\rm ov} < 1.04$. Thus, the altitude of the emission region in the UV/optical bands is identified as $r_{\rm ov} \sim$ 0.90-1.04, where the lower limit is set by a coarse bin of the phase in the observational data.

Kern et al. (2003) [77] have already investigated the multi-wavelength light curve of this pulsar using a similar method to ours, but could not explain the profile using geometrical parameters which are consistent with radio polarization data [45]. The reason for this is that the lower boundary of the emission region was chosen as the last-open field lines in the vacuum dipole field, that is, $r_{\rm ov} = 1.0$. In our analysis, by allowing $r_{\rm ov} \geq 1.0$, the phase of peaks can be successfully fitted by using observed geometrical parameters. This suggests that the actual lower boundary of the gap is slightly different from the last-open field lines in a vacuum dipole.

5.3 PSR J0205+6449

The γ-ray pulse profile observed by *Fermi* [6] shows a double-peak structure. The first peak is offset from the radio peak by $\phi \sim 0.08$, and the second is at $\phi \sim 0.57$. The separation is $\Delta\phi = 0.49$. The X-ray data from *RXTE* [90] are consistent with the results from *XMM-Newton* [84]. The spectral shape can be fitted by a power law such that most of the emission is non-thermal and the thermal component is constrained by the upper limit [84]. The observed X-ray pulse profile shows two peaks aligned in phase over a wide energy range of ~0.5-270 keV, and is also very similar to that of the γ-ray band.

We show the intensity maps for outward and inward emission in the upper and lower panels of figure 29(C), respectively. As seen in the upper panel, the emission altitude for the double-peak with $\Delta\phi = 0.49$ is $r_{\rm ov} \sim 0.97$-0.98. A shift of the reference phase $\delta\phi$ is not necessary in this source. As argued in TCS08 [152], outward emission dominates in the light curve for a young pulsar with a strong non-thermal X-ray component, like the Crab pulsar. PSR J0205+6449 is the youngest pulsar in our sample (characteristic age $\tau_{\rm c} \sim 5 \times 10^3$ yr) and shows rather strong non-thermal radiation in the X-ray band. Thus, it is likely that only outward omission contributes to the observed X-ray light curve in this pulsar.

5.4 PSR J2229+6114

The light curve for γ-rays observed by *Fermi* [7] shows an asymmetric single peak at $\phi \sim 0.49$. The tail extends down to $\phi \sim 0.2$. The peak position depends slightly on the energy range above 100 MeV, but the amount of shift is only ~ 0.04. The X-ray pulse profile observed by *XMM-Newton* [7] shows a double-peak structure. No peak is seen at the γ-ray peak phase. The separation between first X-ray peak and the γ-ray peak is $\Delta\phi \sim 0.32$, and the separation between the second X-ray peak and the γ-ray peak is $\Delta\phi \sim 0.14$.

The intensity map for outward emission is shown in the upper panel of figure 29(D). We consider the formation of the γ-ray peak and two X-ray peaks as being due to outward emission only. Such a solution is possible by choosing an emission altitude of $r_{\rm ov} \sim 1.01$-1.02 with a small phase shift $\delta\phi = 0.03$. The intensity map for inward emission shows a sudden decrease in the number counts for $r_{\rm ov} < 1.06$. The peak becomes broad and hence the contribution of the inward emission is not very important. We show the light curve of inward and outward emission for $r_{\rm ov} \sim 1.01$-1.02 in figure 29(D). The outward emission curve is very similar to the observations in the γ- and X-ray bands.

In this pulsar, we need to use all the light curves simultaneously in order to determine the range of $r_{\rm ov}$. Since emissions with smaller values of $r_{\rm ov}$ are not seen, if γ-ray and optical emission regions are separated $\Delta r_{\rm ov} > 0.10$, similar to the Vela pulsar and PSR J0659+1414, we predict that an optical pulse profile cannot be observed or will be only very weakly detected. This is consistent with the fact there have been no reports of the detection of a pulse in the lower energy band for this pulsar.

5.5 PSR J1420-6048

The γ-ray light curve from *Fermi* [173] shows a broad peak at $\phi \sim 0.2$-0.5. This peak may consist of two components, but it is not clear in the current photon statistics. The X-ray pulse profile from *ASCA* is detected weakly at a marginal level, and shows a broad peak at $\phi \sim 0.6$-0.7, which is different from the γ-ray peak [124, 20]. Recently, in the table of Marelli, De Luca & Caraveo (2011) [98] they list this object as non-thermal dominated source in X-ray. The pulsed X-ray profile is likely to originate from the non-thermal component.

Since the light curve of this pulsar and its geometrical parameters are similar to those of PSR J0659+1414, we adopt the same interpretation. That is, the γ-ray peak is formed by outward emission, whereas the X-ray peak is formed by inward emission. From the intensity map in figure 29(E), an emission altitude of $r_{\rm ov} \sim 1.10$-1.11 corresponds to one broad peak at $\phi \sim 0.2 - 0.5$ by outward emission and another at $\phi \sim 0.6 - 0.7$ by inward emission. Here a small shift $\delta\phi = 0.10$ toward earlier phase is used. Since there are similarities in both the γ- and X-ray light curves and the geometrical parameters between this pulsar and PSR J0659+1414, we expect a similar double-peak pulse profile in the optical band, if it is detected.

5.6 PSR J2021+3651

Observations in the γ-ray band have been obtained by *Fermi* [8] and *AGILE* [58]. The observed light curve shows a sharp double-peak structure. The first peak is offset from the radio peak by $\phi \sim 0.16$ and the two peaks are separated by $\Delta\phi \sim 0.47$. The X-ray light curve in Abdo et al. (2009d) [8] shows a relatively sharp peak associated with first peak in the γ-ray light curve albeit with weak photon statistics. Here, we assume that at least the first peak is non-thermal in origin. The possible contribution of non-thermal X-ray emissions is also discussed in Hessels et al. (2004) [64] and Van Etten, Romani & Ng (2008) [161]. We expect that this assumption will be tested by phase-resolved spectra from future observations.

As seen in the upper panel of Fig. 29(F), the emission altitude is $r_{\rm ov} \sim 0.97$-0.98, for which there is a γ-ray double-peak profile with separation $\Delta\phi = 0.47$ and a relative shift $\delta\phi = 0.06$ toward later phase. The peak of non-thermal emission at $\phi = 0.15$-0.20 in the X-ray light curve is found to be formed by outward emission only. The relatively weak second peak in the X-ray band is consistent with the case of PSR J0205+6449. Thus, the three model parameters for this pulsar and PSR J0205+6449 are very similar, as shown in Table 5.2.

5.7 PSR J1057-5226

The γ-ray light curve from *Fermi* [4] shows a broad peak at $\phi \sim 0.25$-0.65. This probably consists of two components, but it is not clear. De Luca et al. (2005) [40] extract only a power-law component of the X-ray light curve and their figure 13 shows a two peaks at $\phi \sim 0.2$-0.3 and $\phi \sim 0.9$-1.0, although the data are very coarse. We regard the light curve as being produced by a non-thermal X-ray component.

The observed light curve may be regarded either as a broad peak consisting of weak peaks and a relatively bright bridge emission or as a result of the range of the emission region widening towards lower altitudes. In the latter interpretation the fitted $r_{\rm ov}$ is only a lower limit. We thus focus on the width of the γ-ray peak. From the upper panel of figure 29(G), the emission altitude is $r_{\rm ov} \sim 0.93$-0.94 Even if we assume a double-peak structure with the first peak at $\phi \sim 0.31$ and the second peak at $\phi \sim 0.59$ following Abdo et al. (2010c) [4], we have $r_{\rm ov}$ ~0.90-0.91, which is very similar to the value obtained above. Thus we have $r_{\rm ov}$ ~0.90-0.95 in either case. The phase shift is $\delta\phi = 0.10$ in this pulsar. The first peak in the X-ray light curve is formed by outward emission, but the second one cannot be produced for the same altitude. This may be a drawback to our model, but the present X-ray data are coarse and a much more precise non-thermal X-ray light curve is needed.

6 DISCUSSIONS

6.1 Statistical Properties of the Emission Region

In the previous section, we have shown that the peak phases of seven pulsars emitting γ- and X-rays can be successfully fitted using the TCS08 [152] outer gap model, in which both γ-rays and X-rays originate from the same magnetic field line characterized by an altitude $r_{\rm ov}$. The parameter $r_{\rm ov} > 1$ is needed in the light curve fitting for some sources. Moreover, the inclusion of inward emission for X-rays causes a variety of pulse profiles in both bands. The parameter $r_{\rm ov}$ could not be determined solely using γ-ray data for a single γ-ray peak pulsar. But, by considering the X-ray light curve, the parameter is uniquely determined for PSRs J0659+1414, J2229+6114 and J1420-6048.

It is worthwhile to explore the general dependence of the altitude $r_{\rm ov}$ on other characteristics if any, although there may not be enough data for a proper statistical analysis. In figure 31, $r_{\rm ov}$ is plotted as a function of inclination angle α, spin-down luminosity $L_{\rm sd}$, characteristic age $\tau_{\rm c}$ and surface dipole magnetic field $B_{\rm NS}$. We found that there is a significant correlation between $r_{\rm ov}$ and the inclination angle α only; the relations of $r_{\rm ov}$ with the other parameters are very weak. This correlation suggests that the deviation from a vacuum rotating dipole field is large for small inclination angle. It is very interesting to compare this result with that in a force-free magnetosphere. Bai & Spotkovsky (2010b) [18] proposed that the separatrix layer at an altitude of 0.90-0.95 times the height of the last-open field line is relevant to emissions in a three-dimensional inclined force-free magnetosphere. This altitude, which is not exactly symmetric with respect to the magnetic azimuthal angle $\phi_{\rm m}$, but can be approximated by the value at $\phi_{\rm m} = 0$, is plotted in figure 31 as purple downward and blue upward triangles. Two linear fitting lines are also shown. The altitude $r_{\rm ov}$ decreases with the inclination angle α in both our model and the separatrix layer model of a force-free magnetosphere. However, the emission region in the separatrix layer model extends even outside the light-cylinder, whereas ours is well localized around null points. Accounting for this difference may be important for further improvement of the model of the emission region based on a force-free magnetosphere.

The thickness of the gap region, w, is not known, but it is sometimes assumed to decrease with the spin-down luminosity $L_{\rm sd}$ [169, 127]. We have $w = 1 - r_{\rm ov}$, if the lower boundary of the gap is fixed as the last-open field line in the vacuum dipole field. This assumption is tested in the lower left panel of figure 31, in which the relation $(1 - r_{\rm ov}) \approx (L_{\rm sd}/10^{33}{\rm erg\ s^{-1}})^{-1/2}$ is plotted as a light green curve. (The curve is not fitted to the data points.) This suggests that the assumption of maximum altitude, $r_{\rm ov} = 1.0$, is not a good one. This discovery affects expected number of the γ-ray pulsars in the observation. From geometrical reason, the pulsed emission by caustics is limited to a certain range between inclination and viewing angles.

Romani & Watters (2010) [127] showed the range of observable pulsars with $r_{\rm ov}$ =0.95, 0.90 and 0.70 for outer gap model in their Fig.16. We recalculate it and show the result in figure 32. The observable range of viewing angle ζ is below the curves. Our finding in figure 31 is that $r_{\rm ov}$ is a function of the inclination angle, which is similar to that of the separatrix layer model. We also show the observable range by the empirical relation obtained in figure 31 as black solid line, for which the altitude is chosen as 0.925 times the

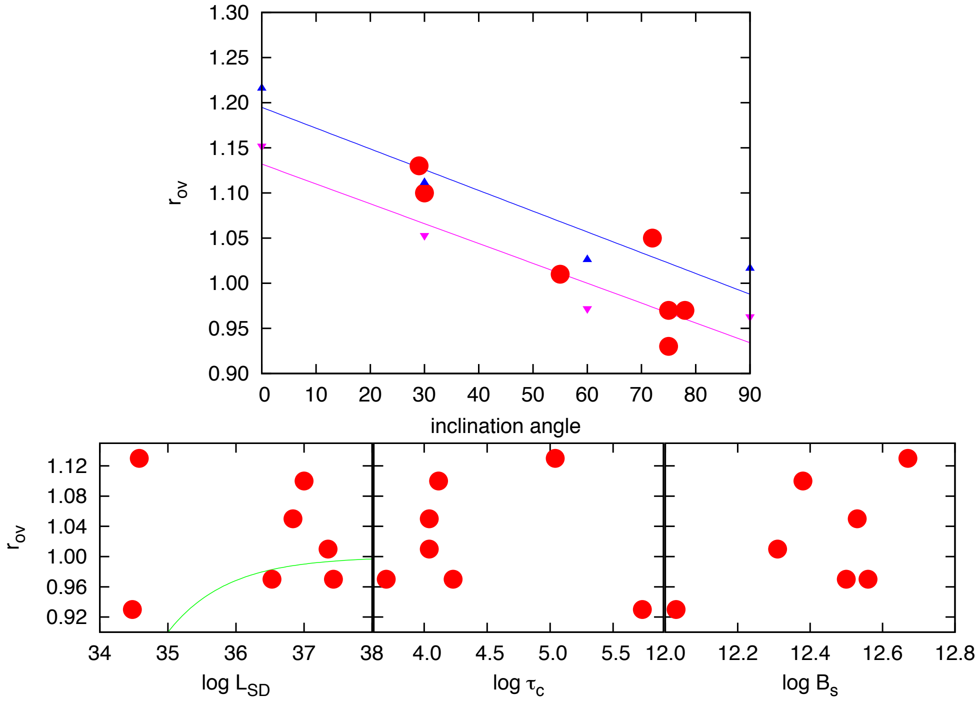

Figure 31: The relation between $r_{\rm ov}$ and inclination angle (upper), spin-down luminosity (lower left), characteristic age (lower middle) and surface magnetic field (lower right). The altitudes corresponding to the separatrix layer model are shown as purple downward and blue upward triangles in the upper panel. The two lines are linear fitting lines for the separatrix layer model. The light green curve in the lower left panel shows the relation $(1 - r_{\rm ov}) = (10^{33}{\rm erg\ s^{-1}}/L_{\rm sd})^{1/2}$.

height of the last-open field line in force-free magnetosphere. The figure shows that sources with low inclination and viewing angles become observable. For example, pulsar with the inclination angle $\alpha = 30°$ can be detected for $\zeta > 60°$ for $r_{\rm ov}$ =0.95, but for $\zeta > 30°$. Thus expected number increases approximately twice for sources with the low inclination and viewing angles.

Note that we also investigate the effect to the cut-off energy of γ ray spectrum using the obtained $r_{\rm ov}$-α relation. We describe it in Appendix A.

6.2 The Phenomenological Limitation for Emissivity

The caustic model which considered in this thesis provides peak positions consistent with observation, but there are also some additional, unseen peaks. These are interpreted as being prohibited by some mechanism. In this section, we consider an improvement to our model that takes into account a very simple distribution for the emissivity. Detectable γ-rays are radiated with large multiplicity by the pair plasma in the gap region. Therefore, the mean free path of a γ-ray photon should be less than light cylinder radius [150]. The pair creation

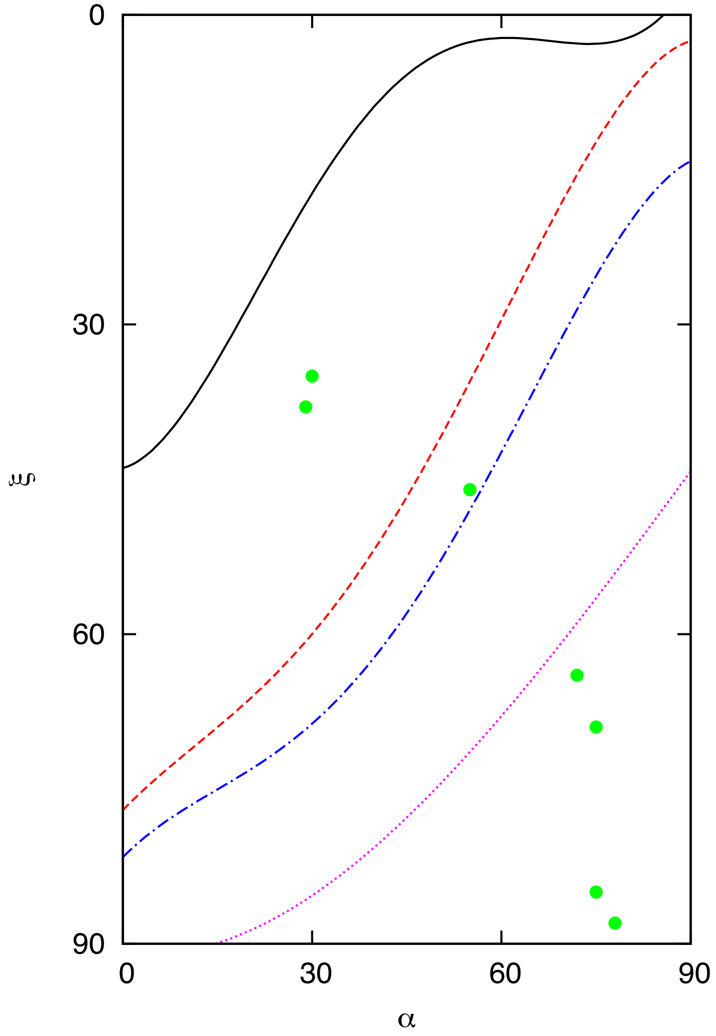

Figure 32: The observable range for γ-ray pulsars in the α-ζ plane for the outer gap model. Black solid curve shows the boundary of observable pulsars using linear fitting line for the separatrix layer model. Red dashed, blue dash-dotted and purple dotted curves show the boundary with $r_{\rm ov}$ =0.95, 0.90 and 0.70, respectively. Light-green curcles show the pulsars in Table 5.2.

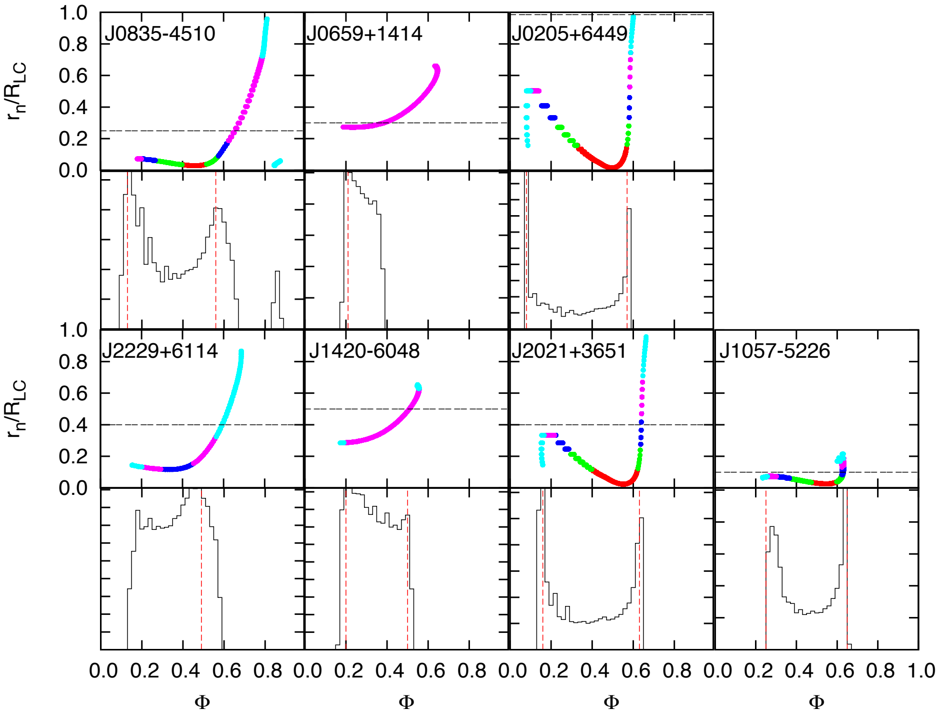

Figure 33: The distribution of the radial distance to the null point of the field line on which observed photons are emitted (each upper panel) and the light curves that are restricted by the azimuthal extension limit as a function of the rotation phase (each lower panel) for seven pulsars. The color shows the radial distance to the emitting point as $0.0 < r/R_{\rm LC} < 0.2$ (red), $0.2 < r/R_{\rm LC} < 0.4$ (light green), $0.4 < r/R_{\rm LC} < 0.6$ (blue), $0.6 < r/R_{\rm LC} < 0.8$ (purple), $0.8 < r/R_{\rm LC} < 1.0$ (light blue). The values $r_{\rm n,lim}$ for each pulsar are shown as black long-dashed horizontal lines. The red short-dashed vertical lines show the phases of the γ-ray peaks. For PSRs J1420-6048 and J1057-5226, the vertical lines show the phase range of broad peaks.

mean free path is given by $\lambda(r) \sim 5.6P^{13/21}(B_{\rm NS}/10^{12}{\rm G})^{-2/7}r$ [156] for an assumed limiting distance to the null point $r_{\rm n,lim}$. The position of the null point of inclined pulsars, where the accelerating electric field arises, depends significantly on magnetic azimuthal angle, so the intensity of γ-ray emission also depends on the magnetic azimuthal angle. Therefore, active field lines should be limited in the azimuthal direction. By taking into account the azimuthal extensions with $\lambda(r_{\rm n,lim}) \lesssim 0.2-0.7R_{\rm LC}$ listed in table 5.2, the fits of the resultant light curves, which are shown in figure 33, become better. In the same figure, we also show the radial distance to the emission points of the observed photons against the rotation phase. Note that, for the Vela pulsar, the minor third peak at $\phi \sim 0.8$ still remains even after the inclusion of the azimuthal extension limit. The corresponding radial distance of emission points is relatively large, so that the photon energy is expected to be soft. The third peak is not observed in the GeV band, but may appear in a much lower energy band. At least, the minor third peak of the X-ray light curve appears to be associated with the same caustic.

We have also tried to improve the X-ray light curve with some other simple assumptions, but have not had good results. The reason for this is that there are many ways for X-ray emitting particles to be created: via thermal, magnetospheric emissions and magnetic pair creation. Therefore, the three-dimensional effect of the propagation of γ-ray photons and soft X-ray photons is very important. Without it we cannot successfully explain the light curve.

6.3 The Location of the UV/Optical Emission Region

We explored the UV/optical emission region for Vela and PSR J0659+1414. The results are qualitatively similar: the altitude range of UV/optical emission, $\Delta r_{\rm ov} \sim 0.15$, is broader than that for γ- and X-rays, $\Delta r_{\rm ov} \sim 0.02$; and both emission regions are not continuous and connected, but are widely separated. The separation may come from two competing mechanisms: a decrease of emissivity and an increase of synchrotron intensity in the UV/optical bands with altitude.

As discussed in TCS08 [152], the outward emission is generally dominant in UV/optical emission, as shown in their Fig. 4. The explanation is the following. The number of created pairs is the main cause of the difference between inward and outward emissions in the UV/optical bands, since the collision angles with magnetospheric X-rays are not different for outgoing and ingoing γ-ray photons in the acceleration region. More outgoing γ-rays are emitted, and hence more outgoing secondary pairs are produced. Thus, the synchrotron emission for outgoing secondary pairs produced by magnetic X-rays is brighter than that for the ingoing secondary pairs. The observed flux strongly depends on the geometrical configuration. The outward emission in the UV/optical bands may not point toward us even though the intrinsic emission is strong. Our results show that the peaks in the Vela pulsar can be explained by outward emission alone, while those in PSR J0659+1414 require both inward and outward emissions. Our result suggests that outward emission is significantly suppressed in PSR J0659+1414, to the level of the intrinsically weak inward emissions. The stronger component is hidden, because the observable altitude range is narrow, as shown in figure 29(B). This may explain the fact that UV/optical flux is smaller than the value extrapolated from non-thermal X-rays, as seen Fig. 4 of Mignani et al. (2010) [107], whereas the flux coincides with the extrapolation in the Vela pulsar. This interpretation may be tested in PSR J1057-5226. We also suggest that this difference is the reason why PSR J0659+1414, which has similar geometrical parameters to the Vela pulsar, has an observable optical spectrum [105], and the flux is slightly smaller than the extrapolation from non-thermal X-ray emission. The pulse profile has not yet been determined, but the peaks should appear at a phase $0.3< \phi < 0.6$ and be due to outward emission.

7 CONCLUSIONS

We have calculated the light curves of the emissions using the TCS08 [152] outer gap model and compared them with observed multi-wavelength light curves. We find that the model can successfully explain the peak positions of multi-wavelength light curves. In order to determine the altitude of the emission region, the observed X-ray light curve is important, especially when there is a single peak in the γ-ray light curve. If inward emissions are absent, the observed light curves for 70% of our samples cannot reproduce in our model. Therefore, we conclude that the current slot gap model should rule out unless using very fine turned emissivity distribution.

The fit of a light curve based on a simple emissivity distribution can be improved by taking into account the limitation of azimuthal extension in which a reasonable value of the γ-ray mean-free-path is adopted. The resulting difference between model and observed γ-ray light curves becomes small; however, there may still be an unseen peak, such as the minor third peak in Vela.

The best-fit values of the altitude of the emission region for PSRs J0659+1414 and J1420-6048, suggest a deviation from the last-open field lines of a vacuum dipole field. The real last-open field lines lie inside those of vacuum dipole field, $r_{\rm ov} < 1.0$. This shift suggests that the lower boundary is very similar to that of a force-free magnetosphere. We find that the altitude of the emission region is correlated with inclination angle. This relationship is also very similar to that in a force-free magnetosphere. The lower boundary of emission region has been assumed to $r_{\rm ov} = 1$ so far, but our model fits do not support it. This modification of the boundary of the magnetosphere suggests that the pulsars with low inclination and viewing angles are likely to be detectable. Thus the expected number in the future observation considered in the works [153, 168] is underestimated for the sources with low inclination and viewing angles.

The X-ray follow-up observations for γ-ray pulsars are now proceeding [98], so that we expect that the samples satisfied with selection criteria of our analysis will increase in the near future. Our model and underlying magnetosphere model will be proved or disproved definitly.

Appendix

A The effect to the cut-off energy

The $r_{\rm ov}$-α relation in figure 31 means that pulsars with the small inclination angle have the large polar cap radius relative to the vacuum dipole. This relation also affects the radial distance to the null charge surface. In the vacuum dipole, the radial distance to the null charge surface is larger for pulsars with smaller inclination angle. Since the observed cut-off energies reflect the strength of the accelerating electric field at the emission point, the softer cut-off energy is expected for the pulsars with smaller inclination and/or viewing angles. However, the relation means that the radial distance to the null charge surface is smaller than that of vacuum dipole for the pulsars with small inclination angle. Therefore, the cut-off energy would be harder than that of the vacuum case and less sensitive to the inclination and viewing angles.

In order to calculate the γ-ray spectrum including the above effects, we adopt the two-layer outer gap model proposed by Wang, Takata & Cheng (2010, 2011) [166, 167]. They argued that the outer gap should be approximately divided into two layers, i.e. the main acceleration region starting from the last-open field lines and the screening region lying in the upper part of the gap. In the main acceleration region, the charge density is ~ 10 % of the GJ value and a strong electric field accelerates electrons and positrons up to a Lorentz factor of $\gamma \sim 10^{7.5}$. The accelerated particles emit several GeV photons via the curvature radiation process. In the screening region, the large number of pairs created there starts to screen out the gap electric field. The curvature radiation from the screening pairs mainly produces $\sim$100 MeV photons.

Here we denote $x_{\rm fl}$, $z_{\rm fl}$ and $\phi_{\rm fl}$ as the coordinates along the magnetic field line, perpendicular to the magnetic field line in the poloidal plane and in the magnetic azimuth, respectively. We expect that the particle number density increases exponentially near the boundary ($z_{\rm fl} = h_{\rm fl,1}$) between the main acceleration and screening regions [29, 30], and that the charge density is almost constant in the screening region [66]. Hence, Wang, Takata & Cheng (2010, 2011) [166, 167] approximately described the distribution of the charge density in the $z_{\rm fl}$-direction with the step function as follows:

$$\rho(\mathbf{r}) = \begin{cases} \rho_1(x_{\rm fl}, \phi_{\rm fl}), & 0 \le z_{\rm fl} \le h_{\rm fl,1}(x_{\rm fl}, \phi_{\rm fl}), \\ \rho_2(x_{\rm fl}, \phi_{\rm fl}), & h_{\rm fl,1} \le z_{\rm fl} \le h_{\rm fl,2}(x_{\rm fl}, \phi_{\rm fl}), \end{cases} \tag{151}$$

where, $|\rho_1| < |\rho_{\rm GJ}| < |\rho_2|$, $z_{\rm fl} = 0$, $z_{\rm fl} = h_{\rm fl,2}$ correspond to the last-open field line and the upper boundary of the gap. For simplicity, we define the boundary $h_{\rm fl,1}$ between main acceleration region and the screening region by approximating that $h_{\rm fl,1}/h_{\rm fl,2}$ is constant along the magnetic field line. The model predicts that the charge density in the screening region should be proportional to the GJ charge density [166]. This situation will be satisfied because there are many pairs created by the GJ values, its distribution along the magnetic field line is not important for the electric field distribution. Therefore, we approximate that $\rho - \rho_{\rm GJ} \sim g(z_{\rm fl}, \phi_{\rm fl})\rho_{\rm GJ}(\mathbf{r})$ for both main acceleration and screening regions, where

$$g(z_{\rm fl}, \phi_{\rm fl}) = \begin{cases} -g_1(\phi_{\rm fl}), & 0 \le z_{\rm fl} \le h_{\rm fl,1}(x_{\rm fl}, \phi_{\rm fl}), \\ g_2(\phi_{\rm fl}), & h_{\rm fl,1}(x_{\rm fl}, \phi_{\rm fl}) < z_{\rm fl} \le h_{\rm fl,2}(x_{\rm fl}, \phi_{\rm fl}). \end{cases} \tag{152}$$

We assume that $g_1 > 0$ and $g_2 > 0$ so that $|\rho| < |\rho_{\rm GJ}|$ for the main acceleration region and $|\rho| > |\rho_{\rm GJ}|$ for the screening region.

To obtain the typical strength of the electric field in the gap, we find the solution of the Poisson equation for each azimuthal angle:

$$\frac{\partial^2}{\partial z_{\rm fl}^2}\phi'(x_{\rm fl}, z_{\rm fl}, \phi_{\rm fl})|_{\phi_{\rm fl}={\rm fixed}} = -4\pi[\rho(x_{\rm fl}, z_{\rm fl}, \phi_{\rm fl}) - \rho_{\rm GJ}(\mathbf{r})]_{\phi_{\rm fl}={\rm fixed}}, \tag{153}$$

where ϕ' is the electric potential of the accelerating field. Here we assume that the derivative of the potential field in the $z_{\rm fl}$-direction is much larger than that in the $x_{\rm fl}$-direction and the $\phi_{\rm fl}$-direction.

In this case, we neglect the $z_{\rm lf}$-dependence of the GJ charge density and approximate as $\rho_{\rm GJ}(x_{,\rm fl}, \phi_{\rm fl}) \sim -\Omega B x_{\rm fl}/2\pi c R_{\rm cur}$ [29, 30]. The conditions on the lower ($z_{\rm fl} = 0$) and upper ($z_{\rm fl} = h_{\rm fl,2}$) boundaries are given by

$$\phi'(x_{\rm fl}, z_{\rm fl} = 0, \phi_{\rm fl}) = 0 \text{ and } \phi'(x_{\rm fl}, z_{\rm fl} = h_{\rm fl,2}, \phi_{\rm fl}) = 0 \tag{154}$$

respectively. Imposing the condition that ϕ' and $\partial\phi'/\partial z_{\rm fl}$ are continuous at the boundary $z_{\rm fl} = h_{\rm fl,1}$, we obtain the solution as

$$\phi'(\mathbf{r}) = -\frac{\Omega B x_{\rm fl} h_{\rm fl,2}^2(x_{\rm fl}, \phi_{\rm fl})}{c R_{\rm cur}} \begin{cases} -g_1(\phi_{\rm fl}) z_{\rm fl}'^2 + C_{\rm g} z_{\rm fl}', & 0 \le z_{\rm fl}' \le h_{\rm fl,1}/h_{\rm fl,2}, \\ g_2(\phi_{\rm fl})(z_{\rm fl}'^2 - 1) + D_{\rm g}(z_{\rm fl}' - 1), & h_{\rm fl,1}/h_{\rm fl,2} < z_{\rm fl}' \le 1, \end{cases} \tag{155}$$

where

$$C_{\rm g}(x_{\rm fl}, \phi_{\rm fl}) = -\frac{g_1 h_{\rm fl,1}(h_{\rm fl,1} - 2h_{\rm fl,2}) + g_2(h_{\rm fl,1} - h_{\rm fl,2})^2}{h_{\rm fl,2}^2}, \tag{156}$$

$$D_{\rm g} = -\frac{g_1 h_{\rm fl,1}^2 + g_2 h_{\rm fl,2}^2}{h_{\rm fl,2}^2} \tag{157}$$

and $z_{\rm fl}' \equiv z_{\rm fl}/h_{\rm fl,2}(x_{\rm fl}, \phi_{\rm fl})$. The accelerating electric field, $E_\parallel = -\partial\phi'/\partial x_{\rm fl}$, is written as

$$E_\parallel(\mathbf{r}) \sim \frac{\Omega B h_{\rm fl,2}^2(x_{\rm fl}, \phi_{\rm fl})}{c R_{\rm cur}} \begin{cases} -g_1(\phi_{\rm fl}) z_{\rm fl}'^2 + C_{\rm g}(\mathbf{r}) z_{\rm fl}', & 0 \le z_{\rm fl}' \le h_{\rm fl,1}/h_{\rm fl,2}, \\ g_2(\phi_{\rm fl})(z_{\rm fl}'^2 - 1) + D_{\rm g}(\mathbf{r})(z_{\rm fl}' - 1), & h_{\rm fl,1}/h_{\rm fl,2} < z_{\rm fl}' \le 1, \end{cases} \tag{158}$$

where we used the dipole-field relations $\partial(B h_{\rm fl,2}^2)/\partial x_{\rm fl} \sim 0$, $\partial z_{\rm fl}'/\partial x_{\rm fl} = \partial(z_{\rm fl}/h_{\rm fl,2})/\partial x_{\rm fl} \sim 0$, $\partial(h_{\rm fl,1}/h_{\rm fl,2})/\partial x_{\rm fl} \sim 0$ and approximated that $\partial R_{\rm cur}/\partial x_{\rm fl} \sim 0$.

On the upper boundary, we anticipate that the total potential field (corotational potential + non-corotational potential) in the gap is continuously connected to the corotational potential field outside the gap. This screening condition is described by

$$\frac{\partial\phi'}{\partial z_{\rm fl}}|_{z_{\rm fl}=h_{\rm fl,2}} = -E_\perp(x_{\rm fl}, z_{\rm fl} = h_{\rm fl,2}, \phi_{\rm fl}) = 0. \tag{159}$$

This condition gives the relation between ($h_{\rm fl,1}$, $h_{\rm fl,2}$) and (g_1, g_2) as

$$\left(\frac{h_{\rm fl,2}}{h_{\rm fl,1}}\right)^2 = 1 + \frac{g_1}{g_2}. \tag{160}$$

Here we do not consider the azimuthal distribution of the dimensionless charge density g_1 and g_2, because we discuss the general properties of the γ-ray emission.

The typical Lorentz factor of the accelerated particles can be estimated by force balance between the electric field and the radiation drag force as

$$\gamma = \left(\frac{3R_{\rm cur}^2}{2e}E_{\parallel}\right)^{1/4}. \tag{161}$$

The spectrum of the curvature radiation emitted by the individual particle is written as eq.(11). A γ-ray spectrum measured by the observer may be expressed by (e.g., [67])

$$\frac{dF_\gamma}{dE_\gamma} \sim \frac{1}{d}\sum_{\mathbf{r}_i} N_{\rm p}(\mathbf{r}_i)F_{{\rm cur},\omega}(E_\gamma,\mathbf{r_i})R_{\rm cur}(\mathbf{r}_i)\Delta A_i, \tag{162}$$

where $N_{\rm p} \sim |\rho|/e$ is the particle number density, $\mathbf{r}_i$ represents the radius of the emission point and ΔA_i is the emission area. The integrated energy flux between 100 MeV and 300 GeV can be calculated from

$$F_{\gamma,100} = \int_{100{\rm MeV}}^{300{\rm GeV}} \frac{dF_\gamma}{dE_\gamma}dE_\gamma. \tag{163}$$

We define the fractional gap thickness measured on the stellar surface as

$$f \equiv \frac{h_{{\rm fl},2}(R_{\rm NS},\phi_{\rm fl})}{r_{\rm pc}(\phi_{\rm fl})}. \tag{164}$$

Note that $E_{\parallel} \propto f^2$, because the electric field $E_{\parallel}$ is proportional to $Bh_{{\rm fl},2}^2$.

Zhang & Cheng (1997, 2003) [174, 175] suggested a self-consistent outer gap model controlled by the photon-photon pair-creation process between curvature photons and X-rays from the stellar surface. They estimated the gap fraction as

$$f = \frac{h_{{\rm fl},2}(R_{\rm NS},\phi_{\rm fl}}{r_{\rm pc}(\phi_{\rm fl})} \sim \frac{D_{\perp}(R_{\rm LC})}{R_{\rm LC}} = 5.5\left(\frac{P}{1{\rm s}}\right)^{26/21}\left(\frac{B_{\rm NS}}{10^{12}{\rm G}}\right)^{-4/7}. \tag{165}$$

We note that Zhang & Cheng (1997, 2003) [174, 175] estimated the gap fraction by a completely vacuum electric field $E_{\parallel} = \Omega Bf^2R_{\rm LC}^2/cR_{\rm cur}$. With the same gap fraction, the solution described by eq.(158) gives an electric field at least a factor of four smaller than that used in Zhang & Cheng (1997, 2003) [174, 175]. This difference can be important for the typical energy of curvature radiation, because $E_{\rm cur} \propto E_{\parallel}^{3/4}$. In other words, if we derive the gap fraction from the pair-creation condition that $E_{\rm X}E_\gamma = (m_{\rm e}c^2)^2$, where $E_{\rm X}$ is the X-ray photon energy, the model [155] predicts a fractional gap thickness larger than that of Zhang & Cheng (1997, 2003) [174, 175]. Here, reducing the electric field in the model of Zhang & Cheng (1997, 2003) [174, 175] by a factor of four, we find that the gap fraction is increased by a factor of $4^{3/7} \sim 1.8$ from the values in eq.(165).

The results are shown in figure 34. Following Takata, Wang & Cheng (2011c) [155], we choose the values of the model parameters, $h_{{\rm fl},1}/h_{{\rm fl},2} = 0.95$, $1 - g_1 = 0.3$, $B_{\rm NS} = 3 \times 10^{12}$ G and $f = 0.1$. The black lines show the results in the case of $r_{\rm ov} = 1.0$ and the red lines show the results with the $r_{\rm ov}$-α relation. We can see that in the case of using the $r_{\rm ov}$-α relation, the cut-off energy does not depend on the geometrical parameters. This is consistent with the *Fermi* observations that observed range of the cut-off energy is small [2].

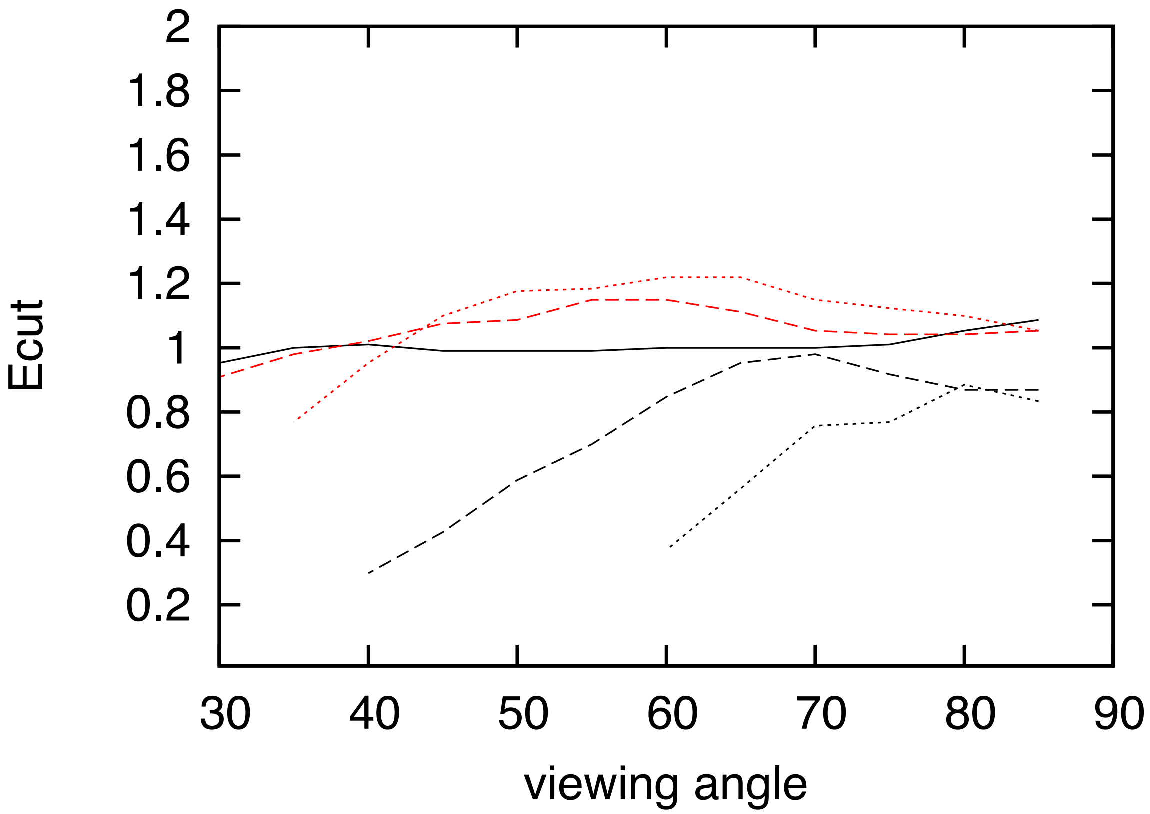

Figure 34: Dependence of spectral cut-off energy of the viewing geometry. The vertical line represents the cut-off energy in the arbitrary unit.

References

[1] Abdo, A. A., et al. 2011a, arXiv:1108.1435

[2] Abdo, A. A., et al. 2010a, ApJS, 187, 460

[3] Abdo, A. A., et al. 2010b, ApJ, 713, 154

[4] Abdo, A. A., et al. 2010c, ApJ, 720, 26

[5] Abdo, A. A., et al. 2009a, ApJ, 696, 1084

[6] Abdo, A. A., et al. 2009b, ApJ, 699, L102

[7] Abdo, A. A., et al. 2009c, ApJ, 706, 1331

[8] Abdo, A. A., et al. 2009d, ApJ, 700, 1059

[9] Abdo, A. A., et al. 2009f, Science, 325, 840

[10] Abdo, A. A., et al. 2008, Science, 322, 1218

[11] Aleksić, J., et al. 2011a, ApJ, 742, 43

[12] Aleksić, J., et al. 2011b, arXiv:1109.6124

[13] Aliu, E., et al. 2011, Science, 334, 69

[14] Arons, J. 1983, ApJ, 266, 215

[15] Arons, J., & Scharlemann, E. T. 1979, ApJ, 231, 854

[16] Baade, W., & Zwicky F. 1934 Proc. NAt. Acad. Sci. 20, 254

[17] Bai, X.-N., & Spitkovsky, A. 2010a, ApJ, 715, 1270

[18] Bai, X.-N., & Spitkovsky, A. 2010b, ApJ, 715, 1282

[19] Bailes, M., et al. 1997, ApJ, 481, 386

[20] Becker, W. 2009, in Becker W., ed., Astrophys. Space Sci. Libr. Vol. 357, Neutron stars and pulsars. Springer, Berlin, p.131-132

[21] Becker, W., & Trümper, J. 1997, A&A, 326, 682

[22] Bell, J. F., Bailes, M., Manchester, R. N., Lyne, A. G., Camilo, F., & Sandhu, J. S. 1997, MNRAS, 286, 463

[23] Berestetsky, V. B., Lifshits, E. M., & Pitaevsky, L. P. 1982, Relativistic Quantum Theory (Pergamon: Oxford)

[24] Beskin, V. S. 2009, MHD Flows in Compact Astrophysical Objects: Accretion, Winds and Jets (Heidelberg: Springer)

[25] Beskin, V. S., Gurevich, A. F., & Istomin, Ya. N. 1993, Physics of the Pulsar Magnetosphere (Cambridge: Cambridge Univ. Press)

[26] Blandford, R. D., & Scharlemann, E. T. 1976, MNRAS, 174, 59

[27] Bogovalov, S. V. 1999, A&A, 349, 1017

[28] Bogovalov, S. V., & Aharonian, F. A. 2000, MNRAS, 313, 504

[29] Cheng, K. S., Ho, C., & Ruderman, M. 1986a, ApJ, 300, 500

[30] Cheng, K. S., Ho, C., & Ruderman, M. 1986b, ApJ, 300, 522

[31] Cheng, K. S., Ruderman, M. A., & Zhang, L. 2000, ApJ, 537, 964

[32] Cheng, K. S., & Zhang, L. 1996, ApJ, 463, 271

[33] Chiu, H. Y., & Salpeter, E. E. 1964, Phys. Rev. Letters, 12, 413

[34] Chkheidze, N., Machabeli, G., & Osmanov, Z. 2011, ApJ, 730, 62

[35] Cocke, W. J., Disney, M. J., & Taylor, D. J. 1969, Nature, 221, 453

[36] Contopoulos, I., & Kalapotharakos, C. 2010, MNRAS, 404, 767

[37] Contopoulos, I., Kazanas, D., & Fendt, C. 1999, ApJ, 511, 351

[38] Daugherty, J. K., & Harding, A. K. 1994, ApJ, 429, 325

[39] Daugherty, J. K., & Harding, A. K. 1996, ApJ, 458, 278

[40] De Luca, A., Caraveo, P.A., Mereghetti, S., Negroni, M., & Bignami, G. F. 2005, ApJ, 623, 1051

[41] Dermer, C. D. 1990, ApJ, 360, 197

[42] Dermer, C. D., & Menon, G. 2009, High Energy Radiation from Black Holes (Princeton, NJ: Princeton Univ. Press)

[43] Du, Y. J., Han, J. L., Qiao, G. J., & Chou, C. K. 2011, ApJ, 731, 2

[44] Dyks, J., & Rudak, B. 2003, ApJ, 598, 1201

[45] Everett, J. E., & Weisberg, J. M. 2001, ApJ, 553, 341

[46] Fawley, W. M., Arons, J., & Scharlemann, E. T. 1977, ApJ, 217, 227

[47] Fierro, J. M., Michelson, P. F., Nolan, P. L., & Thompson, D. J. 1998, ApJ, 494, 734

[48] Ginzburg, V. L., Zheleznyakov, V. V., & Zaitsev, V. V. 1968, Nature, 220, 355

[49] Gold, T. 1968, Nature, 218, 731

[50] Goldreich, P., & Julian, W. H. 1969, ApJ, 157, 869

[51] Gonthier, P. L., Van Guilder, R., & Harding, A. K. 2004, ApJ, 604, 775

[52] Gouiffes, C. 1998, in Neutron Stars and Pulsars, ed N. Shibazaki et al. (Tokyo: Univ. Acad. Press), 363

[53] Gouiffes, C., Finley, J. P., & Ögelman, H. 1992, ApJ, 394, 581

[54] Gould, D. M., & Lyne, A. G. 1998, MNRAS, 301, 235

[55] Gould, R. J. 2006, Electromagnetic Processes (Princeton, NJ: Princeton Univ. Press)

[56] Gruzinov, A. 1999, arXiv:astro-ph/9902288

[57] Gruzinov, A. 2005, Phys. Rev. Lett. 94, 021101

[58] Halpern, J. P., et al. 2008, ApJ, 688, 33

[59] Harding, A. K., & Muslimov, A. G. 1998, ApJ, 508, 328

[60] Harding, A. K., Stern, J. V., Dyks, J., & Frackowiak, M. 2008, ApJ, 680, 1378

[61] Harding, A. K., Strickman, M. S., Gwinn, C. D. R., Moffet, D., & McCulloch, P. 2002, ApJ, 576, 376

[62] Harding, A. K., Usov, V. V., & Muslimov, A. G. 2005, ApJ, 622, 531

[63] Hessels, J. W. T., Ransom, S. M., Stairs, I. H., Freire, P. C. C., Kaspi, V. M., & Camilo, F. 2006 Science, 311, 1901

[64] Hessels, J. W. T., Roberts, M. S. E., Ransom, S. M., Kaspi, V. M., Romani, R. W., Ng, C.-Y., Freire, P. C. C., & Gaensler, B. M. 2004, ApJ, 612, 389

[65] Hewish, A., & Bell, S. J. 1968, Nature, 217, 709

[66] Hirotani, K. 2006, ApJ, 652, 1475

[67] Hirotani, K. 2008, ApJ, 688. L25

[68] Jackson, J. D. 1975, Classical Electrodynamics (2nd ed.; New York: Wiley)

[69] Jackson, M. S., Halpern, J. P., Gotthelf, E. V., & Mattox, J. R. 2002, ApJ, 578, 935

[70] Jauch, J. M., & Rohrlich, R. 1976, The Theory of Photons and Electrons (New York: Springer-Verlag)

[71] Johnston, S., Karastergiou, A., & Willett, K. 2006, MNRAS, 369, 1916

[72] Johnston, S., & Weisberg, J. M. 2006, MNRAS, 368, 1856

[73] Kaaret, P., et al. 2006, ApJ, 657, L97

[74] Kalapotharakos, C., & Contopoulos, I., 2009, A&A, 496, 495

[75] Kalapotharakos, C., Kazanas, D., Harding, A. K., & Contopoulos, I., 2011, arXiv:1108.2138

[76] Kargaltsev, O., & Pavlov, G. G. 2007, Ap&SS, 308, 287

[77] Kern, B., Martin, C., Mazin, B., & Halpern, J. P. 2003, ApJ, 597, 1049

[78] Kisaka, S., & Kojima, Y. 2011, ApJ, 739, 14

[79] Kojima, Y., & Oogi, J. 2009, MNRAS, 398, 271

[80] Komissarov, S. S. 2006, MNRAS, 367, 19

[81] Konopelko, A., et al., 2005, in Acharya, B. S., Gupta, S., Jagadeesan, P., Jain, A., Karthikeyan, S., Morris, S., & Tonwar, S. eds, Proc. 29th Inc. Cosmic Ray Conf., Vol. 4. Tata Institute of Fundamental Research, Mumbai, p. 139

[82] Kramer, M., et al. 1998, ApJ, 501, 270

[83] Krause-Polstorff, J., & Michel, F. C. 1985, MNRAS, 213, 43

[84] Kuiper, L., Hermsen, W., Urama, J. O., den Hartog, P. R., Lyne, A G., & Stappers, B. W. 2010, A&A, 515, A34

[85] Kuiper, L., et al. 2001, A&A, 378, 918

[86] Lattimer, J. M., & Prakash, M. 2001, ApJ, 550, 426

[87] Lattimer, J. M., & Prakash, M. 2007, Phys. Rep., 442, 109

[88] Lee, K. J., Du, Y. J., Wang, H. G.,, Quao, G. J., Xu, R. X., & Han, J. L. 2010, MNRAS, 405, 2103

[89] Li, J., Spitkovsky, A., & Tchekhovskoy, A. 2011, arXiv:1107.0979

[90] Livingstone, M. A., et al., 2009, ApJ, 706, 1163

[91] Longair, M. S. (ed.) 2011, High Energy Astrophysics (3rd ed., Cambridge: Cambridge Univ. Press)

[92] Lyubarski, Y. E., & Petrova, S. A. 1998, A&A, 337, 433

[93] Lyutikov, M., Otte, N., & McCann, A. 2011, arXiv:1108.3824

[94] Lyne, A. G., & Graham-Smith, F. 2006 (ed.), in Pulsar Astronomy (3rd ed., Cambridge Astrophysics Series; Cambridge: Cambridge Univ. Press)

[95] Lyne, A. G., & Manchester, R. N. 1988, MNRAS, 234, 477

[96] Maciesiak, K., & Gil, J. 2011, MNRAS, 417, 1444

[97] Manchester, R. N., Hobbs, G. B., Teoh, A., & Hobbs, M. 2005, AJ, 129, 1993

[98] Marelli, M., De Luca, A., & Caraveo, P. A. 2011, ApJ, 733, 82

[99] McKinney, J. C. 2006, MNRAS, 368, L30

[100] Mestel, L. 1973, Ap&SS, 24, 289

[101] Mestel, L. 1999, Stellar Magnetism (Oxford: Clarendon)

[102] Mestel, L., & Wang, Y.-M. 1979, MNRAS, 188, 799

[103] Michel, F. C. 1973, ApJ, 180, 207

[104] Mignani, R. P. 2011, Adv. Space Res., 47, 1281

[105] Mignani, R. P., Pavlov, G. G., & Kargaltsev, O. 2010, ApJ, 720, 1635

[106] Mignani, R. P., Zharikov, S., & Caraveo, P. A. 2007, A&A, 473, 891

[107] Mignani, R. P., Sartori, A., De Luca, A., Rudak, B., Slowikowska, A., Kanbach, G., & Caraveo, P. A. 2010, A&A, 515, 110

[108] Morini, M. 1983, MNRAS, 202, 495

[109] Muslimov, A. G., & Harding, A. K. 1997, ApJ, 485, 735

[110] Muslimov, A. G., & Harding, A. K. 2003, ApJ, 588, 430

[111] Muslimov, A. G., & Harding, A. K. 2004, ApJ, 606, 1143

[112] Ng, C.-Y., & Romani, R. 2008, ApJ, 673, 411

[113] Ogura, J., & Kojima, Y. 2003, Prog. Theor. Phys. 109, 619

[114] Okamoto, I. 1974, MNRAS, 167, 457

[115] Pacini, F. 1967, Nature, 216, 567

[116] Padmanabhan, T. 2001, Theoretical Astrophysics, Vol. 2, Stars and Stellar Systems (Cambridge: Cambridge Univ. Press),

[117] Pétri, J., Heyvaerts, J., & Bonazzola, S. 2002, A&A, 384, 414

[118] Pétri, J. 2011, MNRAS, 412, 1870

[119] Petrova, S. A. 2002, MNRAS, 336, 774

[120] Petrova, S. A. 2003, MNRAS, 340, 1229

[121] Radhakrishnan, V., & Cooke, D. J., 1969, ApL 3, 225

[122] Rees, M. L., & Gunn, J. E. 1974, MNRAS, 167, 1

[123] Pletsch, H. J., et al. 2012, ApJ, 744, 105

[124] Roberts, M. S. E., Romani, R. W., & Johnston, S. 2001, ApJ, 561, L187

[125] Romani, R. W. 1996, ApJ, 470, 469

[126] Romani, R. W., Kargaltsev, O., & Pavlov, G. G. 2005, ApJ, 627, 383

[127] Romani, R. W., & Watters, K. P. 2010, ApJ, 714, 810

[128] Romani, R. W., & Yadigaroglu, I.-A. 1995, ApJ, 438, 314

[129] Ruderman, M. A., & Sutherland, P. G. 1975, ApJ, 196, 51

[130] Rybicki, G. B., & Lightman, A. P. 1979, Radiation Processes in Astrophysics (New York: Wiley)

[131] Saz Parkinson, P. M., et al. 2010, ApJ, 725, 571

[132] Scharlemann, E. T., & Wagonar, R. V. 1973, ApJ, 182, 951

[133] Scharlemann, E. T., Fawley, W. M., & Arons, J. 1978, ApJ, 222, 297

[134] Shearer, A., et al. 1997, ApJ, 487, L181

[135] Shearer, A., et al. 1998, A&A, 335, L21

[136] Shibanov, Yu A., Koptsevich, A. B., Sollerman, J., & Lundqvist, P. 2003, A&A, 406, 645

[137] Shibanov, Yu. A., Sollerman, J., Lundqvist, P., Gull, T., & Lindler, D. 2005, A&A, 440, 693

[138] Shklovsky, I. S. 1970, ApJ, 159, L77

[139] Shukre, C. S., & Radhakrishnan, V. 1982, ApJ, 258, 121

[140] Smith, I. A., Michel, F. C., & Thacker, P. D. 2001, MNRAS, 322, 209

[141] Spitkovsky, A., & Arons, J. 2002, Adv. Space Sci. Conf. Ser., 271, 81

[142] Spitkovsky, A. 2006, ApJ, 648, L51

[143] Stecker, F. W., Hunter, S. D., & Kniffen, D. A. 2008, Astropart. Phys., 29, 25

[144] Strickman, M. S., et al. 1996, ApJ, 460, 735

[145] Sturner, S. J. 1995, ApJ, 446, 292

[146] Sturrock, P. A. 1971, ApJ, 164, 529

[147] Tademaru, E. 1973, ApJ, 183, 625

[148] Takata, J., Shibata, S., & Hirotani, K. 2004, MNRAS, 348, 241

[149] Takata, J., Shibata, S., Hirotani, K., & Chang, H.-K. 2006, MNRAS, 366, 1310

[150] Takata, J., & Chang, H.-K. 2007, ApJ, 670, 692

[151] Takata, J., & Chang, H.-K. 2009, MNRAS, 392, 400

[152] Takata, J., Chang, H.-K., & Shibata, S. 2008, MNRAS, 386, 748

[153] Takata, J., Wang, Y., & Cheng, K. S. 2011a, ApJ, 726, 44

[154] Takata, J., Wang, Y., & Cheng, K. S. 2011b, MNRAS, 414, 2173

[155] Takata, J., Wang, Y., & Cheng, K. S. 2011c, MNRAS, 415, 1827

[156] Tang, A. P. S., Takata, J., Jia, J. J., & Cheng, K. S. 2008, ApJ, 676, 562

[157] Timokhin, A. N. 2006, MNRAS, 368, 1055

[158] Thompson, D. J. 2004, in Cosmic Gamma Ray Sources, ed. K. S. Cheng & G. E. Romero (Dordrecht: Kluwer), 149

[159] Thompson, D. J., et al. 1999, ApJ, 516, 297

[160] Usov, V. V., & Melrose, D. B. 1995, Aust. J. Phys., 48, 571

[161] Van Etten, A., Romani, R. W., & Ng, C.-Y. 2008, ApJ, 680, 1417

[162] Venter, C., Harding, A. K., & Guillemot, L. 2009, ApJ, 707, 800

[163] Wada, T., & Shibata, S. 2007, MNRAS, 376, 1460

[164] Wada, T., & Shibata, S. 2011, MNRAS, 418, 612

[165] Wallace, P. T., et al. 1977, Nature, 266, 692

[166] Wang, Y., Takata, J., & Cheng, K. S. 2010, ApJ, 720, 178

[167] Wang, Y., Takata, J., & Cheng, K. S. 2011, MNRAS, 414, 2664

[168] Watters, K. P., & Romani, R. W. 2011, ApJ, 727, 123

[169] Watters, K. P., Romani, R. W., Weltevrede, P., & Johnston, S. 2009, ApJ, 695, 1289

[170] Weber, E. J., & Davis Jr., L. 1967, ApJ, 148, 217

[171] Weltevrede, P., & Johnston, S. 2008, MNRAS, 391, 1210

[172] Weltevrede, P., & Wright, G. 2009, MNRAS, 395, 2117

[173] Weltevrede, P., et al. 2010, ApJ, 708, 1426

[174] Zhang, L., & Cheng, K. S. 1997, ApJ, 487, 370

[175] Zhang, L., & Cheng, K. S. 2003, A&A, 398, 639